The Thesis Committee for Christopher William LaRoche Nelsen
Certifies that this is the approved version of the following Thesis:

Experimental Evaluation of Geocell Reinforcement Behavior using Transparent Soil Techniques

APPROVED BY
SUPERVISING COMMITTEE:

Jorge G. Zornberg, Supervisor

Amit Bhasin

Experimental Evaluation of Geocell Reinforcement Behavior using Transparent Soil Techniques

by

Christopher William LaRoche Nelsen

Thesis

Presented to the Faculty of the Graduate School of

The University of Texas at Austin

in Partial Fulfillment

of the Requirements

for the Degree of

Master of Science in Engineering

The University of Texas at Austin

August 2018

Dedication

To my family – Linda, Charles, Catherine, and Margaret. Without their support, I would not be where I am today. Thank you.

Acknowledgements

There are far too many people that deserve thanks for the support and encouragement given to me during my time at The University of Texas at Austin.

For their constant support, fantastic classroom teaching, and professional development – a huge thank you is due to the Geotechnical Engineering Faculty, especially to my advisor, Professor Jorge Zornberg. Another big thank you to Professor Amit Bhasin for his valuable review and comments on this manuscript.

For technical advice, practical experience, and endless patience – another thank you is due to my senior (and now former) graduate students, Dr. Amr Morsy and Dr. Xin Peng. In addition, thank you to all of my fellow graduate students in Geotechnical Engineering.

Thanks and recognition are also due to Federico Castro, Dr. Gregório Araújo, and Dr. Yuri Costa for their practical and technical support during research and development. In addition, the support of Phil Tomlin and Lamont Prosser with the facilities, equipment, and operations in ECJ were invaluable. A big thanks to Alejandro Marez in the Longhorn MakerStudio Wood Shop, as well.

Our research group is lucky to have the support of many undergraduate research assistants and work-study students – thank you Luis, Carlos, Sam, Henry, and Mario for your help at various stages of testing and development.

For the provision of fused quartz, a special thanks goes to Heraeus Quarzglas and the employees there. The folks at the Bosque County Recycling Center, especially Dianne Bernhardt, deserve more thanks than I can give for the hard work, endless energy, and opportunity to crush the large quantities of fused quartz in their glass pulverizer.

Another thank you is due to Joe Friedrichsen for his continued efforts to develop a streamline LabVIEW code for the improved operation of the pneumatic loading system.

Abstract

Experimental Evaluation of Geocell Reinforcement Behavior using Transparent Soil Techniques

Christopher William LaRoche Nelsen, M.S.E.

The University of Texas at Austin, 2018

Supervisor: Jorge G Zornberg

Geocells are a growing type of geosynthetic product used in many applications, including the reinforcement of unbound granular materials for the construction of flexible pavements. Although significant research has been conducted to quantify the performance of geocell-reinforced soil masses, there is no universally accepted design method for these structures. The Mechanistic-Empirical Pavement Design Guide (MEPDG) is a solid framework on which to base a geocell design method. The resilient modulus of a material is constitutive relationship between the imposed stress state and the resilient strain. It is the relevant design parameter that should be modified in the MEPDG for the design of pavement structures using geocells. However, a more robust understanding of the behavior and mechanisms that contribute to the overall performance of geocell-reinforced materials is necessary to develop theoretically-sound model. As such, the materials and equipment necessary to conduct a thorough analysis of geocells were conceived and implemented as part of this study. This equipment is based around the transparent soil concept – transparent soils are two-part media consisting of solid particles and a saturating fluid with matching refractive indices. Fused quartz and mineral oil were selected as appropriate materials to use as a granular soil surrogate. The large-scale equipment consists of a steel-framed tank with cast acrylic sides. Many lessons were learned with regard to the use of transparent soil techniques

in large-scale experiments. Preliminary results indicate the equipment is adequate to validate the results of prior geocell experiments. Additional improvements will allow for the full utilization of transparent soil capabilities and the direct observation of geocell reinforcement behavior and mechanisms in-situ.

Table of Contents

List of Tables

List of Figures

Chapter 1: Introduction

1.1: MOTIVATION

Ever since their development in the mid-1970s, geocellular confinement systems, commonly known as geocells, have been steadily growing in an already expanding geosynthetic market. According to *Markets and Markets*, the global geosynthetic market share is expected to exceed USD $15 billion by 2019, (marketsandmarkets.com 2014). Within that market, geocells accounted for USD $352 million in 2016 and are projected to reach nearly USD $590 million by 2022, (marketsandmarkets.com 2018). Much of the growth in the geocell market share is expected to be driven by extensive infrastructure construction in emerging economies throughout Asia Pacific and the Middle East, although North America and Europe are projected to see growth as well. Geocells are used in many different applications such as erosion control, channel lining, and retaining wall construction, but a large portion of the projected market growth is expected to be in the construction of low volume roads, both paved and unpaved, with a majority of that construction focused in the traditional and renewable energy production industries.

Despite the burgeoning presence of geocells in the civil engineering industry, their acceptance and further implementation by design engineers is limited by the lack of a clear design methodology. The original design methodologies were based solely on empirical design equations developed as a result of parametric studies on geocell performance. While empirical design equations are not uncommon in civil engineering practice, they have questionable validity when extrapolating beyond the range of parameters used in the experimental trials. More recently, researchers have attempted to incorporate some of the theoretical reinforcement mechanisms that actively contribute to the performance improvement due to geocells into their design equations. These methods, however, are

limited by the understanding of geocell reinforcement mechanisms, which are both complex and interdependent.

Recent advances in transparent soil technology have allowed some researchers to observe other complex soil-reinforcement interactions, especially in the context of geogrid reinforcement, (Peng and Zornberg 2016, 2017, Ezzein and Bathurst 2014, Bathurst and Ezzein 2015). Transparent soils are two-part media consisting of transparent solid particles and a saturating fluid with matching refractive indices. In principle, if the refractive indices of two adjacent materials match precisely, light will not reflect or refract at the interface between them and will therefore pass through unaffected rendering the combined medium fully transparent. Transparent soils include a number of different varieties to simulate a range of soil types and conditions. One of the more recently developed varieties is crushed fused quartz, or fused silica, used in conjunction with mineral oil to simulate granular soils such as sand and gravel commonly used as base materials in pavement construction. Utilizing transparent soil techniques will allow for the direct observation and quantification of geocell reinforcement mechanisms in-situ – a novel use of transparent soil and an internal perspective on geocell-reinforced soil behavior.

1.2: OBJECTIVES

The objectives of this research trajectory are threefold. The first objective is to observe, characterize, and quantify the separate reinforcement mechanisms that occur within geocell-reinforced soil. As previously mentioned, there have been attempts to incorporate those mechanisms into semi-empirical design methodologies, but it is difficult to quantify internal mechanisms solely from post-test forensic analyses. Transparent soil will facilitate the observation of mechanisms that may be active during different loading stages or at certain strain levels. The second objective is to provide a framework to develop

a mechanistic design methodology that accounts for the soil-reinforcement interaction mechanisms. In the context of pavement design, this mechanistic design methodology will be compatible with the Mechanistic-Empirical Pavement Design Guide, or MEPDG, the developing standard of practice for flexible and rigid pavement design. The third objective is to establish the protocols, equipment, and techniques for subsequent testing involving geocells and transparent soil.

As the first step toward achieving the objectives outlined above, the short-term objective of this two-year research project is to develop the laboratory-based experimental components of the overall research trajectory. This includes the procurement and processing of all materials (transparent soil components and various geocell test sections), the development and construction of the laboratory-scale testing equipment, and the advancement of understanding and expertise associated with the use of transparent soil techniques. An extensive literature review focused on geocells and on the use of transparent soil techniques is also crucial for the development of a robust research program that will yield novel and useful results.

1.3: Overview of Thesis

This thesis has been divided into seven chapters. The first chapter introduces the motivation for the research and its objectives. Chapter two includes a literature review of background information regarding the history, theory, and state-of-practice of geocells as well as information regarding the MEPDG and transparent soil techniques. Chapter three summarizes the materials and equipment developed during the course of this study for the purpose of conducting a comprehensive parametric evaluation of geocell-reinforced soil performance with transparent soil. Chapter four goes into detail regarding challenges encountered when scaling up transparent soil techniques from the small-scale devices used

for geogrid testing to the large-scale apparatus developed for geocell testing. Chapter five describes the typical results obtained from large-scale tests of unreinforced transparent soil masses and geocell-reinforced transparent soil masses. Chapter six provides details regarding the current capabilities of the equipment and of transparent soil for future evaluations. The potential for improving those capabilities is also explored. A parametric study that will yield novel and useful insights into the geocell reinforcement mechanisms and the parameters on which they depend is also proposed. The final chapter presents the main conclusions of this thesis and additional recommendations for future work.

Chapter 2: Background

2.1: History and Modern Usage of Geocells

2.1.1: Development and Early Applications

In the late 1970s, the U.S. Army Corps of Engineers at the Waterways Experiment Station at Vicksburg, Missouri started experimenting with alternative methods to reinforced military roads and temporary bridge approaches across soft ground. These full-scale experiments yielded the first geocell test section composed of thousands of short, mechanically-attached, corrugated pipe sections filled with sand, Figure 1. These sections were able to limit roadway deformations much more effectively than planar geotextile separators alone, (Richardson 2004).

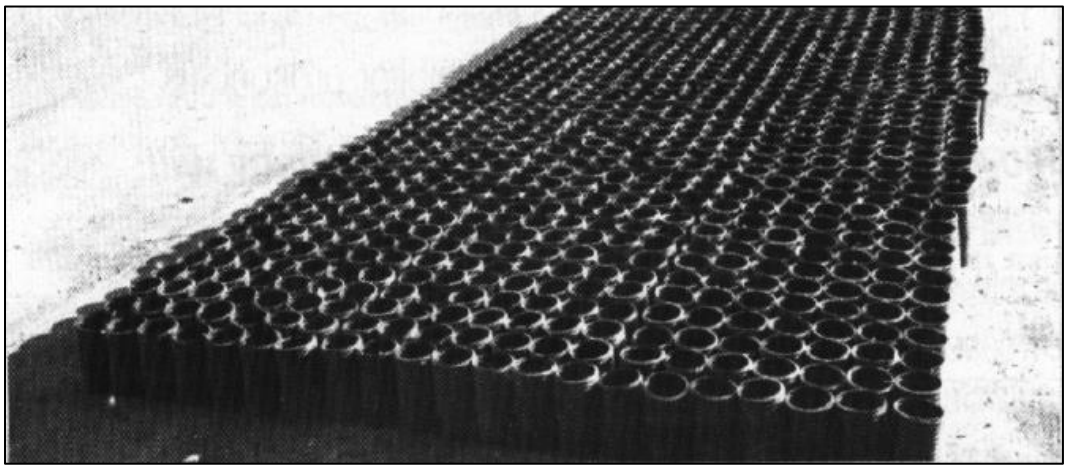

Figure 1. Corps of Engineers geocell test section, Vicksburg, 1977, (Richardson 2004)

Other candidates for geocellular confinement systems included wax-coated craft paper, hexagonal-shaped glued aluminum, low- and medium-density recycled materials, pure polyethylene, and square “egg carton” cells. In cooperation with Presto Products, Co., the USACE developed the first high-density polyethylene (HDPE) strips welded together

to form the characteristic honeycomb-like structure now common in nearly all commercial geocell products. This original product, known as "Sandgrid", was used for the rapid construction of roadways and fortified walls in Middle Eastern combat zones in the early 1990s, (Presto Geosystems 2009). Welded HDPE geocells are now commercially available worldwide and used for all of the applications outlined in the following sections. A depiction of a typical section of geocells in presented below in Figure 2.

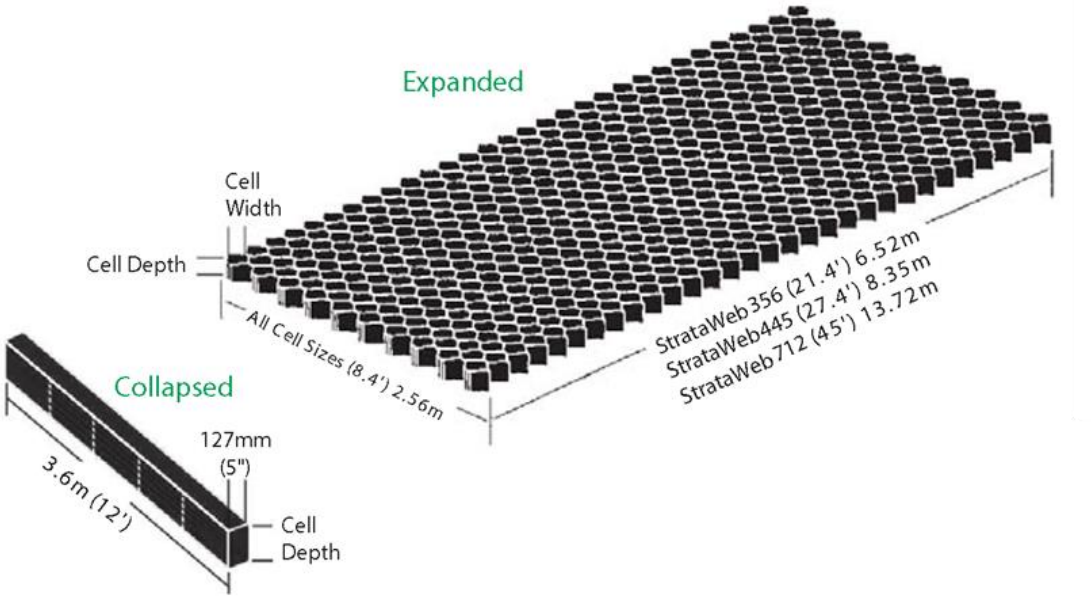

Figure 2. Typical geocell sections shown collapsed for shipping and expanded for use (Strata Systems, Inc. 2015)

Novel polymer alloys (NPA), composed of a nano-composite alloy of polyester/polyamide nano-fibers dispersed in a polyethylene matrix, have also recently been used to manufacture geocells with the same characteristic honeycomb structure. These materials have similar elastic behavior to HDPE at low temperatures, but lower thermal expansion coefficient and lower creep reduction factor as well as higher tensile

stiffness and strength than standard HDPE. These properties may contribute to the performance and design life of geocells, (Pokharel et al. 2010).

2.1.2: Modern Applications

Since the development of modern geocells, new applications have been implemented continuously. In addition to use in roadway construction, geocells are currently used for the construction of temporary and permanent retaining walls, erosion control systems, channel linings, (Richardson 2004), railroad ballast reinforcement, and embankment base reinforcement, (Bathurst and Crowe 1992). Geocellular retaining structures take on many forms including standard gravity retaining walls, geosynthetic reinforced soil walls with geocell facia, and hybrid gravity walls that use extended layers of geocells to replace planar geosynthetic reinforcement, Figure 3.

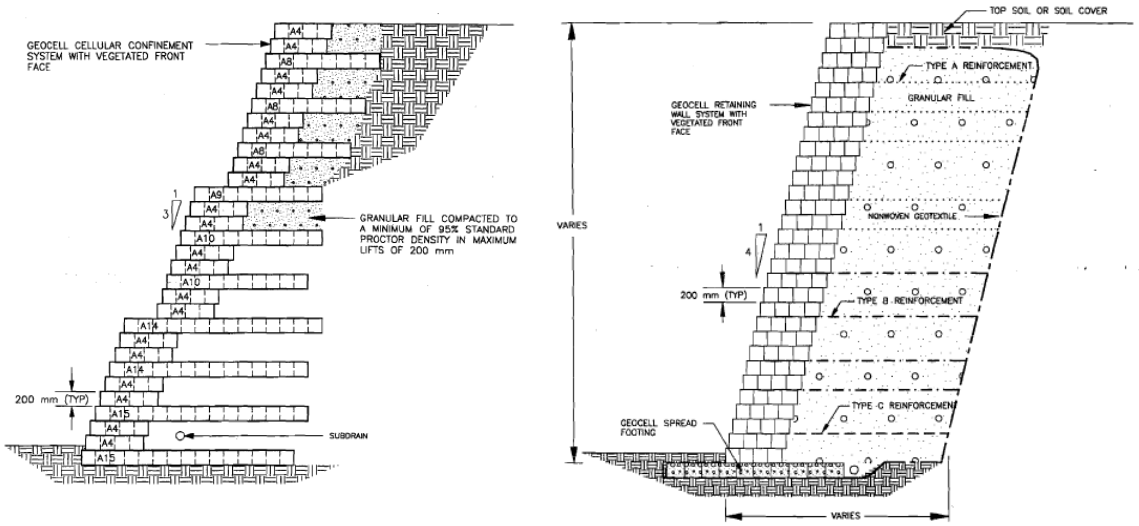

(a) (b)

Figure 3. A depiction of (a) a hybrid gravity-style retaining wall constructed using geocells and (b) a geosynthetic-reinforced soil wall with geocell facia, (Bathurst and Crowe 1992)

Geocell erosion control systems and channel linings can be filled with vegetated soil, well-graded aggregate, or concrete depending on the project requirements. These systems utilize geocells primarily for their soil retention capabilities. Railroad ballast and embankment reinforcement are examples of applications that utilize the bearing capacity improvement offered by geocells. The relevant mechanisms of geocell reinforcement depend significantly on the specific application, and as such, it is important to consider the desired application in the development of a design methodology.

2.2: Theoretical Geocell Soil Improvement Mechanisms

For the majority of early applications, the design of geocell-reinforced soil structures was based solely on empirical correlations to estimate improvement factors for bearing capacity or related geotechnical engineering parameters. As experimental laboratory and field work have continued to be performed to understand the actual mechanisms involved in the performance, the understanding of geocell behavior has improved. At this point, it is accepted that geocells derive their improved performance from three main mechanisms: 1) the confinement effect, 2) the vertical stress dispersion effect, and 3) the tensioned membrane effect. The presence of these mechanisms as well as their relative contributions to the overall performance of the reinforced system depends on many factors such as the geocell geometry, the geocell-reinforced system geometry, the loading on the system, and the native soil conditions. There may be interaction between these mechanisms such that they are not independent, but instead different aspects of a coupled behavior. Additionally, the applicability of these mechanisms is also dependent on the framework of the design methodology and the imposed limit states, which will be discussed later.

2.2.1: Confinement Effect

The confinement effect has been generally accepted to involve providing additional or apparent "pseudo"-cohesion by the geocell to an otherwise unbound granular material (UGM). As the soil within an individual cell is loaded vertically, it tends to dilate and/or move laterally. This lateral movement is restricted by the geocell, the net effect of which is thought of as an induced or apparent cohesion. It has been suggested in the literature that the confinement effect stiffens the reinforced soil zone, which can be considered as a single composite layer often referred to as a geocell mattress. It has also been noted that a geocell mattress confines the soil vertically as well as laterally due to interface shear stresses between the infill and geocell sidewalls, (Pokharel et al. 2010). The tendency to resist heaving around the loaded area may be an important mechanism in geocell-reinforced soil performance.

2.2.2: Vertical Stress Dispersion Effect

Analytical solutions for the stresses and deflections under a load of limited extent have shown that a material with a comparatively higher elastic modulus (i.e. stiffness) will distribute an applied load over a larger area than a less stiff material, (Foster and Ahlvin 1954). When subjected to a concentrated load, a geocell-reinforced soil mattress can act in this way, distributing the applied load over a wider area, thereby reducing the pressure applied to the underlying subgrade. This effect may contribute substantially to the performance of geocell-reinforced soil for applications with concentrated loads (e.g. traffic loads, shallow spread footings). However, the vertical stress dispersion effect may be negligible or nonexistent when the loaded area approaches the extent of the geocell-reinforced soil mattress as in some embankment base reinforcement applications. The

relative contribution of the different mechanisms for different applications is an area that requires further study.

2.2.3: Tensioned Membrane Effect

The tensioned membrane effect is a geosynthetic reinforcement mechanism that occurs frequently with planar reinforcement such as geogrids or geotextiles. For geocell-reinforced soil applications, the tensioned membrane effect occurs when significant vertical deformations (i.e. bending and/or rutting) occur causing the development of tensile stresses in the base of the geocell-reinforced layer. The vertical component of the tensile stresses is taken by the geocell itself thereby reducing the total amount of load transferred to the underlying subgrade, (Zhang, et al. 2010). The contribution of this effect depends on the absolute and differential magnitudes of vertical deformation. If a geocell mattress undergoes very little vertical deformation, the tensioned membrane effect will result in negligible contribution to the performance of the system. Beyond that, if excessive settlements occur uniformly over the entire system, no bending will occur and therefore no tensile stresses will develop, (Pokharel 2010). As such, the tensioned membrane effect has been excluded from some of the more recently proposed geocell design methods, (Avesani Neto et al. 2016).

2.3: Prior Experimental Investigations Into Geocell Performance

2.3.1: Triaxial Testing

Triaxial testing has been used by a number of researchers to evaluate the strength and stiffness of geocells in various configurations and with different infill materials. Bathurst and Rajagopal (1993) performed large-scale triaxial compression tests on two types of geocell-reinforced granular soils. The triaxial specimens consisted of single

cellular units with 1.15-mm thick polyethylene walls infilled with either No. 40 silica sand or 20-mm-diameter crushed limestone aggregate. The specimens had approximate dimensions of 200 mm in diameter and 200 mm in height for a height-to-diameter ratio (also known as h/d ratio or aspect ratio) of unity, typical of base reinforcement systems used in the field.

The large-scale triaxial testing yielded a number of significant results. First, geocell-reinforced specimens showed significantly greater strength than the unreinforced specimens at all levels of confining pressure as well as an increased stiffness and a strain-hardening response as illustrated by Figure 4. The reinforced specimens also showed greater axial stiffness and suppressed dilatancy indicative an active contribution from the confinement effect. In some cases, the reinforced specimens ruptured along the welded seam indicating that weld strength is important property that may limit overall performance if not properly accounted for.

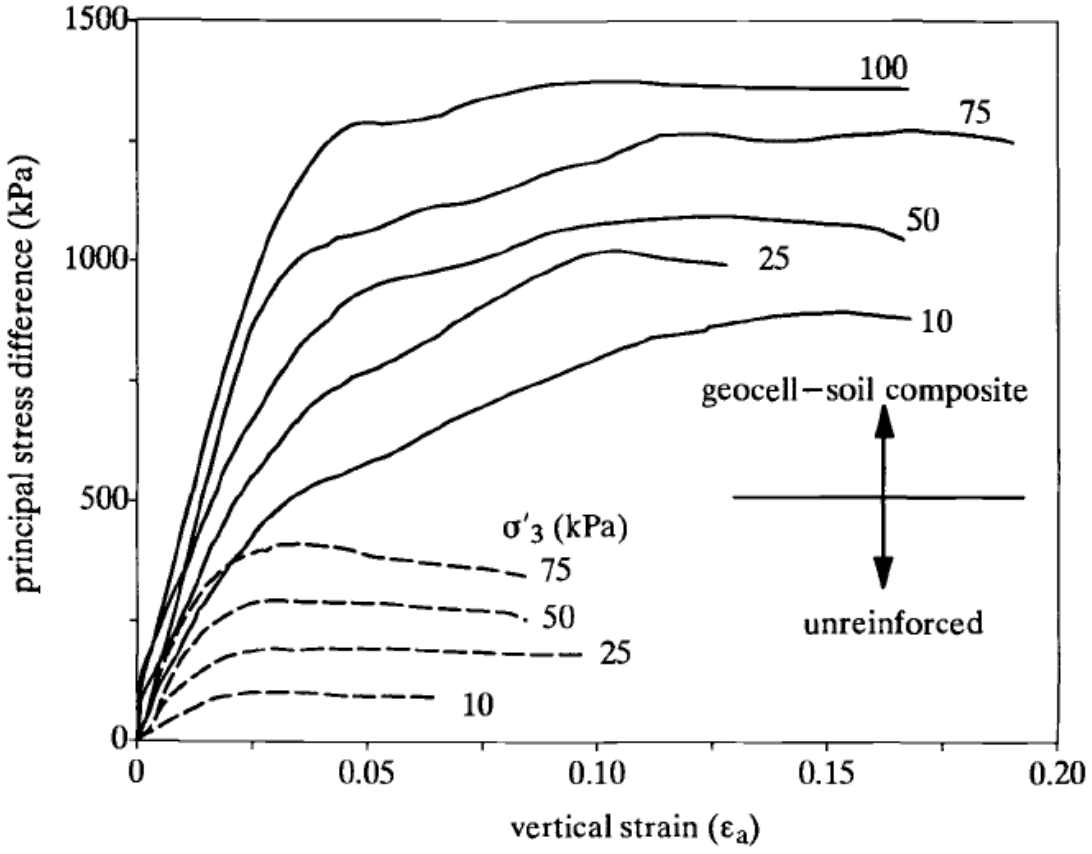

Figure 4. Principle stress difference versus axial strain from large-scale triaxial testing on geocell-reinforced granular soil, (Bathurst and Rajagopal 1993)

Triaxial compression tests have also been performed on single and multiple geocell-reinforced soil specimens, (Rajagopal et al. 1999). These specimens were constructed from different geotextiles and meshes infilled with a uniformly graded river sand (USCS classification – SP, poorly-grade sand). The various layouts used in the experimental program are illustrated in Figure 5. The results showed that, for use as geocell materials, woven geotextiles perform better than nonwoven geotextiles which are, in turn, better than soft mesh and the unreinforced granular infill. This performance can be attributed to the stiffness of each material with stiffer materials performing better than more flexible materials provided that seam rupture does not occur.

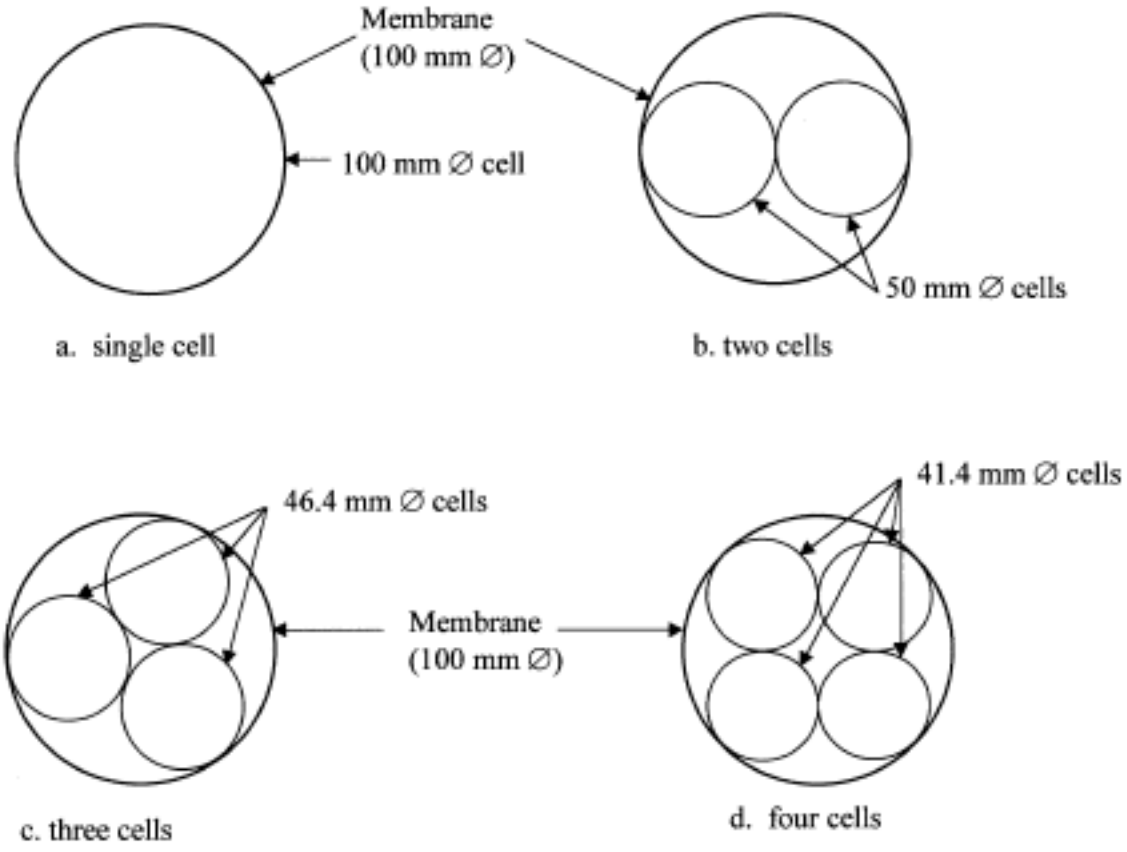

Figure 5. Different configurations of cells used in triaxial tests, (Rajagopal et al. 1999)

The provision of multiple cells was also observed by Rajagopal et al. (1999). Generally, increased strength was observed with a greater number of cells within the triaxial device. However, the added benefit of each additional cell diminished to the point at which the three- and four-cell configurations had approximately equivalent responses as illustrated by Figure 6. The authors conclude that, in this configuration, "the strength behavior of three interconnected cells may represent the mechanism of geocells having a large number of interconnected pockets," (Rajagopal et al. 1999). It should be noted that the layout of these multi-cell configurations is not representative of configurations used in commercial applications, so the applicability of these results is in question.

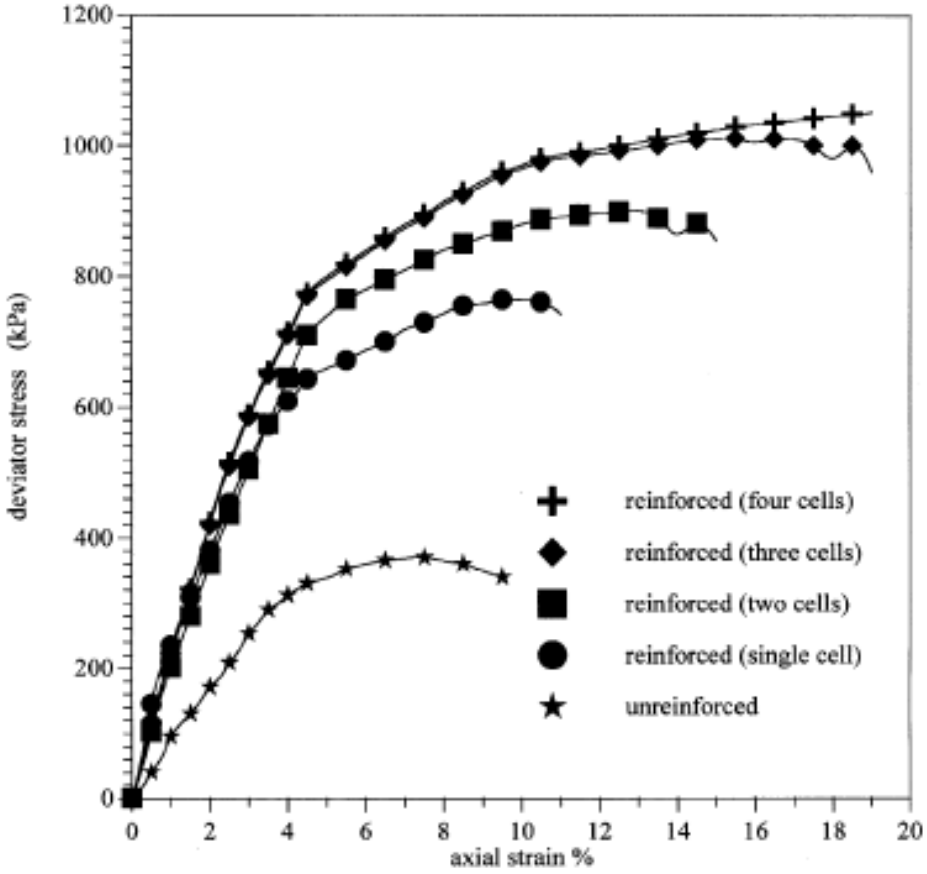

Figure 6. Effect of additional cells on the strength improvement of a granular infill, (Rajagopal et al. 1999)

A later study included the effect of cell shape in the context of triaxial testing, (Chen et al. 2013). In addition to the circular cells used by the previous authors, Chen et al (2013) used hexagonal and rectangular (block) cells as illustrated in Figure 7. While cell shape was not the most important factor in the overall strength of a particular specimen, the circular cells were shown to perform the best and the hexagonal cells performed the worst. This was attributed to the additional straining required to develop significant tensile stresses in hexagonal and block configurations using flexible cell membranes. It should be noted that commercially-available geocells have a unique shape and configuration that is

not represented by any of the cell shapes used in this experiment. However, the authors do note that "constraint by adjacent cells prevents the cells from expanding laterally, and consequently the mobilization of the tensile strength of geocells is restrained in multi-cell configurations," (Chen et al. 2013). This condition is applicable to commercial geocell products, and its effect should be accounted for in design.

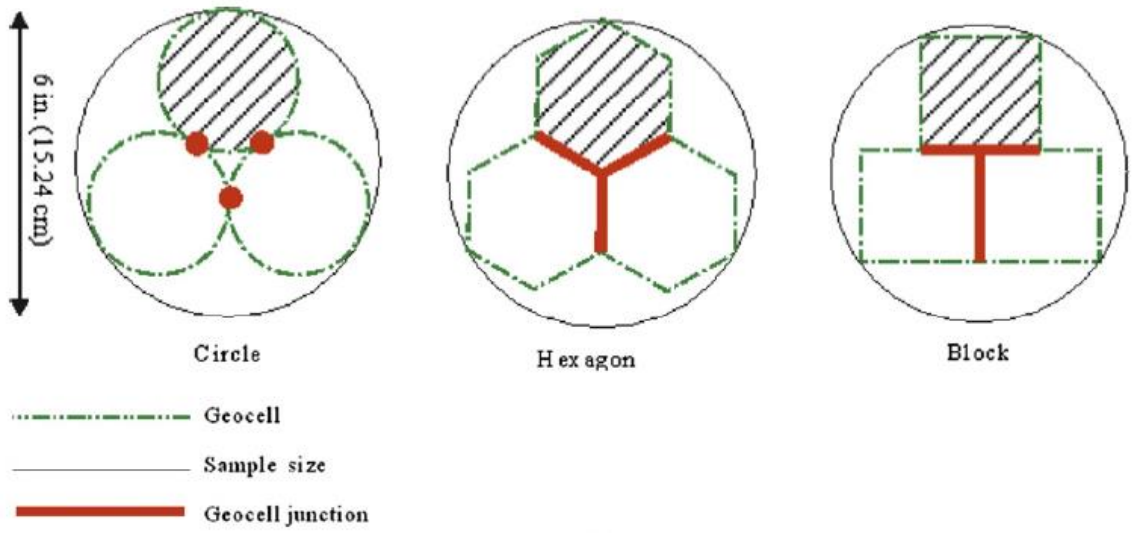

Figure 7. Various geocell shapes used in triaxial compression tests, (Chen et al. 2013)

All three of the studies summarized in this section focus on the confinement effect as it relates to the performance of geocell-reinforced soils. Parameters under observation include the geocell material properties (tensile strength, tensile stiffness, and seam strength), infill material properties (friction angle), and geocell geometry (aspect ratio, cell size, cell shape, number of cells). One of the major takeaways is that the provision of geocell reinforcement does not significantly affect the friction angle of the infill material as illustrated by the p-q failure envelopes from Bathurst and Rajagopal (1993) and Rajagopal et al. (1999), Figure 8. As such, the confinement effect can be quantified as an

additional cohesive strength. This additional cohesive component is the basis of the Apparent Cohesion Method; more details can be found in Section 2.4.2: Apparent Cohesion. However, this method may have a significant limitation in that it does not account for the other two potential global mechanisms, the vertical stress dispersion effect and the tensioned membrane effect, present in full-scale geocell sections.

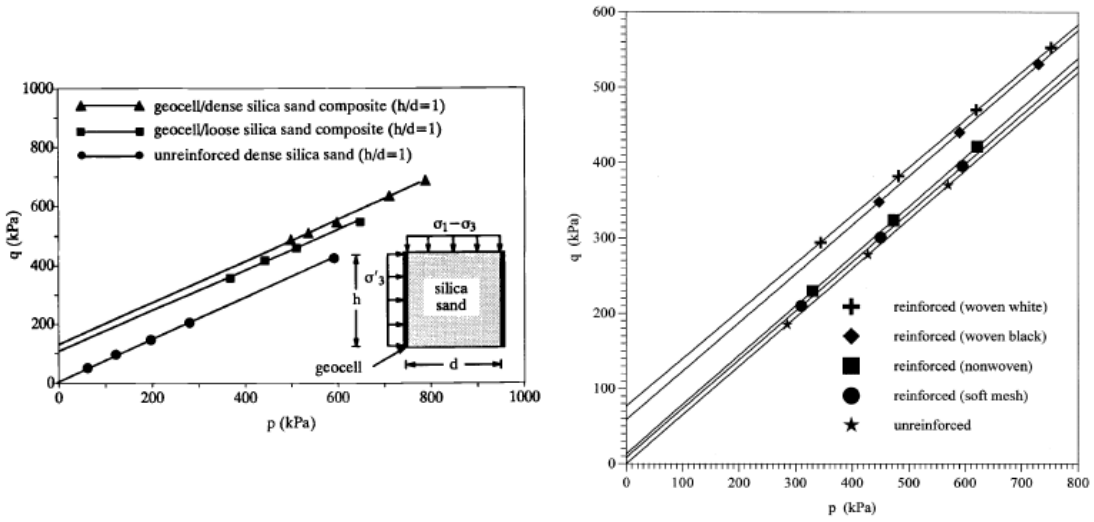

(a) (b)

Figure 8. p-q failure envelopes from (a) Bathurst and Rajagopal (1993) and (b) Rajagopal et al. (1999)

2.3.2: Medium-Scale Experiments

Due to the significant effect of geocell mattress geometry on intercellular interaction, a significant amount of effort has been put into the evaluation of geocell-reinforced soil on a medium scale. These experiments typically consist of geocell mattress sections of limited extent with pocket shapes and dimensions comparable to commercial products. The sections have often been constructed in tanks or other containment devices with rigid walls and bases. As such, the effects of boundary conditions have been of

primary concern. Besides the increased scale, one added benefit of the medium-scale tests over the triaxial tests is the ability to use specific subgrades that represent the soft subgrades often encountered in the field. In addition, different loading conditions can be imposed in the medium-scale setups such as circular or rectangular plate loading, strip loading, and simulated traffic loading.

S. K. Dash from the Indian Institute of Technology, Kharagpur published extensively on medium-scale experiments on geocell-reinforced soil from 2001 to 2013. The same medium-scale setup was used for most experiments with some modifications in later studies. It included a test tank with inside dimensions of 900 mm in length, 900 mm in width, and 600 mm in height. A load frame was used to provide a reaction force for the rigid steel plates of varying dimensions used as footings. The force was applied by a manually-operated hydraulic jack. The interface between the load plate and the soil was roughened by applying sand with epoxy. In general, test sections had dimensions nearly the full length and width of the test tank, but earth pressure cells were used to verify there was little to no interaction with the rigid tank boundaries, (Dash et al. 2003). Dash et al. (2003) studied, among many other things, the behavior of geocell-reinforced sand beds under circular footings, their behavior under strip loading, the effect of subgrade modulus, the effect of infill material, and the effect of geocell type.

It should be noted that the majority of the geocells tested by Dash were manually constructed from geogrid sections attached with bodkin joints, Figure 9. This allowed for the creation of custom geocells with unique shapes and sizes such as diamond and chevron patterns, Figure 10, but these may not be representative of the commercially-available geocell sections with the characteristic honeycomb shape.

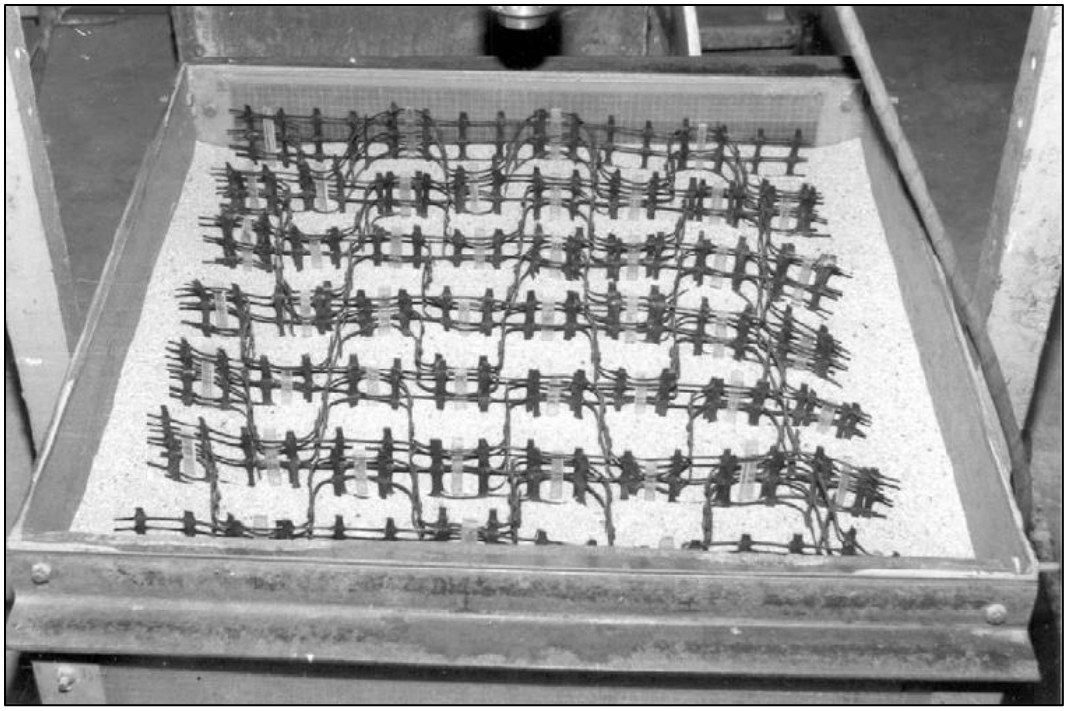

Figure 9. Custom geocell test section constructed from geogrid sections with bodkin joints, (Dash et al. 2003)

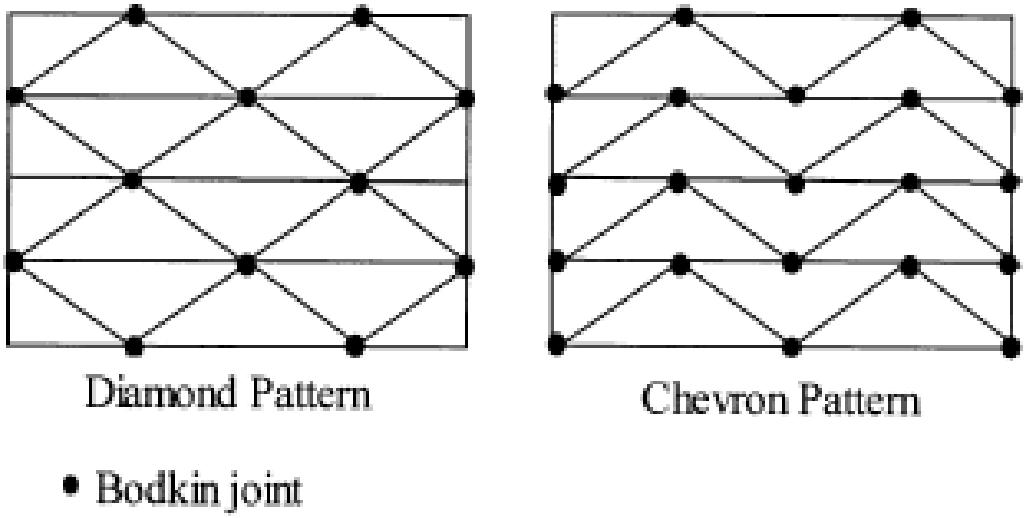

Figure 10. Depictions of different patterns used to create custom geocell test sections, (Dash et al. 2001)

As mentioned previously, much of the experimental work on geocell-reinforced soil only quantified the improvement due to the reinforcement for different conditions and did not attempt to attribute the improvement to different factors. Dash et al. (2001) conformed to this approach by quantifying the performance of the geocell-reinforced test sections to an unreinforced baseline case with a bearing capacity improvement factor, I_f. This improvement factor is often presented at different levels of settlement ratios (settlement divided by the section width, s/B [%]). This is a useful framework to quickly evaluate many different conditions in a parametric study, but it does not give insight into the contribution of different mechanisms that are fundamental to the overall performance.

Even with the limitations in the analytical framework, the studies by Dash et al. (2001, 2003, 2007, 2008, 2012, 2013) provide significant insight into parameters that affect the overall performance of geocell-reinforced soil. Dash et al. (2001) presented a number of conclusions for geocell-reinforced sand beds under strip loading:

1. The pressure-settlement behavior is approximately linear up to s/B ≈ 50% and a load up to 8 times the ultimate capacity of the unreinforced case.
2. A geocell mattress with dimensions approximately equal to the footing still shows improvement by acting as a deeply-imbedded footing.
3. Surface heave can be reduced or eliminated with a geocell mattress wide enough to restrict the formation of failure planes within the foundation soil.
4. The chevron pattern is more beneficial than the diamond pattern (although this conclusion may not have bearing in discussions on commercial products for reasons noted above).
5. Improvement due to the geocell mattress is significant up to a geocell height equal to twice the width of the footing after which there is negligible improvement.

6. The optimum width of the geocell mattress is 4 times the footing width; at this width the mattress intercepts all potential failure planes within the foundation soil.
7. The optimum depth below the surface for the geocell mattress is 10% of the footing width from the bottom of the footing.
8. The density of the infill soil is an important parameter; a dense soil configuration induces dilation and lateral expansion of the infill soil, which transfers load from the soil to the geocell.

Dash et al. (2003) presented similar conclusions for geocell-reinforced sand beds subjected to load from a circular footing. In that case, selected conclusions were as follows:

1. The performance increases with the width of the geocell mattress up to 5 times that of the footing, beyond which improvement is negligible.
2. Improvement due to the geocell mattress is significant up to a geocell height equal to twice the width of the footing after which there is negligible improvement.
3. An additional layer of planar geogrid significantly improves the performance of the geocell mattress in terms of load-carrying capacity and stiffness. (The provision of basal geogrid has become a common practice in the application of geocells for load-carrying applications.)

Dash et al. (2007) made an important advancement to the test tank by providing a transparent side wall made from acrylic through which the deformation patterns and failure planes could be observed. It should be noted that this transparent side was used in conjunction with a strip load oriented perpendicularly to the side wall causing a plane-strain condition. Using this new test tank, the authors were able to directly observe failure planes within the foundation soil delineated by discontinuities in alternating white and

colored sand layers. Using these observations, the authors were able to quantify load dispersion angles, Figure 11, a significant insight into the vertical stress dispersion effect.

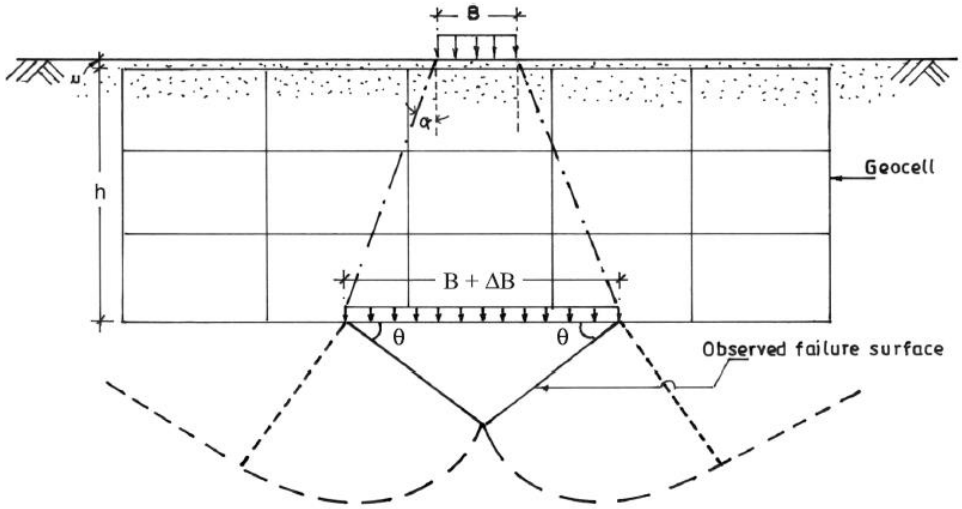

Figure 11. A depiction of observed failure surfaces and approximated load dispersion, (Dash et al. 2007)

Figure 12. Post-test deformation pattern of subgrade soil underlying a geocell mattress, (Dash 2012)

Equation (1) was used to compute the approximate dispersion angle:

$$tan\,\alpha = \frac{\Delta B}{2(h+u)} \qquad (1)$$

where:

α = the load dispersion angle

ΔB = the observed increase in loaded area at the base of the geocell mattress

h = the height of the geocell mattress

u = the depth of the geocell layer below the surface

In general, the load dispersion angle has been reported to increase as the size of the geocell pocket opening decreases, (Dash 2012). This is explained by the increasing flexibility of the geocell mattress with increasing pocket size; greater flexibility allows the load to be transferred to the soil locally around the footing. α also increases with an increase in height of the geocell mattress until h/B = 1.2 beyond which the trend reverses. Other trends of the load dispersion angle with respect to factors such as width of the geocell mattress and depth below the surface were also found. In this study, typical dispersion angles ranged from ~18° to ~34° with extremes at ~4° and ~53°, (Dash et al. 2007).

Dash et al. (2008) continued experimental work with geocells by evaluating the subgrade modulus, a concept introduced for the stress analysis of railroad ballast and conventionally defined as the secant modulus on a load-displacement curve at a point corresponding to a particular settlement. The authors also developed a regression model to estimate the subgrade modulus of geocell-reinforced beds as a function of various geometric ratios of the geocell mattress including: s/B, d/B, h/B, b/B, and u/B,

where:

s = the settlement of the footing at failure

d	=	the pocket size of an individual cell
h	=	the height of the geocell layer
b	=	the width of an individual cell
u	=	the depth of placement of the geocell layer
B	=	width of the footing

While the value of this empirical equation is noted, its efficacy is limited to a narrow range of conditions, most notably the custom geocells constructed from geogrid in a chevron pattern and singular infill and foundation soils used. In addition, all of the tests run by Dash et al. (2008) consisted of slow, monotonic loading patterns. Those loading conditions may be applicable for embankment stabilization or the reinforcement of shallow foundations, but traffic loading patterns are best approximated by cyclic, or at least repeated, loading conditions.

In an effort to better understand the behavior of geocell-reinforced soil under traffic-like loading conditions (i.e. low amplitude, repetitive loading), researchers have conducted large-scale experimental evaluations of geocell-reinforced bases under repeated loading, (Pokharel et al. 2017). The equipment used in this particular experiment consisted of an 800-mm square box with a 120-mm depth. The geocell-reinforced soil was loaded via a pneumatic actuator. For a given load cycle, the maximum load (either 345 kPa or 552 kPa) was applied in 15 s, maintained for 20 s, released over a 15 s period, and the nominal seating load was then maintained for 20 s before the next cycle. Single and multiple geocell configurations were tested with three different infill materials: 1) a poorly-graded sand (SP), 2) a well-graded aggregate (GW-GC), and 3) a quarry waste material (SP-SC).

The results of the study were used to draw a number of conclusions including:

1. Geocell-reinforced soils had higher initial moduli than unreinforced soils with improvement factors ranging from 1.26 to 2.04 for the different soil types.
2. Geocell reinforcement reduced the amount of permanent deformation accumulated over the full loading sequence. Multiple geocells reduced the permanent deformation to a greater degree than single-geocell configurations.
3. The traffic benefit ratio (TBR), defined as the "the ratio of the number of cycles necessary to reach a given rut depth (i.e., the permanent deformation) for a geocell-reinforced test section to that for an unreinforced section at the same rut depth with the same section thickness and base and subgrade properties," (Pokharel et al. 2017), was 8 for single-geocell configurations and 12 for multiple-geocell configurations.
4. Geocell reinforcement allowed the quarry waste and well-graded aggregate to have a higher percentage of elastic deformation reaching 90% after the initial 10 cycles, typically.

2.3.3: Full-Scale and Field Experiments

Full-scale and field experiments have also been conducted in an effort to demonstrate that the geocell-reinforcement behaviors and mechanisms observed in laboratory settings also applied in field settings. An experimental application in Delaware County, Pennsylvania showed significant improvement after a pavement section was rebuilt using geocell reinforcement over a very soft subgrade (CBR 1.5% – 6.5%), (Al-Qadi and Hughes 2000). The rebuilt pavement structure showed a twofold increase in resilient modulus as determined by Falling Weight Deflectometer (FWD) analyses. In

addition, the road section showed no signs of distress three years post-construction; the previous pavement section failed due to excessive rutting after only 7 days. However, the geocell reinforcement was used in conjunction with basal geogrid and geotextile reinforcements, so the contribution of the geocell reinforcement to the improved performance was not possible to determine. The authors suggest that the additional confinement provided by the geocell and the separation provided by the planar reinforcements were both influential in the successful application.

A similar experiment was conducted in India with the addition of in-situ earth pressure monitors to measure the vertical stress in the base material underlying the geocell reinforcement, (Kief and Rajagopal 2008). The reinforced section showed a 50% reduction in vertical stress compared to an unreinforced test section. In addition, finite element analyses were used to back-calculate the stiffness of the geocell-reinforced layer of the test section. The analyses indicated that the stiffness of the reinforced material was improved by a factor of 5. The reinforcement increased the bearing capacity of the low-strength subgrade by approximately 2.5 times. The authors also noted the auxiliary benefits of using geocells for pavement reinforcement over soft subgrades, including a reduction in excavation, haul and infill. The reduction in construction cost and operation cost allows for a shift from road maintenance and rehabilitation to new construction, an important benefit in growing economies such as India.

In addition to field tests, some researchers have also performed full-scale Accelerated Pavement Testing (APT) on geocell-reinforced test sections, (Yang et al. 2012). This particular APT involved using a single-axle, dual-wheel load applicator with a 552 kPa (80 psi) tire pressure that applied a repeated 80-kN (18 kip) load with moving wheels to accurately simulate traffic loading in a controlled environment. These tests, in particular, were conducted on unpaved road sections with NPA geocells to demonstrate the

improvement of sand bases in terms of overall stability and permanent deformations. The testing showed that a 15-cm geocell reinforcement layer enabled the sand base to withstand 5000 loading cycles; the unreinforced base could not withstand a single load application without excessive rutting. Testing with 10-cm geocell-reinforced layer resulted in "considerable rutting" due to cell bursting and seam failure. The authors indicated that the seam rupture failure mode could be avoided with a thicker geocell reinforcement layer or a higher seam weld strength. Strain gauge measurements indicated that cells within the wheel path experienced tensile stresses, while the cells outside of the wheel path experienced compressive stresses. These stresses are indicative of the tendency for soil particles to move laterally from underneath the wheel path.

2.4: CURRENT DESIGN METHODS

In addition to the numerous experimental studies that have been performed involving geocell reinforcement, a number of design methodologies have been proposed for various applications of geocell reinforcement. The methods outlined in the following section are focused on the bearing capacity improvement capabilities of geocell reinforcement. Geocell behavior and the corresponding theoretical mechanisms are incorporated in these methods by varying degrees. However, none of the methods fully combine all three mechanisms into a single coherent framework.

2.4.1: Koerner's Method

In his book, *Designing with Geosynthetics*, Koerner introduced a simplified method to predict the performance of geocell-reinforced soil based on Terzaghi's bearing capacity formulas developed in 1943, (Koerner 2005). These formulae were developed to prevent catastrophic bearing capacity failures; this is called a *strength requirement*, which is a

limiting or ultimate state (Coduto et al. 2011). Terzaghi's original formulae were developed for the plain-strain condition due to continuous strip footings, but subsequent refinements included shape factors to account for discrete, three-dimensional shallow foundations. Figure 13 is a depiction of the idealized unreinforced and reinforced bearing capacity failure surfaces with and without a geocell mattress.

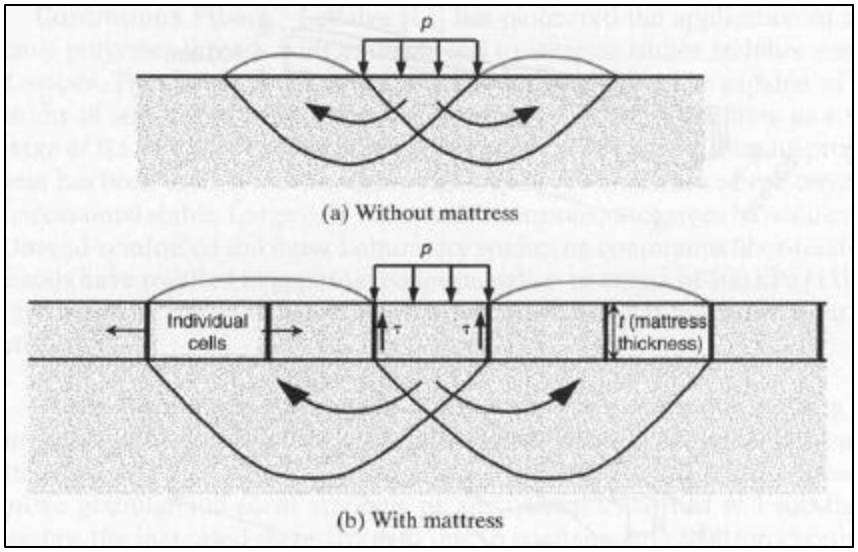

Figure 13. Theoretical bearing capacity failure mechanisms of sand without and with a geocell confinement system, (Koerner 2005)

Koerner (2005) based his method on Terzaghi's modified bearing capacity equation, below:

$$p_u = cN_c\zeta_c + qN_q\zeta_q + 0.5\gamma BN_\gamma\zeta_\gamma \qquad (2)$$

where:

p_u = maximum unreinforced bearing capacity stress (≈ tire inflation pressure of vehicles driving on the system);

c = cohesion (equal to zero when considering granular soil such as sand);

q = surcharge load (= $\gamma_q D_q$), in which

γ_q = unit weight of soil within geocell, and

D_q = depth of geocell;

B = width of applied pressure;

γ = unit weight of soil in failure zone;

N_c, N_q, N_γ = bearing capacity factors, which are all functions of internal friction angle of the soil, ϕ;

ζ_c, ζ_q, ζ_γ = shape factors used to account for differences from the plane strain assumption of the original theory.

In Koerner's method, the contribution of the geocell reinforcement is accounted for based on the interface shear resistance, τ, between the infill soil and the walls of individual cells within the mattress, see Figure 13b. This interface shear strength is calculated as:

$$\tau = \sigma_h \tan \delta \qquad (3)$$

where:

τ = interface shear strength between geocell and soil contained within it;

σ_h = average horizontal force within the geocell ($\approx p \cdot K_a$);

p = applied vertical pressure;

K_a = coefficient of active earth pressure (= $\tan^2(45 - \phi/2)$ from Rankine theory);

δ = angle of shearing resistance between soil and cell wall material ($\approx$ 10º to 30º between sand and smooth or textured geomembranes; $\approx$ 20º to 30º between sand and geotextiles).

According to Koerner, the reinforced bearing capacity, p_r, could be approximated simply as the unreinforced bearing capacity plus two times the interface shear strength, assuming a two-dimensional geometry:

$$p_r = p_u + 2\tau \quad (4)$$

Thus, Koerner's full design equation for the bearing capacity of geocell-reinforced soil is as follows:

$$p_r = cN_c\zeta_c + qN_q\zeta_q + 0.5\gamma BN_\gamma\zeta_\gamma + 2p\,K_a \tan\delta \quad (5)$$

2.4.2: Apparent Cohesion

The apparent cohesion methodology is based on the concept that additional confining pressure is generated by membrane stresses, as presented by Henkel and Gilbert (1952) in the context of triaxial compression tests. Henkel and Gilbert related the additional confining pressure applied to a triaxial specimen to the circumferential strain at failure and the modulus of the membrane, as follows:

$$\Delta\sigma_3 = \frac{2M\varepsilon_c}{D} \cdot \frac{1}{(1 - \varepsilon_a)} = \frac{2M}{D_0} \cdot \left[\frac{1 - \sqrt{1 - \varepsilon_a}}{1 - \varepsilon_a}\right] \quad (6)$$

where:

ε_c	=	circumferential strain at failure;
ε_a	=	axial strain at failure;
D_0	=	initial diameter of the sample;
D	=	diameter of the sample at an axial strain of ε_a
M	=	modulus of the membrane.

Under the assumption that an individual geocell acts in a similar manner to a rubber triaxial membrane, the apparent cohesion due to the geocell layer can be approximated as a function of the additional confinement and the Rankine passive earth pressure. The apparent cohesion can be added to the natural cohesion of the infill soil, if applicable, to determine the cohesive strength of the geocell layer, (Rajagopal et al. 1999).

$$c_r = \frac{\Delta\sigma_3}{2} \cdot \sqrt{K_p} \qquad (7)$$

where:

c_r = apparent cohesion induced due to geocell confinement;

K_p = coefficient of passive earth pressure (= $\tan^2(45 + \phi/2)$ from Rankine theory).

It is assumed that the geocells do not affect the internal friction angle of the soil; the additional confinement and corresponding apparent cohesion are the only effects, which can be visualized using Mohr's circles, as in Figure 14 from (Rajagopal et al. 1999).

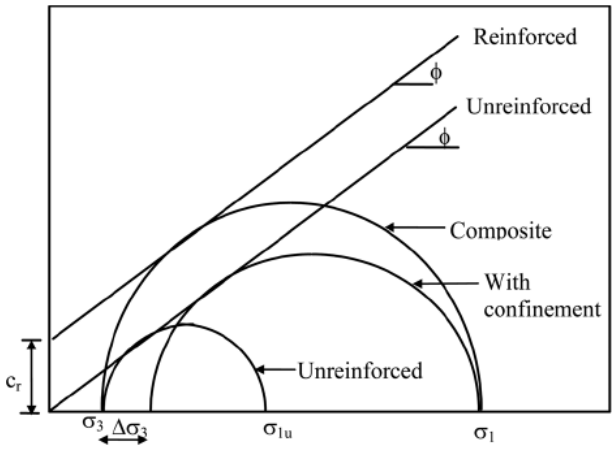

Figure 14. Mohr's circles depicting the unreinforced and reinforced failure envelopes due to geocell reinforcement, (Rajagopal et al. 1999).

It has been noted that the increase in confining pressure due to the geocell reinforcement will also induce an increase in the stiffness of the confined soil, (Rajagopal et al. 2001), which can be accounted for using the hyperbolic model as described by Duncan and Chang (1970), below:

$$E_t = \left[1 - \frac{R_f(1-\sin\varphi)(\sigma_1-\sigma_3)}{2c\cos\varphi+2\sigma_3\sin\varphi}\right]^2 \cdot K_r \cdot P_a \cdot \left(\frac{\sigma_3}{P_a}\right)^n \qquad (8)$$

where:

E_t = elastic modulus of the geocell-reinforced soil

R_f = failure ratio (typically in the range of 0.6 to 0.95)

K_r = modulus number of the reinforced soil (= $K_u + \lambda \cdot 50 \cdot M^{0.16}$)

K_u = modulus number of the unreinforced soil

λ = interaction parameter between geocell pockets dependent on the number of cells (= 4 in triaxial tests with 3 and 4 geocells)

P_a = atmospheric pressure

n = exponential parameter (empirically, ~ 0.70)

In the apparent cohesion method, the geocell-reinforced soil layer is modelled as a single, composite layer with reinforced strength and stiffness parameters. This framework has been used in numerical studies conducted to model the performance of geocell-reinforced soils. It is contrasted in Section 2.4.5 with other numerical studies that model the geocell and infill material as separate components with their own strength and stiffness parameters.

It should be noted that the Apparent Cohesion method was developed for the design of geocell-reinforced embankments. Accordingly, the stresses and strains involved with these types of structures may be significantly different than those at work in typical pavement structures. Therefore, these models may not be applicable for the small-strain, repetitive loading conditions that build up cumulative damage such as traffic loading systems; see Section 2.5 for more details.

2.4.3: Presto's Method

Presto Geosystems, Inc. proposed their own design equation for geocell-reinforced soil for unpaved roads over soft soils using a bearing capacity framework, (Presto Geosystems 2008). Presto's method is based on empirical data and Boussinesq's elasticity theory. The proposed equation is as follows:

$$p_r = 2\frac{h}{d}K_a\sigma_{vm}\,tan\,\delta + c_u N_c \qquad (9)$$

where:

p_r = reinforced bearing capacity

h/d = geocell aspect ratio

K_a = active earth pressure coefficient

σ_{vm} = average vertical stress (calculated at the top and bottom of the geocell mattress using Boussinesq's elasticity theory)

δ = interface shear angle between the cell wall and the filling soil (~ 0.7ϕ suggested)

c_u = subgrade shear strength

N_c = bearing capacity coefficient based on traffic from the US Forestry Service guidelines; 2.8 for high traffic and 3.3 for low traffic)

2.4.4: Other Analytical Methods

Many other researchers have proposed methods to calculate the bearing capacity of geocell-reinforced soil. One such proposed methodology presented by Avesani Neto et al. (2013) incorporates the theoretical geocell improvement mechanisms described in Section 2.2. Specifically, Avesani Neto argues that for most applications with small subgrade displacements and low geosynthetic stiffness the tensioned membrane effect can be considered negligible, so only the confinement effect and vertical stress dispersion effect are incorporated into the final method. Avesani Neto's method, like Koerner's method, is based on Terzaghi's bearing capacity equation with an additional improvement factor provided by the geocell reinforcement.

For the computation of the confinement effect improvement, Avesani Neto used the at-rest lateral earth pressure coefficient instead of the active lateral earth pressure to determine the shear stress between the cell wall and the infill soil. This shear stress is used to define a unitary pocket shear force by multiplying by the total area of the cell walls with respect to the three-dimensional geometry. The confinement effect improvement is quantified as the sum of the unitary pocket shear forces under the loaded area, numerically the unitary pocket shear force multiplied by the number of cells under the loaded area, in this case four:

$$\Delta F_\tau = 4\frac{h}{d}K_0 pBL\ tan\ \delta \qquad (10)$$

The improvement from the vertical stress dispersion effect is due to the distribution of applied load over a larger area, which results in a reduced stress applied to the soft subgrade. Avesani Neto limits the distance of load redistribution to one pocket diameter, d, from the loaded area justified by the wall rigidity and material discontinuity at cell walls which bar any additional spreading. Thus, the stress acting on the subgrade, p*, can be defined by the following equation:

$$p^* = \left(p - 4\frac{h}{d}K_0 p \tan\delta\right) \cdot \frac{BL}{(B+2d)(L+2d)} = \left(p - 4\frac{h}{d}K_0 p \tan\delta\right) \cdot e \qquad (11)$$

Overall, the reinforced bearing capacity can be expressed as the unreinforced bearing capacity plus the difference between the applied load and the stress that acts on the subgrade or in its full form:

$$p_r = p_u + (p - p^*) = p_u + 4\frac{h}{d}K_0 p \tan\delta + (1 - e)p \qquad (12)$$

2.4.4.1: Comparison of Analytical Methods

In a later study, Avesani Neto et al. (2016) compared his proposed analytical bearing capacity method to other methods including Koerner, Presto, and the Apparent Cohesion Method. This comparison was performed using data from eight different experimental studies on geocell-reinforced soil from 1994 to 2009. The comparison was grouped into two sections, one for sandy subgrades and one for clayey subgrades, in order to illustrate different analytical limitations. Figure 15 and Figure 16 illustrate the results of the comparison on sandy subgrades and clayey subgrades, respectively.

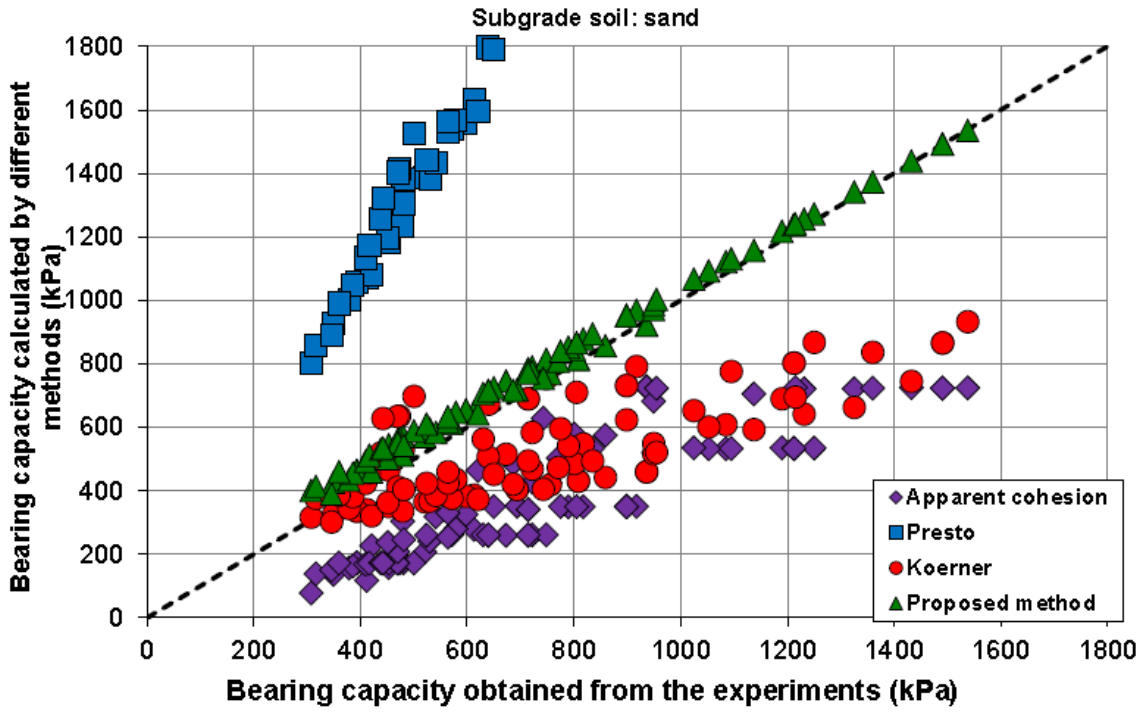

Figure 15. Comparison of various bearing capacity equations for geocell-reinforced soil over sandy subgrades

For experiments of geocell-reinforced soil over sandy subgrades, Presto was found to significantly overestimate the reinforced bearing capacity, Apparent Cohesion significantly underestimates the reinforced bearing capacity, and Koerner generally underestimates the experimental results.

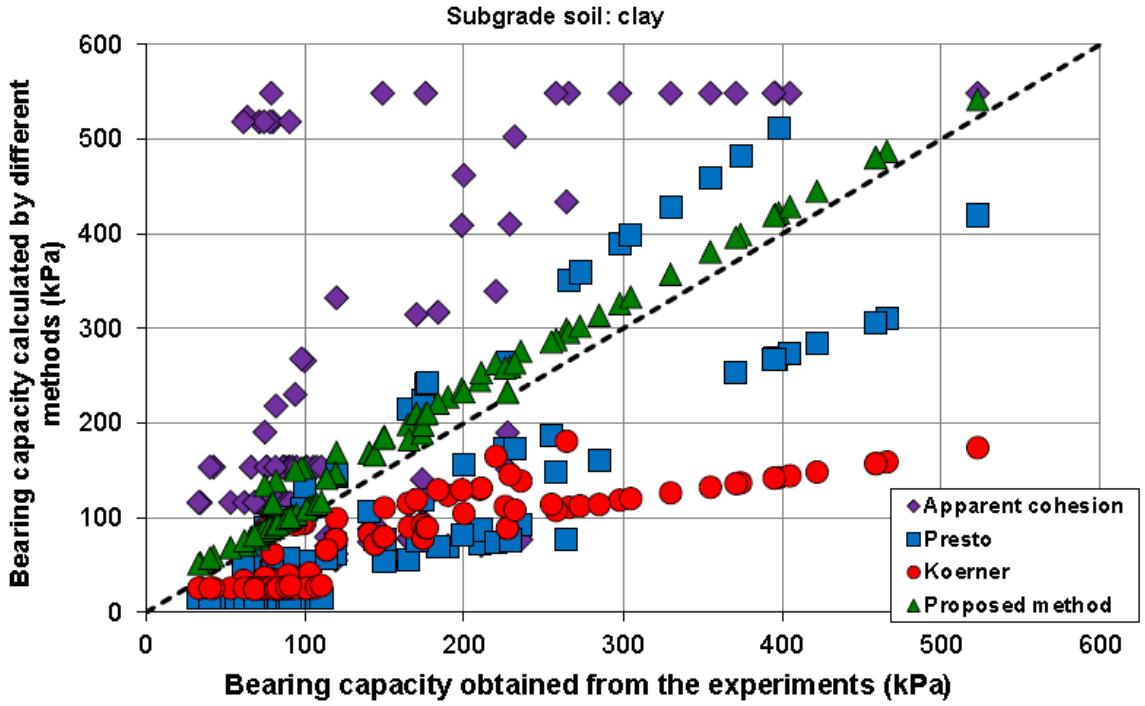

Figure 16. Comparison of various bearing capacity equations for geocell-reinforced soil over clayey subgrades

For experiments of geocell-reinforced soil over clayey subgrades, Presto overestimates and underestimates the reinforced bearing capacity, Apparent Cohesion significantly overestimates the reinforced bearing capacity, and Koerner generally underestimates the experimental results.

2.4.5: Numerical Methods

While numerical methods were not a focus of this study, it is important to note that two major frameworks exist for the analysis of the geocell-reinforced systems in finite element analyses. First, using a method such as the Apparent Cohesion Method, the geocell mattress can be modelled as a single composite layer with strength and stiffness properties representative of the reinforced section. A good reference for this category of numerical

method is Latha (2011). The benefit of this simplified numerical model is ease-of-use and the development of strength parameters based on the Apparent Cohesion Method.

The second category of numerical models involved the creation of individual geocell elements to capture the soil-reinforcement interaction mechanisms and overall geocell mattress behaviors. This type of numerical model is much more complex than a single composite layer and requires the development of model parameters for the infill soil, the geocell material, and interaction parameters. References for this category of numerical model include Leshchinsky and Ling (2013), Hedge and Sitharam (2015), and Avesani Neto et al. (2015).

2.5: MECHANISTIC-EMPIRICAL FRAMEWORK

Although most of the work in geocell design methodologies has been focused in the context of ultimate bearing capacity, the projected use of geocells for paved and unpaved roads necessitates a different framework for the development of an applicable design methodology. The Mechanistic-Empirical Pavement Design Guide, the most recent and advanced framework for the design and analysis of both flexible and rigid pavements, is a framework in which geocells could be incorporated effectively. In order to understand the new mechanistic-empirical approach, the AASHTO Method, the older empirical design method must first be understood.

2.5.1: AASHTO Method

The AASHTO Guide for Design of Pavement Structures, originally published in 1993, presents an empirical design method for flexible pavements based primarily on the AASHO Road Test conducted in Ottawa, Illinois from August 1956 to June 1961. The AASHO Road Test was one of the most comprehensive full-scale pavement tests ever

conducted, and it generated crucial information regarding pavement structural design, performance, load equivalencies, climate effects, and more. In short, many pavement sections were built and subjected to various traffic loading conditions. The serviceability of those pavement structures was monitored with respect to loading conditions, climatic conditions, and other pertinent factors. More details regarding the AASHO Road Test can be found in the Highway Research Board Special Report 61A – 61G

The resultant AASHTO design method for flexible pavements often takes the form of the following equation:

$$log_{10}(W_{18}) = Z_R \times S_0 + 9.36 \times log_{10}(SN + 1) - 0.20 + \frac{log_{10}\left(\frac{\Delta PSI}{4.2-1.5}\right)}{0.40+\frac{1094}{(SN+1)^{5.19}}} + 2.32 \times log_{10}(M_R) - 8.07 \qquad (13)$$

where:

W_{18} = predicted number of 18-kip equivalent single-axle loads (ESALs)

Z_R = standard normal deviate

S_0 = combined standard error of the traffic prediction and performance prediction

SN = structural number; an index indicative of the total pavement thickness required

= $a_1D_1 + a_2D_2m_2 + a_3D_3m_3 + \ldots + a_iD_im_i$

a_i = i^{th} layer coefficient

D_i = i^{th} layer thickness [inches]

m_i = i^{th} layer drainage coefficient (often taken as 1.0 unless there is sufficient justification for a different value)

ΔPSI = difference between initial design serviceability index, PSI_0, and the design terminal serviceability index, PSI_t

M_R = subgrade resilient modulus [psi]

In general, this equation can be solved for any of the variables as long as the others are provided. Typically, an analysis will be performed to determine the number of ESALs that a pavement section can undergo before reaching a given serviceability limit state. Alternatively, the structural number required to withstand a given number of ESALs could be determined. Both approaches are iterative processes involving the calculation of ESALs as a function of the actual traffic loading using the following equation:

$$\frac{W_x}{W_{18}} = \left[\frac{L_{18}+L_{2s}}{L_x+L_{2x}}\right]^{4.79} \times \left[\frac{10^{G/\beta_x}}{10^{G/\beta_{18}}}\right] \times [L_{2x}]^{4.33} \quad (14)$$

where:

W_{18} = number of 18-kip equivalent single-axle loads (ESALs)

W_x = number of single-axle loads with magnitude x

Lx = axle load being evaluated [kips]

L18 = standard 18-kip axle load [kips]

L2 = axle configuration code (1 = single axle; 2 = tandem axle; 3 = triple axle; x = axle load equivalency factor being evaluated; s = code for standard axle = 1)

G = a function of the ratio of loss in serviceability at time, t, to the potential loss taken at a point where $PSI_t = 1.5$

= $\log_{10} [(4.2 – PSI_t) / (4.2 – 1.5)]$

β = a function that determines the relationship between serviceability and axle load applications

$$= 0.4 + [\, 0.081 \cdot (L_x + L_{2x})^{3.23} / (SN + 1)^{5.19} \cdot L_{2x}^{3.23} \,]$$

The AASHTO design method was the standard of practice for many years despite many known drawbacks. This method has a number of limitations, including traffic loading deficiencies, rehabilitation deficiencies, climatic deficiencies, subgrade deficiencies, surfacing material deficiencies, base course deficiencies, truck characterization deficiencies, construction drainage deficiencies, design life deficiencies, performance deficiencies, and reliability deficiencies, (ARA, Inc., ERES Consultants Division 2004). Many of these issues have been addressed with the development of the mechanistic-empirical approach.

2.5.2: Mechanistic-Empirical Pavement Design Guide

2.5.2.1: Mechanistic-Empirical Concept

The Mechanistic-Empirical concept evolved as the coupling of two concepts, the mechanistic design procedure and empirical damage estimation and failure definition. According to the Guide for Mechanistic-Empirical Design of New and Rehabilitated Pavement Structures (referred to hereinafter as the Design Guide), the *mechanistic* term "refers to the application of the principles of engineering mechanics, which leads to a rational design process," (ARA, Inc., ERES Consultants Division 2004). The mechanistic design procedure has three components: 1) the theory used to predict failure or distress, 2) the evaluation of material properties, and 3) the relationship between the magnitude of a particular distress parameter and the damage that should not be achieved to maintain the desired performance level. The theory used to predict distress in the Design Guide is a generalized multi-layered elastic theory discussed at length in *Principles of Pavement*

Design, (Yoder and Witczak 1975). The *empirical* component refers to the damage models used to estimate the pavement damage (e.g. rutting, cracking) as a function of the stresses determined in the multi-layer elastic model. The overall framework for the Design Guide can be summarized by the graphic shown in Figure 17 with the overall goal of determining a suitable pavement structure geometry.

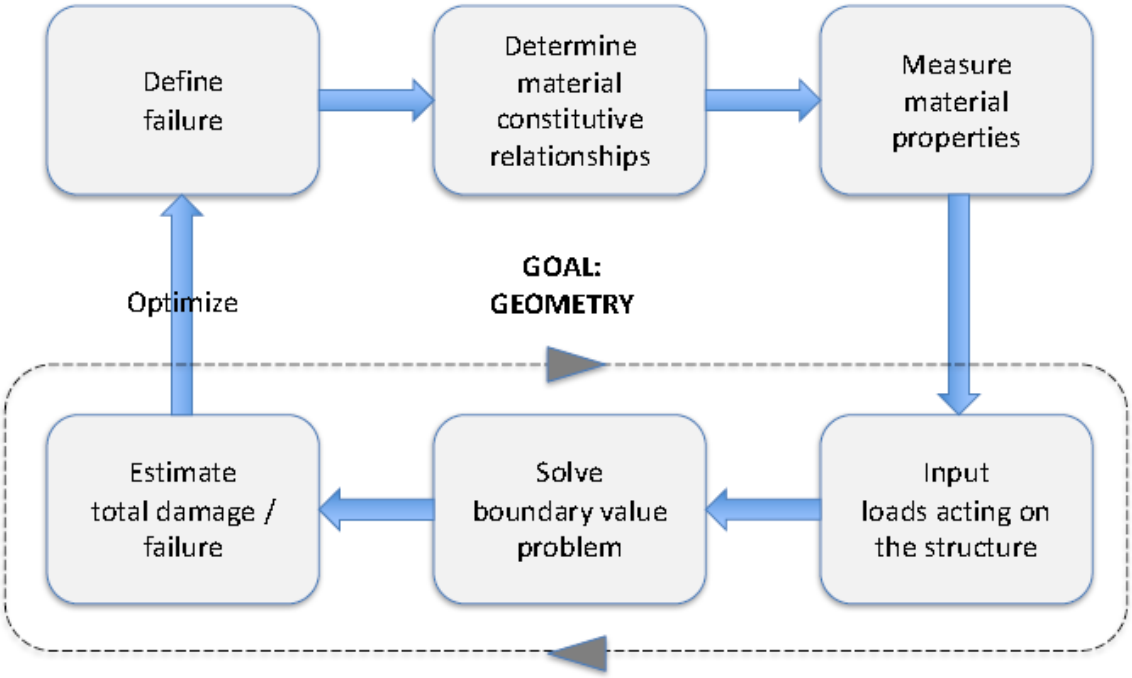

Figure 17. The Mechanistic-Empirical Design Framework, (Bhasin 2017)

The Design Guide is based on the philosophy that the amount of effort that goes into the design should be consistent with the relative size, scale, importance, and cost of the project. As such, a hierarchical system has been introduced to determine the level of design inputs necessary for a particular project. Level 1, the most sophisticated and modern procedure, involves comprehensive laboratory and/or field testing. Level 3, the least involved, requires estimation of the most appropriate design input values with little to no

testing. Inputs at Level 2 are estimated based on correlations to index parameters that are easier and less expensive to measure than the design inputs themselves. The properties described in the following sections correspond to the design inputs for a Level 1 analysis.

2.5.2.2: Defining Failure Criteria

First, failure criteria are defined by an acceptable level of rutting and/or cracking for a particular pavement structure. For typical pavement structures, fatigue damage builds up as repeated cycles of traffic loading are imposed over time. Typical types of pavement distress are grouped into two categories, cracking and rutting. Cracking distresses include meandering, transverse, longitudinal, diagonal, block, crocodile, and crescent-shaped cracks. Cracking failure criteria are often defined in terms of a damage index which is correlated to expected crack widths, crack depths, and/or cracks per unit area. Rutting occurs when there is significant densification and/or lateral movement of material within the pavement structure causing the formation of a depression in the wheel path. The rutting failure criterion is often defined in absolute terms as a maximum rut depth.

2.5.2.3: Material Constitutive Relationships

The material constitutive relationships used in the Design Guide are the models used to quantify the properties of the material components of a pavement structure (i.e. subgrade, base, and asphalt) over a range of conditions. In a Level 1 analysis, the resilient modulus, M_R, is the design input for both base course and subgrade materials. As the base and subgrade are the layers most likely to be reinforced using geocells, they will be the focus of this section. The constitutive model for resilient modulus is often expressed as:

$$M_R = k_1 P_a \left(\frac{\theta}{P_a}\right)^{k_2} \left(\frac{\tau_{oct}}{P_a} + 1\right)^{k_3} \qquad (15)$$

where:

M_R	=	resilient modulus, psi
θ	=	bulk stress = $\sigma_1 + \sigma_2 + \sigma_3$
σ_1	=	major principles stress
σ_2	=	intermediate principle stress = σ_3 for cylindrical tests
σ_3	=	minor principle stress/confining pressure
τ_{oct}	=	octahedral shear stress
	=	$\frac{1}{3}\sqrt{[(\sigma_1 - \sigma_2)^2 + (\sigma_1 - \sigma_3)^2 + (\sigma_2 - \sigma_3)^2]}$
P_a	=	atmospheric pressure (normalizing stress), ~14.7 psi
k_1, k_2, k_3	=	regression constants

The regression constants, k_1, k_2, and k_3, are determined from a linear or nonlinear regression analysis to fit the model to the M_R data generated in the lab. The coefficient, k_1, is proportional to the elastic modulus of the material, and as such the values of k_1 should be positive since the resilient modulus can never be a negative value. The first exponent, k_2, is related to the bulk stress. An increasing bulk stress should stiffen the material resulting in a higher resilient modulus, so k_2 should also be positive. The second exponent, k_3, is related to the octahedral shear stress. Increasing shear stresses will soften the material, so k_3 should be negative. These three values, k_1, k_2, and k_3, are the actual input values for the mechanistic-empirical design process, not the resilient modulus itself as it is an extrinsic, stress-dependent property.

Although not directly applicable to geocell-reinforced soils, it is important to also understand the constitutive model for asphaltic materials used in the Design Guide. Unlike base and subgrade materials, the controlling property used as a design input for asphaltic layers of flexible pavements is the complex modulus, E*. Because asphalt is a thermo-viscoelastic material, it is sensitive to both temperature and the frequency of loading. As

such, the constitutive model for this material, the asphalt “master curve”, must account for those parameters. The asphalt master curve is a sigmoidal function that describes the time dependency of the complex modulus at a reference temperature. This relationship is often presented in terms of the log reduced time, the logarithm of the reciprocal of the loading frequency. Shift factors, then, describe temperature dependency of the complex modulus.

Complex modulus testing is performed at a number of temperatures over a narrow range of loading frequencies, typically 0.1 Hz to 25 Hz, which corresponds to a range of log reduced time values from 1.0 to -1.4. These values are shifted via the shift factors, a(T), to develop the full master curve over a large range of log reduced times as depicted in Figure 18.

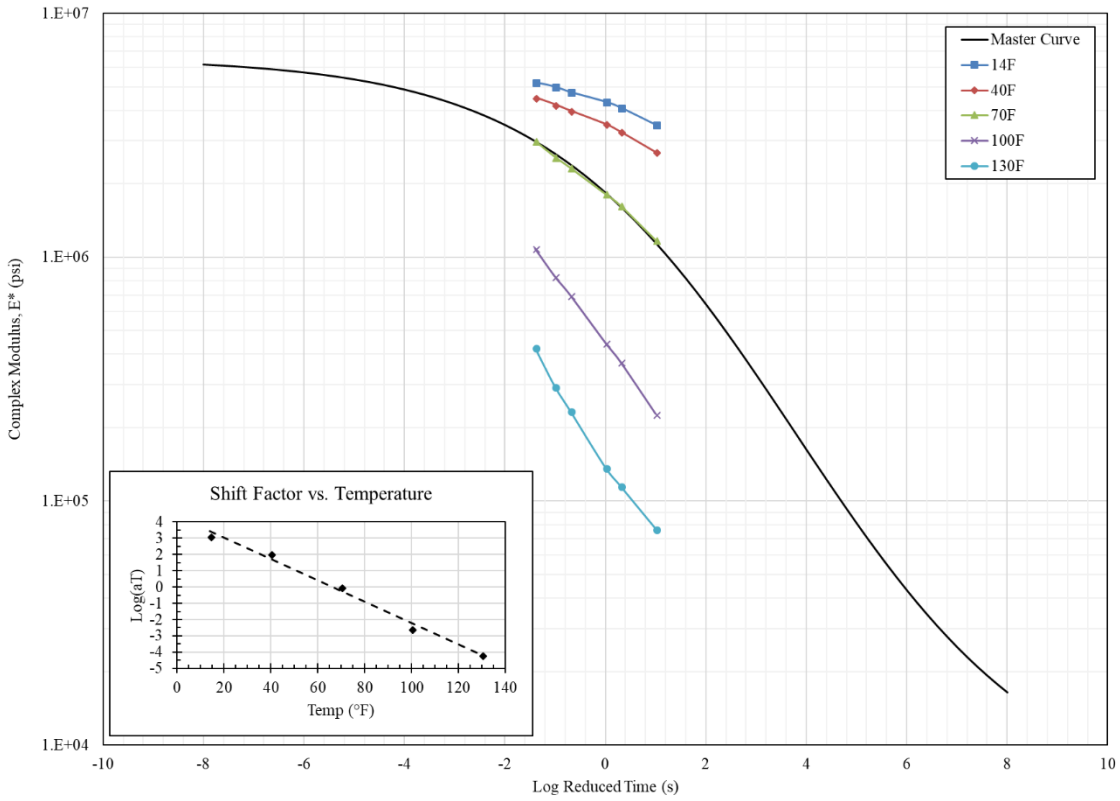

Figure 18. Typical constitutive model for asphalt in flexible pavements, the asphalt master curve with the associated plot of a(T) vs. T

This constitutive model is expressed as a sigmoidal function defined below:

$$\log_{10}|G^*|(\omega) = \delta + \frac{\alpha}{1+\exp(\beta+\gamma \log_{10} \omega)} \qquad (16)$$

where:

E* = complex, or dynamic, modulus measured using uniaxial compression

ω = period of load application, 1/f

δ, α = fitting parameters; for a given set of data, δ represents the minimum value of E* and (δ + α) represents the maximum value of E*

β, γ = parameters describing the shape of the sigmoidal function

The general form of the shift factors is presented below:

$$t_r = \frac{t}{a(T)} \qquad (17)$$

$$\log(t_r) = \log(t) - \log[a(T)] \qquad (18)$$

where:

t_r = time of loading at the reference temperature

t = time of loading at a given temperature of interest

a(T) = shift factor as a function of temperature

T = temperature of interest

2.5.2.4: Measurement of Material Properties

Measuring the material properties as defined in the previous section requires sophisticated laboratory equipment and significant testing time. The Design Guide

recommends two standard test methods for the resilient modulus of unbound granular materials (base) and fine-grained subgrade materials: 1) NCHRP 1-28A, "Harmonized Test Methods for Laboratory Determination of Resilient Modulus for Flexible Pavement Design," (Witczak 2003) and 2) AASHTO T 307-99, "Determining the Resilient Modulus of Soil and Aggregate Materials," (AASHTO 2007). Essentially, both of these tests are repeated load triaxial, or RLT, tests with specific load sequences and parameters for different soil types. Both test methods require that the stress conditions used in the test are representative of the range of stress states likely to develop at the depth of interest beneath flexible pavements subjected to traffic loading.

2.5.2.5: Input Loading Conditions

The input loading conditions for a mechanistic-empirical pavement analysis include four types of traffic data:

- Yearly traffic volume
- Traffic volume adjustment factors such as monthly adjustments, vehicle class distribution, hourly truck distribution, and traffic growth factor
- Axle load distribution factors
- General traffic inputs such as the number of axles/trucks, axle configurations, and wheel base

The level of detail required for a specific project is, as previously mentioned, dependent on the level of analysis. The traffic data required for each of the three hierarchical levels is summarized in Figure 19.

Data Elements/Variables		Input Level		
		1	2	3
Truck Traffic and Tire Factors	Truck directional distribution factor	Site specific WIM or AVC	Regional WIM or AVC	National WIM or AVC
	Truck lane distribution factor	Site specific WIM or AVC	Regional WIM or AVC	National WIM or AVC
	Number of axles by axle type per truck class	Site specific WIM or AVC	Regional WIM or AVC	National WIM or AVC
	Axle and tire spacing	Hierarchical levels not applicable for this input		
	Tire pressure or hot inflation pressure	Hierarchical levels not applicable for this input		
	Truck traffic growth function	Hierarchical levels not applicable for this input		
	Vehicle operational speed	Hierarchical levels not applicable for this input		
	Truck lateral distribution factor	Hierarchical levels not applicable for this input		
	Truck monthly distribution factors	Site specific WIM or AVC	Regional WIM or AVC	National WIM or AVC
	Truck hourly distribution factors	Site specific WIM or AVC	Regional WIM or AVC	National WIM or AVC
Truck traffic distribution and volume variables	AADT or AADTT for base year	Hierarchical levels not applicable for this input		
	Truck distribution/spectra by truck class for base year	Site specific WIM or AVC	Regional WIM or AVC	National WIM or AVC
	Axle load distribution/spectra by truck class and axle type	Site specific WIM or AVC	Regional WIM or AVC	National WIM or AVC
	Truck traffic classification group for pavement design	Hierarchical levels not applicable for this input		
	Percentage of trucks	Hierarchical levels not applicable for this input		

Figure 19. Summary of traffic data required for input into a mechanistic-empirical analysis, (ARA, Inc., ERES Consultants Division 2004)

2.5.2.6: Boundary Value Problem

The boundary value problem is defined by the pavement geometry, layer thicknesses, and input loading. Typically, a multi-layer elastic solution is used to determine the stresses, strains, and displacements throughout the pavement structure induced by the traffic loading. The strains within the pavement structure are then used to estimate total damage to the pavement, a process that will be detailed in the next section. A layered elastic analysis requires a number of assumptions in order to solve the boundary value problem, including:

- Each pavement layer is homogeneous, isotropic, and linear elastic
- Each pavement layer extends infinitely in the horizontal direction
- The bottom layer, either subgrade or bedrock, extends infinitely downward
- The materials are not stressed beyond their elastic range

A number of software packages are available to perform this layered elastic analysis. These include, but are not limited to, Winjulea, Kenlayer, Illi-pave, and Mich-pave. It should be noted that the Design Guide also recommends the use of a nonlinear finite element procedure if it is determined that the stresses due to the input loading will exceed the linear and/or elastic thresholds of either the base or subgrade materials.

A key aspect of solving the boundary value problem is reaching compatibility between the stresses induced by the input loading and the stress-dependent material properties. Recall, the resilient modulus is dependent on both the bulk stress, θ, and the octahedral shear stress, τ_{oct}. Establishing compatibility requires an iterative process. First, initial material properties are selected based on the unloaded stress condition. The first iteration of the layered elastic analysis will yield a new stress condition. A new set of material properties should be determined based on this new stress condition, and the layered elastic analysis should be re-run. This process should continue until there is agreement between the input stress condition and the output stress condition. Some of the available software packages perform this iterative process automatically while others require a manual iteration procedure. Further details regarding the boundary value problem and layered elastic analyses can be found in the Design Guide.

2.5.2.7: Estimating Total Damage & Identifying Failure

The estimation of total damage is the empirical component of the mechanistic-empirical approach. Damage models are used to convert the stresses and strains determined during the layered elastic analysis into different types of damage. Damage, or distress, that occurs in a pavement is divided into two categories, cracking and rutting, which are then subdivided into a number of subcategories depending on the type pavement structure including top-down and bottom-up fatigue cracking and thermal cracking. Different types

of distress are related to stresses and strains in particular locations and orientations, known as critical response variables. The locations of these critical values are dependent on the axle configuration and other factors, but for simple cases, they can be determined by inspection. The critical response variables include:

- Horizontal tensile strain at the bottom and top of the asphalt layer (for asphalt fatigue cracking)
- Vertical compressive stresses/strains within the asphalt layer (for asphalt rutting)
- Vertical compressive stresses/strains within the base layer (for base rutting)
- Vertical compressive stresses/strains at the top of the subgrade layer (for subgrade rutting)

The critical stress and strain responses are converted to incremental distresses that are summed over all loading increments and output at the end of the analysis. Incremental distresses are determined either in absolute terms (for rut depth) or in terms of a damage index (for fatigue cracking).

2.5.3: Modification of Resilient Modulus for Geocells

The inclusion of a geocell-reinforced soil layer into the mechanistic-empirical design process is the ultimate goal of this research trajectory, which has been initiated with the research components completed in this thesis. Using the MEPDG framework, the design of pavement structures using geocell reinforcement would be theoretically-sound and compatible with modern pavement design. As geocells are most commonly used to reinforce unbound aggregate materials, geocells would most effectively be used to reinforce the base course layer of a pavement structure, especially with the presence of weaker underlying subgrades. As mentioned in previous sections, the material constitutive

relationship used for base course in mechanistic-empirical analyses is the resilient modulus. It follows that an analytical model for the reinforced resilient modulus of geocell-reinforced unbound aggregate materials would best fit into the mechanistic-empirical design approach. Some researchers have already begun to develop models for the determination of geocell-reinforced resilient moduli.

2.5.3.1: Reinforced Resilient Modulus

Yang and Han (2013) presented an analytical model for the resilient modulus and permanent deformation of geosynthetic-reinforced unbound granular material using both geogrids and geocells. The goal of their model was to eliminate the need for RLT testing on geosynthetic-reinforced materials due to the additional complexity involved compared to testing soil alone. Eliminating this time-intensive and expensive requirement would allow for broader acceptance and easier implementation of a mechanistic-empirical design method for geocell-reinforced pavement structures.

The Yang & Han Model for the resilient modulus of geocell-reinforced soil has three components: 1) a stress-dependent resilient modulus model for the unbound granular material (the same model used in the Design Guide); 2) a permanent deformation model for the unbound granular material after Tseng and Lytton (1989); and 3) a linear-elastic model for the geosynthetic material.

The permanent deformation model takes the form of Equation 19 below where $(\varepsilon_0/\varepsilon_r)$, ρ, and β are permanent deformation parameters determined by fitting the measured permanent deformation test curve. The form of Equation 19 implies that the permanent deformation reaches a constant state (i.e. a resilient state) when the number of cycles, N goes to ∞. However, it is often necessary to set a limit of N cycles (typically around 10^5)

to prevent ($\varepsilon_0/\varepsilon_r$) from reaching unreasonably large values if the measured permanent deformation curve does not approach a constant value during testing.

$$\frac{\varepsilon_{1,p}}{\varepsilon_{1,r}} = \left(\frac{\varepsilon_0}{\varepsilon_r}\right) e^{-(\rho/N)^{\beta}} \quad (19)$$

It is important to note this model assumes that the applied stress level does not exceed the shakedown limit of the material and that the sample will reach the resilient state, the state in which all resilient strain, $\varepsilon_{1,r}$, generated in the loading period will be recovered in the unloading period. While in this state, the stress-strain relationship can be described using Equation 20:

$$\varepsilon_{1,r} = \frac{\sigma_1 - \sigma_3}{M_r} \quad (20)$$

The Yang & Han Model breaks down a single load cycle of the RLT test into two loading stages defined by the level of axial stress applied to the specimen. The first stage starts at the beginning of a load cycle, when the axial stress is equal to the confining pressure, $\sigma_a = \sigma_3$, and ends after the axial stress increases by the amount of additional confinement provided by the geocell, $\sigma_a = \sigma_3 + \Delta\sigma_3$. During the first stage, the bulk stress and octahedral shear stress are defined by Equations 21 and 22, respectively:

$$\theta = \sigma_3 + 2(\sigma_3 + \Delta\sigma_3) = 3\sigma_3 + 2\Delta\sigma_3 \quad (21)$$

$$\tau_{oct} = \frac{\sqrt{2}}{3}\Delta\sigma_3 \quad (22)$$

The second stage starts after the first, where $\sigma_a = \sigma_3 + \Delta\sigma_3$, and continues until the end of the loading cycle when the axial stress reaches the designated maximum stress, $\sigma_a = \sigma_1$. During this stage, the bulk stress and octahedral shear stress are defined by Equations 23 and 24, respectively:

$$\theta = \sigma_1 + 2(\sigma_3 + \Delta\sigma_3) \qquad (23)$$

$$\tau_{oct} = \frac{\sqrt{2}}{3}[\sigma_1 - (\sigma_3 + \Delta\sigma_3)] \qquad (24)$$

For each of the two loading stages, the reinforced specimen has a unique resilient modulus as it is dependent on the stress state, θ and τ_{oct}. The full resilient stress-strain relationship of the geosynthetic reinforced sample is be determined by combining the two stages into Equation 25:

$$\varepsilon_{1,r} = \frac{\Delta\sigma_3}{M_{r,1}} + \frac{\sigma_1 - (\sigma_3 + \Delta\sigma_3)}{M_{r,2}} = \frac{\sigma_1 - \sigma_3}{M_{r,reinf}} \qquad (25)$$

Combining this equation with the permanent deformation model yields Equation 26, an expression of the overall permanent axial deformation in the resilient state, $\varepsilon_{1,p}$.

$$\varepsilon_{1,p} = \left[-\frac{\Delta\sigma_3}{M_{r,1}} + \frac{\sigma_1 - (\sigma_3 + \Delta\sigma_3)}{M_{r,2}}\right] \times \left(\frac{\varepsilon_0}{\varepsilon_r}\right) e^{-(\rho/N_{max})^{\beta}} \qquad (26)$$

The contribution of the geocell to the overall performance of the specimen is quantified by the additional confinement, $\Delta\sigma_3$, it provides. Incorporating the diameter of the geocell, D, the linear-elastic stiffness model for the geocell material, $M = \sigma / \varepsilon$, and the permanent radial or lateral strain, $\varepsilon_{3,p}$, the additional confinement can be determined using hoop stress theory, after (Emersleben and Meyer 2009). The result is Equation 27:

$$\Delta\sigma_3 = \frac{2M}{D} \cdot \left(-\varepsilon_{3,p}\right) \qquad (27)$$

In order to obtain the permanent lateral strain, a relationship is needed between $\varepsilon_{3,p}$ and the resilient vertical strain, $\varepsilon_{1,r}$. The authors assumed that, while in the resilient state, no plastic volumetric strains occur within the specimen. As such, the permanent lateral strain on the specimen is equal to –½ of the permanent axial strain. Assuming constant dilation, ψ, the permanent lateral strain can be expressed as Equation 28:

$$-\varepsilon_{3,p} = \frac{1}{2}\varepsilon_{1,p}\left(\frac{1+\sin\psi}{1-\sin\psi}\right) \qquad (28)$$

Altogether, the additional confinement provided by the geocell-reinforcement can be expressed as Equation 29:

$$\Delta\sigma_3 = \frac{M}{D}\left[-\frac{\Delta\sigma_3}{M_{r,1}} + \frac{\sigma_1-(\sigma_3+\Delta\sigma_3)}{M_{r,2}}\right] \times \left(\frac{\varepsilon_0}{\varepsilon_r}\right) e^{-(\rho/N_{max})^{\beta}} \left(\frac{1+\sin\psi}{1-\sin\psi}\right) \qquad (29)$$

In order to validate their model, the authors used data obtained from a large-scale resilient modulus testing apparatus, Figure 20, developed by Mengelt et al. (2001, 2006) for the purpose of determining the resilient modulus and permanent deformation parameters of geogrid- and geocell-reinforced unbound aggregates. This apparatus and associated loading sequence used in testing conform to AASHTO T 294-94, the predecessor of AASHTO T 307-99.

Figure 20. Large-scale resilient modulus testing apparatus: (a) side view of assembled cell; (b) top view of unassembled cell with specimen confined in geocell

2.5.3.2: Limitations of the Yang & Han Model

While the Yang & Han Model for the resilient modulus of geocell-reinforced unbound aggregate materials is a significant foray into the development of a geocell design methodology, it has a number of limitations that may be important for the implementation of the model in flexible pavement design. First, as noted by the authors, the Yang & Han model is specifically formulated to predict the response of geocells in a modified RLT testing apparatus. While RLT testing is the preferred resilient modulus testing procedure for unreinforced unbound granular materials according to the Design Guide, it may not be as applicable for a reinforced specimen that relies on significant contributions from global mechanisms for its overall strength and stiffness.

The modified RLT apparatus depicted in Figure 20 holds a soil specimen confined with a single geocell. Note that the geocell depicted in Figure 20b is stretched to be nearly circular in shape. In field applications, standard commercial geocells have a shape often described as honeycomb-like, as depicted in Figure 21. Overstressing a geocell into a circular shape, as done by Mengelt et al. (2001, 2006), may impart additional confining stresses to the soil specimen not representative of field conditions. Even fully-loaded cells in the field would not deform into a circular shape, and even if they did, it would cause the collapse of adjacent cells reducing the overall strength and stiffness of the reinforced mattress.

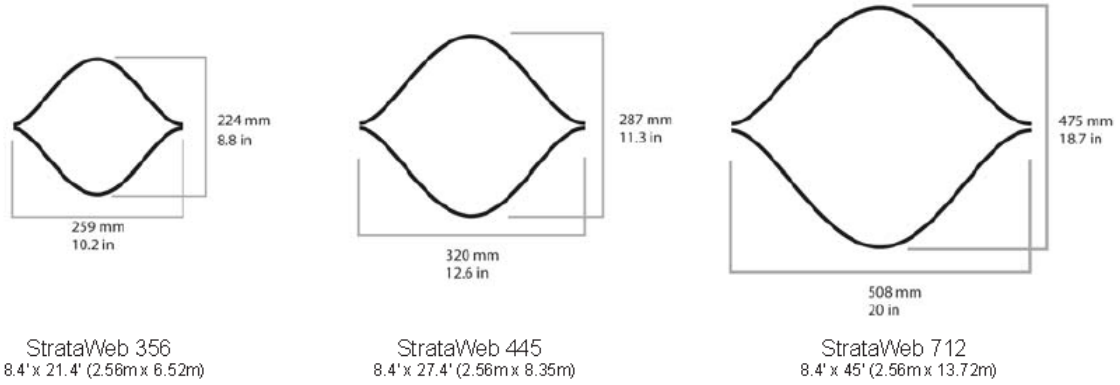

Figure 21. Typical shape and dimensions of commercially-available geocells, Strata Systems, Inc.

Additionally, the single-cell resilient modulus testing does not accurately simulate the interconnected matrix present in a full geocell section. Geocells likely respond to the loading of soil in adjacent cells differently than unreinforced soil would. The interaction between adjacent cells in a geocell matrix is one of the reinforcement mechanisms that is poorly understood. The use of transparent soil is expected to allow for close observation of these interactions.

Another important limitation of this overarching framework is that the model used to relate the resilient strain to plastic strain is empirical and based on observations of typical base materials that do not include geocell reinforcement. Therefore, such an approach must be used with caution and would require calibration. Calibration of the model would involve large-scale RLT testing of geocell reinforced base materials, with appropriate cell expansion, and additional large-scale field evaluations.

2.5.3.3: Addition of Tensioned Membrane Effect

One specific limitation of the Yang & Han Model for geocell-reinforced resilient modulus is the lack of a component due to the tensioned membrane effect. As mentioned in previous sections, the tensioned membrane effect may only be applicable to geocell reinforcement when significant bending/rutting occurs. The small strains induced by a single wheel pass may not be significant enough to warrant the inclusion of a tensioned membrane component for some applications. However, for unpaved roads or temporary roads where ride quality is not of major concern, significant performance gains may be realized if rutting is allowed to reach a level at which significant tensile stresses exist within the geocell matrix provided the geocell material does not relax under constant tension.

In this context, a tensioned membrane component should be included in the analysis procedure during the boundary value problem iteration to reach a strain-compatible state. Vertical compression (i.e. rutting) could be used to determine the deformed shape of the geocell mattress which translates into a tensile stress in the geocell material. This would, in turn, contribute to a greater overall stress state. As the resilient modulus is a stress-dependent material property, an increase in the bulk stress or decrease in the octahedral shear stress would result in an increase in the resilient modulus.

2.5.3.4: Addition of Passive Pressure from Adjacent Geocells

As mentioned above, the interaction between a loading cell and adjacent cells in a geocell matrix is an important, but poorly understood, mechanism contributing to the overall performance of geocell-reinforced soil. In addition to the vertical stress dispersion that transfers vertical stresses from the top of a geocell-reinforced layer to a wider area at the bottom, some of the load is transferred laterally to the side walls of the loaded cell. This confinement is often characterized as a hoop stress in the geocell due to radial expansion and tensile stresses, as in the Yang & Han Model. However, this characterization ignores the response of soil in cells adjacent to the loaded cell to that radial expansion. Considering the principle of passive earth pressure, the resistance of adjacent soil particles to outward movement could be characterized as a component of the potential passive earth pressure. As above, the increase in bulk stress on the infill material would correspond to an increase in the resilient modulus as defined in the Design Guide.

Typical passive earth pressure theories, such as Rankine (1847), Coulomb (1776), and log spiral (Terzaghi 1943), are based on limit equilibrium procedures, (Cole and Rollins 2006). It is also accepted that more displacement is required to mobilize the full passive earth pressure force than the active earth pressure force. With these considerations, the expected additional confining pressure on soil within a loaded geocell due to the passive pressure of soil in adjacent cells may be very small, if not negligible, especially relative to the contribution to the hoop stress in a stiff geocell material. However, geocells with a lower tensile stiffness may experience significantly more radial expansion, and therefore, may develop significantly more passive resistance. A robust geocell design method should account for both the tensioned membrane effect and the passive resistance of soil in adjacent cells. Both of these mechanisms can be translated into a greater confining stress

on the infill soil leading to a greater calculated resilient modulus for the mechanistic-empirical analysis.

The use of transparent soil will be crucial for the direct observation of these mechanisms. Transparent soil will, in theory, allow for the observation of the bending of the geocell mattress under load which can be used to determine tensile strains within the geocell matrix. Transparent soil will also allow for the measurement of radial expansion of loaded cells and the response of adjacent cells. These observations will add to the current understanding of geocell behavior and reinforcement mechanisms for the development of a robust design methodology.

2.6: TRANSPARENT SOIL

2.6.1: Transparent Soil Concept

As previously mentioned, transparent soils are two-part media consisting of a transparent particulate solid and a clear saturating fluid. If these two media have matching refractive indices, light will pass through the combined medium without reflecting or refracting off of any surfaces or facets giving outside observers the ability to visualize the movement of individual soil particles and the interaction between those particles and other objects. There are a number of families of transparent soils that are used to simulate many different soil types and conditions. In addition, there are numerous analysis methodologies and visualization techniques that can be used to extract all available data from experiments.

2.6.2: Families of Transparent Soil

As a growing technology with potential to provide unique and novel insights, there have been multiple reviews and summaries of transparent soil technologies and techniques in geotechnical applications published in recent years, (Ganiyu et al. 2016, Iskander et al.

2015, Iskander et al. 2016). There are five main families of transparent soil that have been used for geotechnical research including silica powder, silica gel, Aquabeads, fused quartz, and Laponite ®. Of these, fused quartz and Laponite ® have been mostly commonly utilized in recent research applications.

2.6.2.1: Fused Quartz

Fused quartz, also referred to as fused silica, is a granular soil surrogate that has been used in many recent geotechnical research applications, (Ferreira 2013, Ferreira and Zornberg 2015, Bathurst and Ezzein 2015, Peng and Zornberg 2016, 2017). The solid particles are a non-crystalline form of silicon dioxide manufactured by melting natural silica at over 2000°C in a vacuum to prevent the formation of bubbles. This material is crushed to particle sizes consistent with typical sands and gravels. Three different saturating fluids have been used with fused quartz including mineral oil, a sucrose solution, and a solution of sodium thiosulfate-treated sodium iodide (STSI). The water-based solutions are advantageous due to their lower viscosities and lower sensitivity to temperature fluctuations. Both mineral oil and STSI pore fluids can be recycled for multiple tests, but STSI is much more expensive than the mineral oils. Because of the application of geocells in the reinforcement of unbound aggregate bases, fused quartz is an ideal material to use for transparent soil evaluations of geocell-reinforcement mechanisms and behaviors.

2.6.3: Transparent Soil Techniques

2.6.3.1: Qualitative Visualization and Observation

The first and most basic application of transparent soil is the direct observation and qualitative characterization of soil-reinforcement interaction. In experiments with normal

soil and careful exhumation procedures, the post-failure, post-test stage of in-situ conditions can be observed in some geotechnical experiments. Unlike those typical geotechnical experiments, a transparent medium allows for the visualization of material in-situ during every stage of loading. The observation of non-transparent objects acting on the transparent soil, such as cone penetrometers, geogrid reinforcement, and projectiles, allows for previously hidden phenomena to be revealed.

2.6.3.2: Tracking Particles and Seeding

The next step beyond the direct observation of non-transparent objects acting upon the transparent soil is the observation of the motion of individual particles in response to perturbation. To this end, opaque soil particles have been used to track the displacement of individual soil particles within a transparent fused quartz soil mass, (Ferreira and Zornberg 2015). In other applications, such as the use of Laponite ® as a clay surrogate, reflective seeding particles have been used to provide contrast and texture within the transparent soil mass, (Black 2015).

2.6.3.3: Laser Plane Illumination

Planar lasers have also been used to illuminate individual planes of transparent soil particles within a transparent soil mass, either to take advantage of reflections off of individual fused quartz particles or to better illuminate the reflective seeding particles. This technique, when used appropriately, yields measurements with higher precision and resolution for displacement and strain contour maps than the use of opaque seeding particles due to the full-field illumination.

2.6.3.4: Digital Image Correlation

Digital Image Correlation, DIC, is a common pattern recognition technique used frequently in association with transparent soil applications, (Iskander et al. 2015, Ganiyu et al. 2016). There are several commercial and open-source codes available to run DIC analyses. These analyses require a consistent texture within an image so that the code can identify unique clusters of pixels and track their movement in sequential images.

2.7: SUMMARY OF LITERATURE REVIEW

The main points resulting from the preceding literature review are as follows:

- Geocells are a growing subclass of geosynthetics that can be used for many different applications such as erosion control, channel lining, retaining wall construction, general bearing capacity improvement, and the reinforcement of pavement structures, especially base and subgrade materials.
- Geocell-reinforced soil performance, especially in the context of pavement reinforcement, is dependent on a number of factors such as loading condition, geocell pocket dimensions, geocell mattress dimensions, overall pavement profile geometry, infill and subgrade material properties, and geocell material properties.
- The overall performance of geocell-reinforced soil can be accounted for by varying levels of contribution from different reinforcement mechanisms, namely the confinement effect, the vertical stress dispersion effect, and the tensioned membrane effect. The relative contribution of each mechanism is dependent on the loading condition, strain level, and other factors.
- Some design methodologies have been developed for geocell-reinforced soil, but most are either empirical and therefore limited in applicability, or they are specifically suited to strength limit state bearing capacity applications.

- Currently, there are no design methodologies that fully account for the physical reinforcement mechanisms associated with geocells, nor is there an accepted methodology for the design of geocell-reinforced flexible pavement systems. The MEPDG is a robust framework in which to incorporate such a design methodology and specifically account for the expected loading conditions for pavement structures.
- Transparent soil, specifically fused quartz saturated with mineral oil, will be a valuable technology for in-situ observation of geocell behaviors and mechanisms prior to, during, and after loading.

Chapter 3: Materials and Equipment

3.1: MATERIALS

3.1.1: Geocell Test Sections

Geocell test sections manufactured from three different materials were obtained for this study. The first variety is a textured HDPE geocell, a typical material for commercially-available products. In order to take full advantage of the transparent soil capabilities, a transparent PVC geocell developed by Strata Systems, Inc. was obtained. A third variety of geocells, an untextured HDPE geocell, was also obtained to account for the contribution of texturing on the performance of geocell reinforcement. The full test section size was selected to fit into a 1219 mm x 1219 mm (48 in x 48 in) square plan area. This resulted in a full-sized test section consisting of a 4x4 matrix of cells as depicted in Figure 22. The ½ and ¼ fractional size test sections consist of 8x8 and 16x16 matrices of cells of the corresponding size. A summary of all varieties of test sections obtain for the proposed parametric evaluation is included in Table 1.

The test sections were custom-made in a variety of sizes for use in the proposed parametric study. The weld-spacing and h/d_e selections were based on a standard Strata Systems product, StrataWeb 356 or SW356, with nominal expanded cell dimensions of 259 mm x 224 mm and standard available height-to-equivalent diameter (h/d_e) ratios of 1.0, 1.3, 1.9, and 2.6. Fractional sizes of SW356 were selected in order to determine the effect of footing width to cell diameter (B/d_e) ratios. The (h/d_e) ratios were selected to be less than the standard ratios in an attempt to promote exaggerated failure mechanisms, in particular the tensioned membrane effect. Three different weld spacings were used (356 mm, 178 mm, and 89 mm) with three (h/d_e) ratios (0.4, 0.8, and 1.6). As such, each

fractional size of test section had three cell depths corresponding to the three standard aspect ratios.

Table 1. Dimensions of geocell test sections

Parameter	Unit	SW356 (GC 1)	SW178 (GC 2)	SW89 (GC 3)
Fractional Size	(-)	1	½	¼
Weld Spacing	mm (in)	356 (14)	178 (7)	89 (3.5)
Nominal Expanded Cell Size (width x length)	mm (in)	259 (10.2) x 224 (8.8)	129.5 (5.1) x 112 (4.4)	64.8 (2.6) x 66 (2.2)
Nominal Expanded Cell Area	cm^2 (in^2)	289 (44.8)	144.5 (22.4)	72.3 (11.2)
Equivalent Diameter (d_e)	mm (in)	190.2 (7.5)	95.1 (3.7)	47.6 (1.9)
Cell Depths	mm	300, 150, 75	150, 75, 38	75, 38, 19

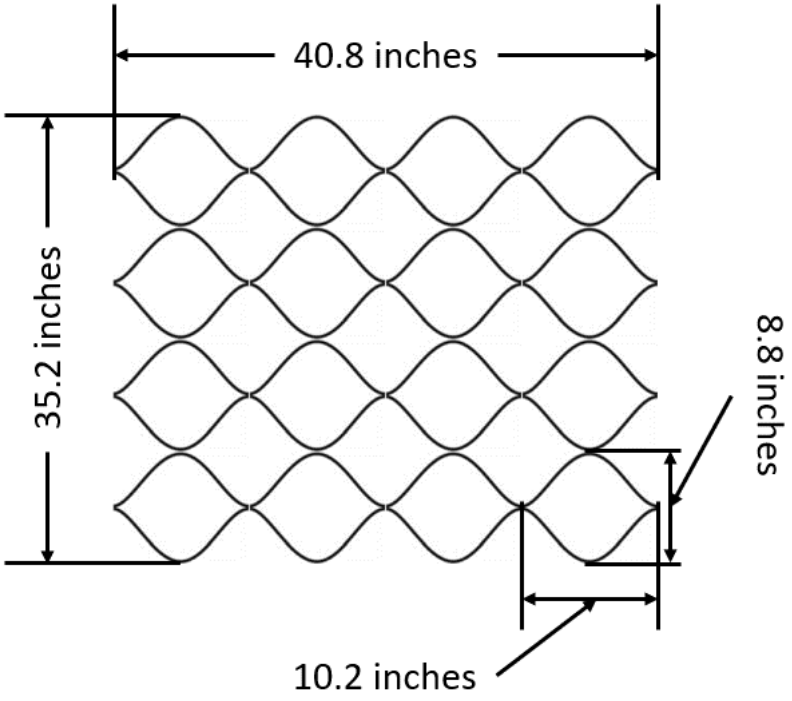

Figure 22. Full-size GC 1 test section

3.1.1.1: Textured HDPE Geocells

The standard commercially-available geocells are typically manufactured from a high-density polyethylene (HDPE) with a nominal thickness of 1.8 mm. These geocells are textured with rhomboidal indentations and perforated with holes to allow soil particle interlocking and groundwater flow. Extruded strips of textured HDPE are thermally welded together at designated intervals so that, when expanded, the section creates the typical honeycomb pattern, Figure 23.

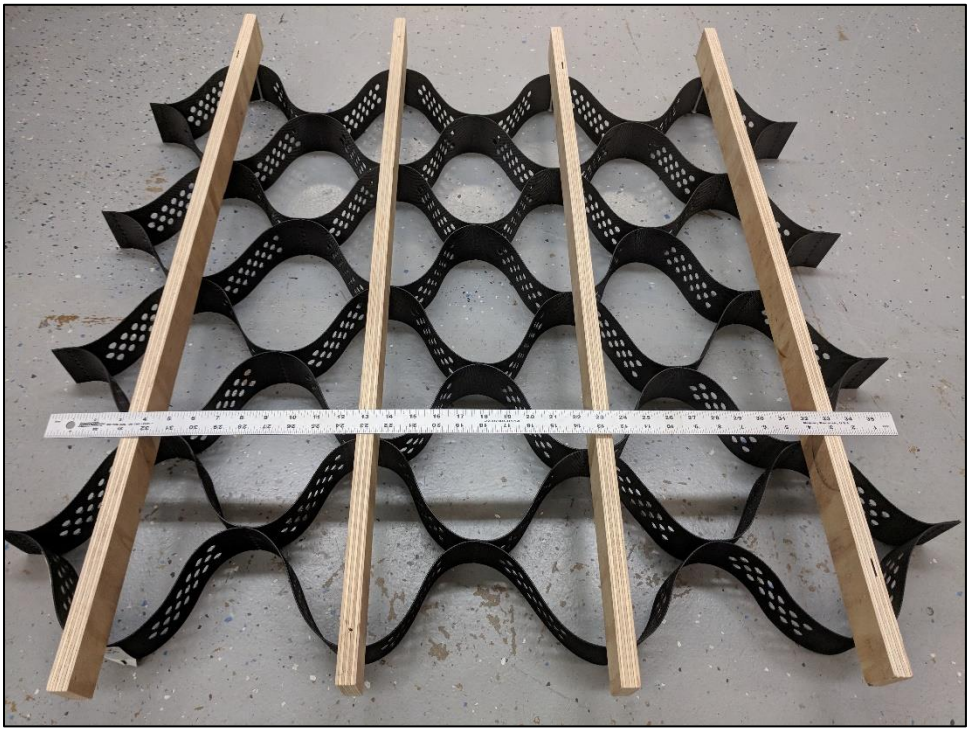

Figure 23. Textured HDPE test section of GC 1 with 150-mm depth, ($HDPE_t$ GC 1-150)

The HDPE has documented material properties including polymer density (0.935 – 0.965 g/cm^3), environmental stress crack resistance (> 400 hours), carbon black content (1.5% by weight minimum), and nominal sheet thickness after texturing (1.52 mm -5%, +10%). The welds have a seam peel strength of 80 lbs/in (per U.S. Army Corps of

Engineers Technical Report GL-86-10, Appendix A). The rhomboidal indentations have a surface density of 22 – 31 per cm^2. The perforations are in horizontal rows, 10-mm in diameter, 16.6 mm on center. Horizontal rows are staggered and separated 8.3 mm relative to hole centers. The perforations correspond to a minimum 11% ± 2% and maximum 16% ± 3% of the side wall area, depending on cell depth. Perforations were not made in the test sections with the smallest depths due to side wall area restrictions.

3.1.1.2: Transparent PVC Geocells

The transparent PVC geocells, Figure 24 and Figure 25, have nominal sheet thickness of 2.2 mm. The seam peel strength is approximately 20% that of the HDPE test sections. The PVC test sections are smooth without the typical rhomboidal texturing, but they have the same number and spacing of perforations as the other sections.

Because the transparent PVC geocells are significantly less stiff than the HDPE geocells, it is expected that they will perform significantly worse than the commercial products. The lower stiffness will also exaggerate some of the reinforcement mechanisms allowing for easier identification and quantification during the full parametric evaluation. The relative contribution of each reinforcement mechanism may be stiffness dependent, so this will be an important factor to consider in the analysis.

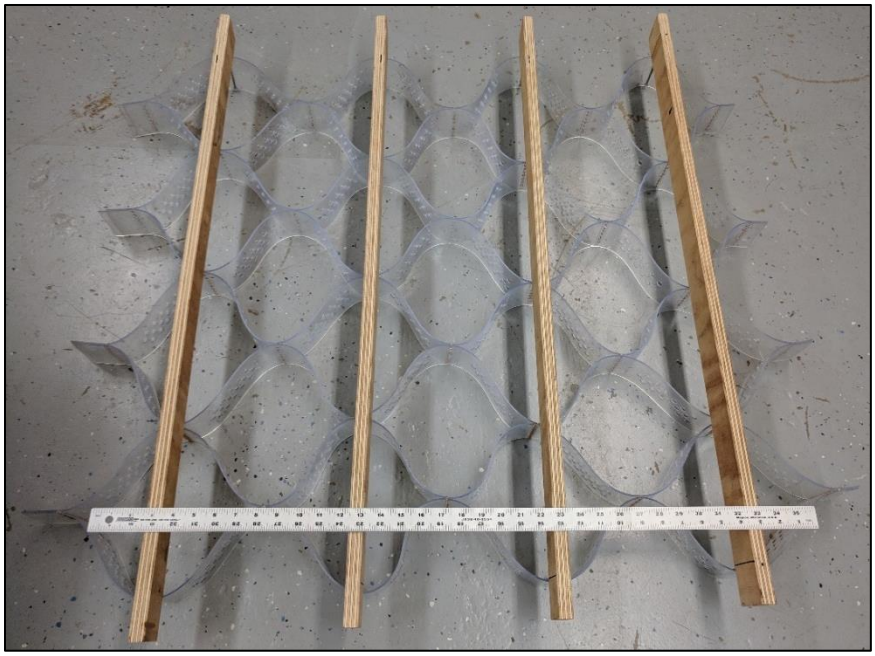

Figure 24. Transparent PVC geocell test section of GC 1 with 150-mm depth (PVC GC 1-150)

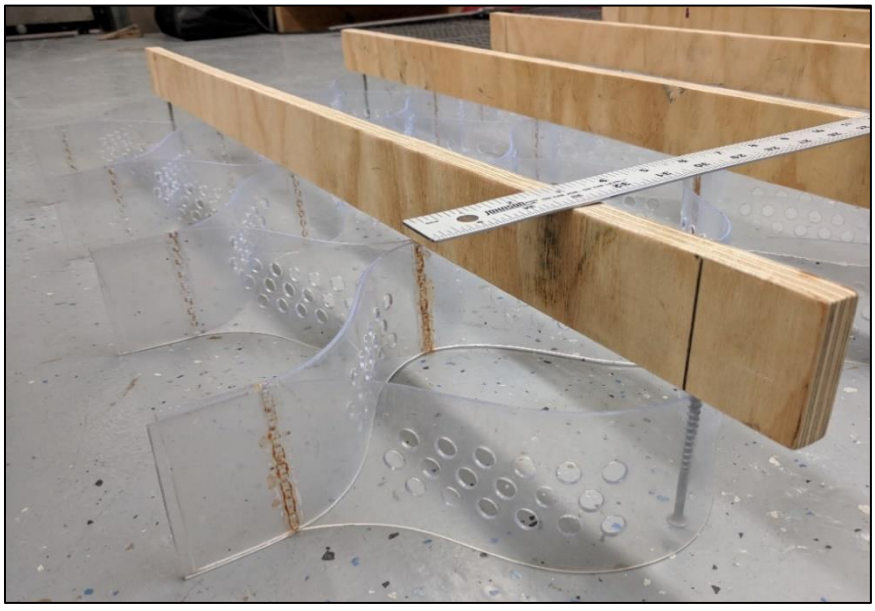

Figure 25. Close-up view of PVC GC 1-150

3.1.1.3: Smooth HDPE Geocells

Because the interface friction between the infill soil and the geocell side walls has been shown to be a critical factor in the performance of geocells, it is predicted that the smooth texture of the transparent PVC geocells will also contribute to their poor performance relative to the HDPE geocells. As such, smooth HDPE geocells of equivalent dimensions to the other geocell tests sections have also been obtained to quantify the impact of texturing on geocell performance. The relative difference between the textured and smooth HDPE geocells will be isolated and removed from the comparison between the stiff HDPE and the soft PVC.

3.1.2: Transparent Soil

3.1.2.1: Crushed Fused Quartz

This study is one of, if not the, largest transparent soil experiments by volume ever conducted. As such, a very large quantity of fused quartz had to be sourced and processed into a usable product. Certain overseas manufacturers, mainly in China, can provide processed fused quartz particles in a range of grain size distributions, but due to the large quantity required the cost was prohibitive. Instead, a specialized glass producer, Heraeus Quarzglas was found with a facility in Austin, Texas. Heraeus manufactures a wide range of optical glass products for many applications including semi-conductor and solar panel manufacturing as well as many optical applications. The company has multiple product lines of fused quartz and fused silica with well-defined parameters and tolerances. Heraeus was able to supply scrap fused quartz tubes and other pieces in large quantities.

In particular, the fused quartz obtained from Heraeus was from the HOQ 310 product line, typically used for applications in the technical optics field. HOQ 310 fused quartz has mechanical properties available on record including density (2.2 g/cm^2), elastic

modulus (7.25 x 10^4 N/mm^2), Poisson's ratio (0.17), compressive strength (1150 N/mm^2), tensile strength (~50 N/mm^2), and Knoop hardness (5800-6200 N/mm^2). The refractive index and dispersion of HOQ 310 are characterized by the properties listed in Table 2, (Heraeus 2016).

Table 2. Optical properties of Heraeus HOQ 310 Fused Quartz

Property	Value
n_c (λ = 656.3 nm)	1.45646
n_d (λ = 587.2 nm)	1.45856
n_f (λ = 486.1 nm)	1.46324
n_g (λ = 435.8 nm)	1.46681
Abbe-Constant, $v_d = (n_d - 1) / (n_f - n_c)$	67.7 ± 0.5
Principal Dispersion, $n_f - n_c$	0.00678

The scrap material obtained from Heraeus had to be crushed, cleaned, and sieved to create a suitable granular soil surrogate. The target grain size distribution for the crushed fused quartz was based on a truncated AASHTO #8 aggregate, with no particles passing a #8 sieve (2.36 mm) and no particles retained on a 3/8" sieve (9.5 mm), with a uniformity coefficient, C_u = 1.5, coefficient of curvature, C_c = 1.0, and USCS classification of GP, poorly-graded gravel. The grain size distributions of standard AASHTO #8 and the truncated AASHTO #8 are presented in Figure 26. This target gradation was selected because similar aggregates and previous transparent soil batches have been used in geogrid pullout testing, (Peng and Zornberg 2016, 2017), and it is representative of typical unbound granular materials reinforced with geocells.

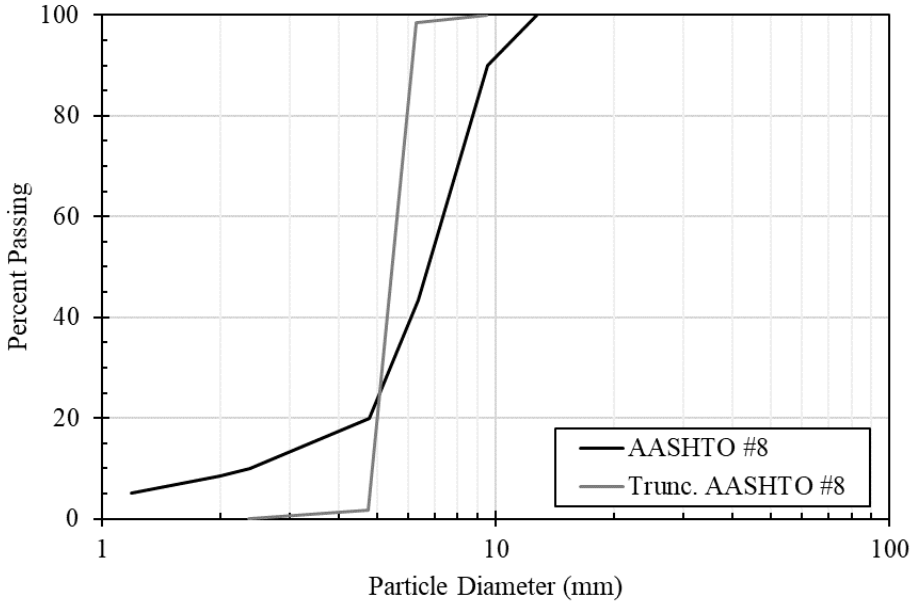

Figure 26. The target grain size distribution for the crushed fused quartz transparent soil and its parent gradation

In order to crush the large quantities of scrap fused quartz required to supply to large-scale testing, an industrial recycling center in Bosque County, Texas was found with a GP-Mega Mini glass pulverizer from Andela Products Ltd., Figure 27. The GP-Mega Mini has a 0.5 ton/hour capacity and outputs the cullet (raw crushed glass) in a typical gradation depicted in Figure 28, (Andela Products Ltd. 2017). It should be noted that the crushed fused quartz is very angular, a characteristic that may have a significant impact on the unreinforced soil strength and the interface friction between the soil and the geocell side walls.

Figure 27. GP-Mega Mini glass pulverizer at the Bosque County Recycling Center

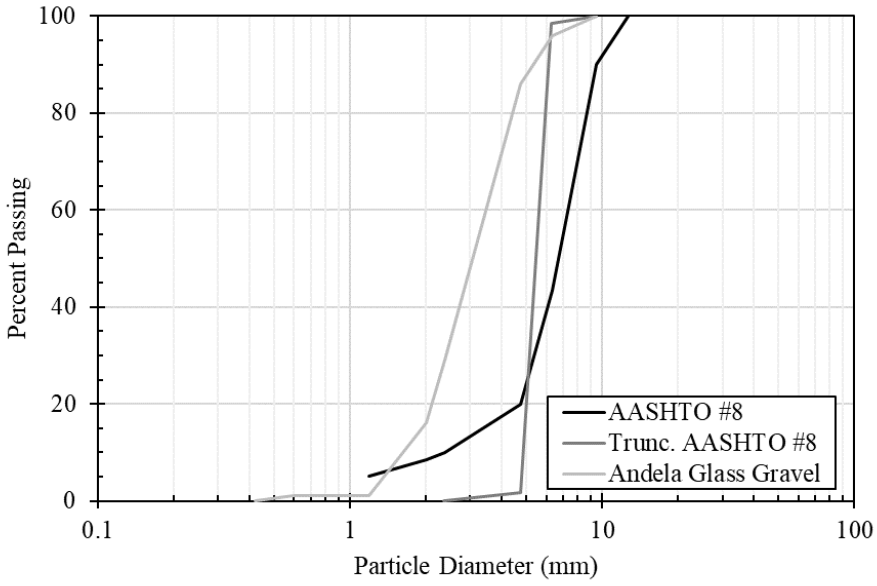

Figure 28. Gradation of GP-Mega Mini glass pulverizer in comparison to target gradation

This output gradation has a significantly higher proportion of particles with diameters smaller than a standard #8 sieve, over 29% by weight, so all of the raw crushed fused quartz had to be sieved to remove particles larger than a 3/8” sieve (9.5 mm) and smaller than a #8 sieve (2.36 mm). In addition, despite the best efforts of the Bosque County Recycling Center staff, some contaminants were introduced into the crushed fused quartz supply during the crushing process. It was found that wet sieving the raw material through a high-capacity #4 aggregate sieve was the most efficient approach to truncate the gradation and remove the majority of contaminants. A visual comparison of the raw and processed fused quartz cleaned and sieved in this fashion is presented below in Figure 29.

Figure 29. Processed (left) and raw (right) crushed fused quartz

The final product after sieving and rinsing had a grain size distribution with slightly more particles passing a #8 sieve than originally desired, approximately 6%, as depicted in

Figure 30. The final gradation had a uniformity coefficient, C_u = 2.2, coefficient of curvature, C_c = 0.8, and USCS classification of SP, poorly-graded sand with gravel. This was determined to still be representative of soil types typically reinforced with geocells for pavement construction. In addition, further sieving would have reduced the overall supply of processed fused quartz to an undesirable level.

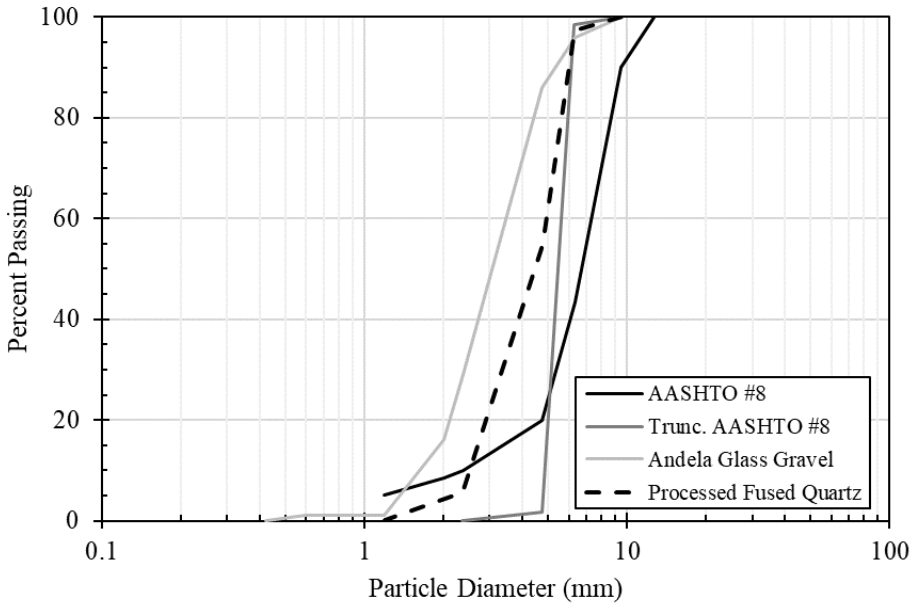

Figure 30. Comparison of final grain size distribution to target grain size distribution

Other geotechnical properties of fused quartz are summarized in Table 3. Note that these values were determined for a different batch of fused quartz with a slightly finer grain size distribution, but it is assumed that the properties are nominally the same. Direct shear and/or triaxial testing should be performed in the future to confirm this assumption.

Table 3. Geotechnical properties of fused quartz, after (Peng and Zornberg 2016)

Property	Test Method	Value
Specific gravity (20°C)	ASTM D854	2.203
Maximum-index dry density	ASTM D4253	1.336 (g/cm^3)
Minimum-index dry density	ASTM D4254	1.203 (g/cm^3)
Friction angle (dry)	ASTM D3080	45°
Friction angle (oil-saturated, drained)	ASTM D3080	44°

3.1.2.2: White Mineral Oil Mixture

The saturating fluid selected for this large-scale application is based on the prior experience with transparent soils, (Ezzein and Bathurst 2011, Peng and Zornberg 2016). The crucial property to create a transparent soil is the refractive index, n, which is simply defined as the ratio between the speed of light passing through a vacuum and the speed of light passing through the material. If two adjacent materials have matching refractive indices, light will not reflect or refract at the interface between them rendering the combined medium transparent. The refractive index of fused quartz is well-defined, ~1.4586 at a reference wavelength of 589 nm, so the refractive index of the saturating fluid must match this value as closely as possible. More details regarding the refractive index property are included in subsequent chapters.

Petro-Canada produces two white (clear) mineral oils, Puretol 7 Special and Paraflex HT4, that have refractive indices above and below the refractive index of fused quartz, 1.4635 and 1.4532, respectively. Because these two oils are miscible, they can be used to create a mixture with a refractive index approximated by a weighted average of the refractive indices by volume. A mixture ratio of 52% Puretol 7 Special and 48% Paraflex HT4 was found to be adequate for small-scale transparent soil applications, (Peng and Zornberg 2016). Other properties of the two mineral oils are summarized in Table 4, (Petro-Canada Lubricants Inc. 2013, 2017).

Table 4. Properties of Petro-Canada mineral oils

Property	Units	Test Method	Puretol 7 Special	Paraflex HT4
Density	kg/L @ 15°C	D4052	0.842	0.825
Viscosity	cSt @ 40°C	D445	12.2	3.7
Flash Point	°C	D92	190	135
Pour Point	°C	D5950	-20	-24
Refractive Index	-	-	1.4635	1.4532

3.1.3: Opaque Soil Particles

In anticipation of using opaque soil particles for displacement tracking, black gravel particles were obtained. Colored fish tank gravel was readily available and inexpensive. The particle size and shape approximately matched the crushed fused quartz particles, although that are slightly more rounded than the angular crushed glass. A sample of opaque soil particle suspended in the transparent soil is presented in Figure 31.

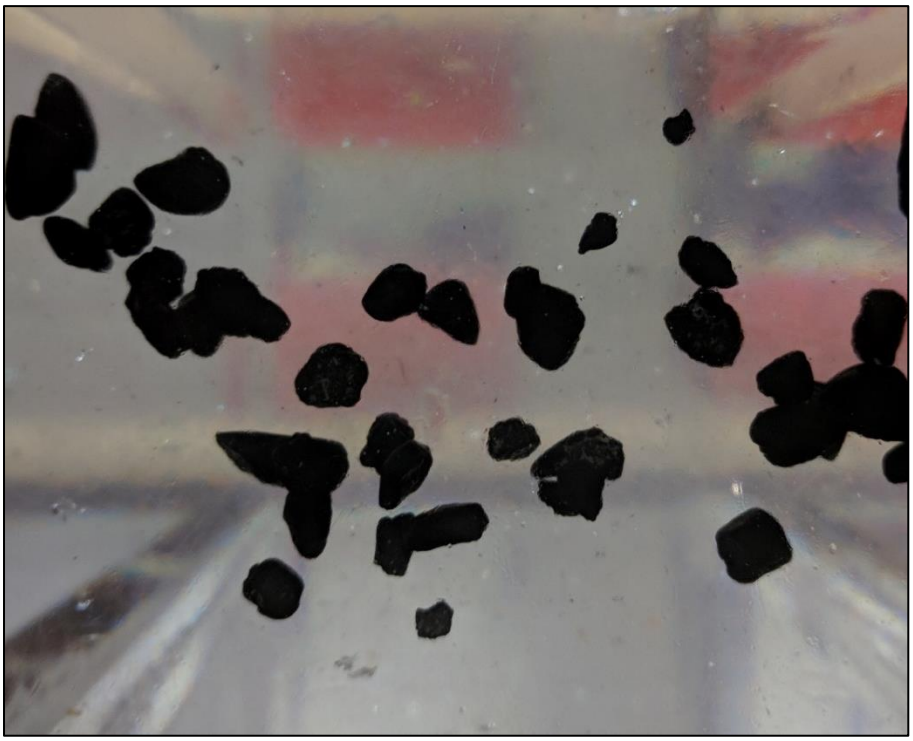

Figure 31. Opaque soil particles suspended in transparent soil

3.2: EQUIPMENT

3.2.1: Large-Scale Transparent Soil Apparatus

3.2.1.1: Purpose and Conception

The purpose of developing a large-scale transparent soil apparatus (LSTSA) was to test geocell-reinforced soil masses at the scale used in the field, while also utilizing the transparent soil techniques already employed for the characterization of geosynthetic-soil interaction mechanisms on smaller scales. As mentioned in previous sections, this study's focus is on the application of geocells for pavement design and the resistance of traffic loading. In order to visualize the mechanisms at work in a geocell-reinforced soil mass under traffic loading, a plate load test framework was adopted and based on ASTM D 1196-12 – The Standard Test Method for Nonrepetitive Static Plate Load Tests of Soils and Flexible Pavement Components. Considering the repeated nature of traffic loading, a repeated or cyclic plate load test may be more appropriate, but time and practicality constraints dictated otherwise.

The designated geocell test sections, as noted in previous sections, are based on 4x4 section a typical commercial geocell product with nominal-expanded cell dimensions 259 mm (10.2") x 224 mm (8.8") leading to overall test section dimensions 1,036 mm (40.8") x 896 mm (35.3"). The proposed transparent soil testing procedures necessitated fully-transparent side walls for the visualization of vertical soil particle movements and the bending and/or settlement of the geocell-reinforced section. In addition to transparent sidewalls, a transparent base panel was also required to enable to visualization of lateral soil particle movements and the expansion and/or contraction of individual geocells. The entire tank had to be elevated on a steel frame to facilitate the placement of a digital camera

beneath the apparatus with a sufficient focal distance to capture the entire plan area. A rigid steel reaction frame was necessary for the application of the vertical load.

3.2.1.2: Design, Fabrication, and Assembly

During the design process, AutoCAD and SolidWorks were utilized simultaneously to develop two-dimensional and three-dimensional models, respectively. In SolidWorks, material properties could be input for different sections to allow for the estimation of material quantities, weights, and costs. The AutoCAD drawings were eventually used as the final submission to the fabrication company, W2MacFab.

The design process began with a simple steel-framed, acrylic-sided tank, which would eventually become the main tank of the final design, Figure 32. The structural frame consisted of 2” x 2” x 0.25” square steel sections. The structural frame was fastened with L-shape brackets with four 0.25”-diameter bolt holes per side. The frames for the acrylic consisted of 2” x 2” x 0.25” L-shape steel sections. These frames were to be welded together and subsequently welded to the structural frame. No accommodations were made for the reaction frame nor the base frame at this stage of design.

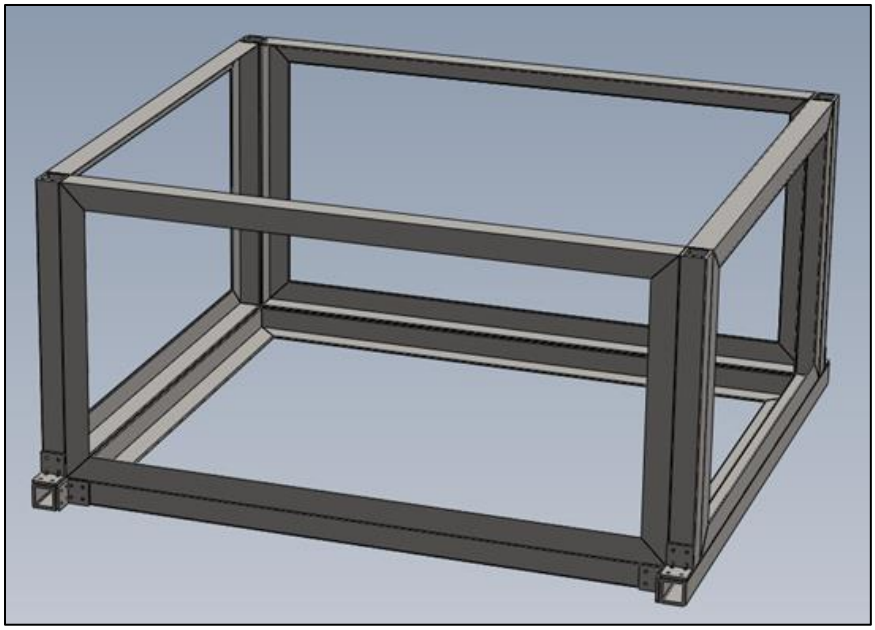

Figure 32. First iteration of the LSTSA design process

The second design iteration included the first versions of the reaction frame and base frame, as pictured in Figure 33. The reaction frame consisted of two 2” x 4” x 0.25” rectangular steel sections, which supported a W5x16 steel section as the crossbeam. These sections were chosen to limit the overall machine deflections in the reaction frame to < 1 mm (0.04”) based on a conservative point load analysis. The reduction of machine deflections was noted as an important factor in the accuracy of vertical displacement measurements. In this design iteration, the base frame elevated the main tank approximately 40” above the ground, a distance determined to be adequate based on the minimum focal distance of the digital cameras available in the laboratory. This design iteration consisted of three main structural components: 1) the scaffolding/support frame (red), 2) the main tank (blue), and 3) the reaction beam (yellow).

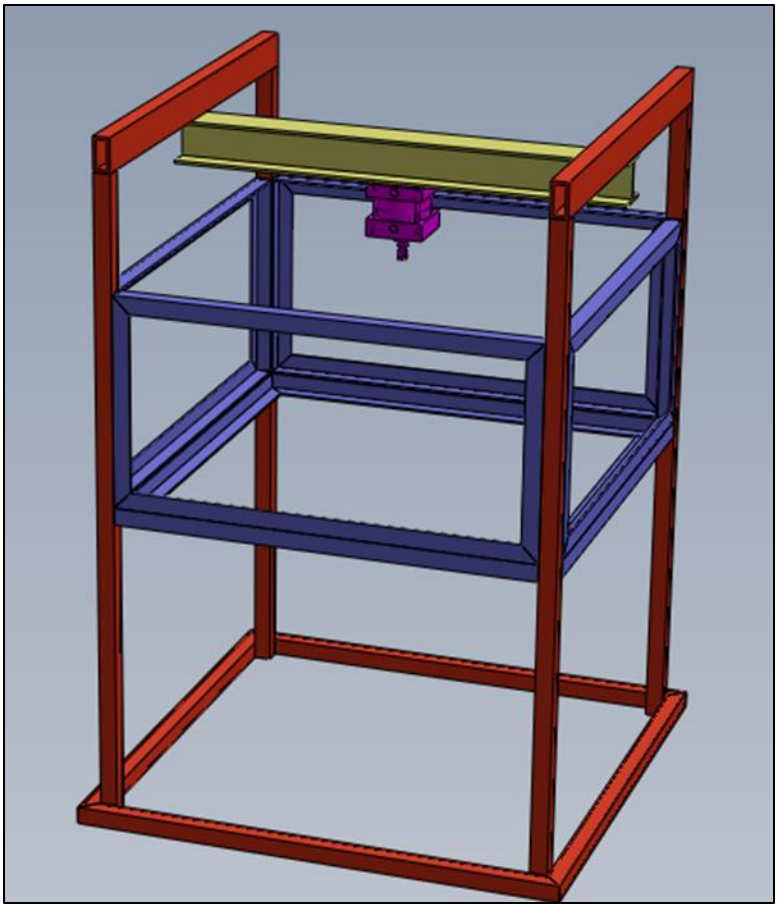

Figure 33. Second iteration of the LSTSA design process

The third design iteration, Figure 34, modified the original reaction frame design to include triangular side frames to support the W5x16 reaction beam. In addition, diagonal supports were added to the base frame to resist buckling in the legs when the main tank was fully-loaded with transparent soil, estimated at the time to be approximately 2,560 lb in total. The acrylic panels were also included in the third design iteration for weight and cost estimates. This design iteration consisted of 3 main structural components: 1) the base frame (red), 2) the main tank (blue), and 3) the reaction frame (green).

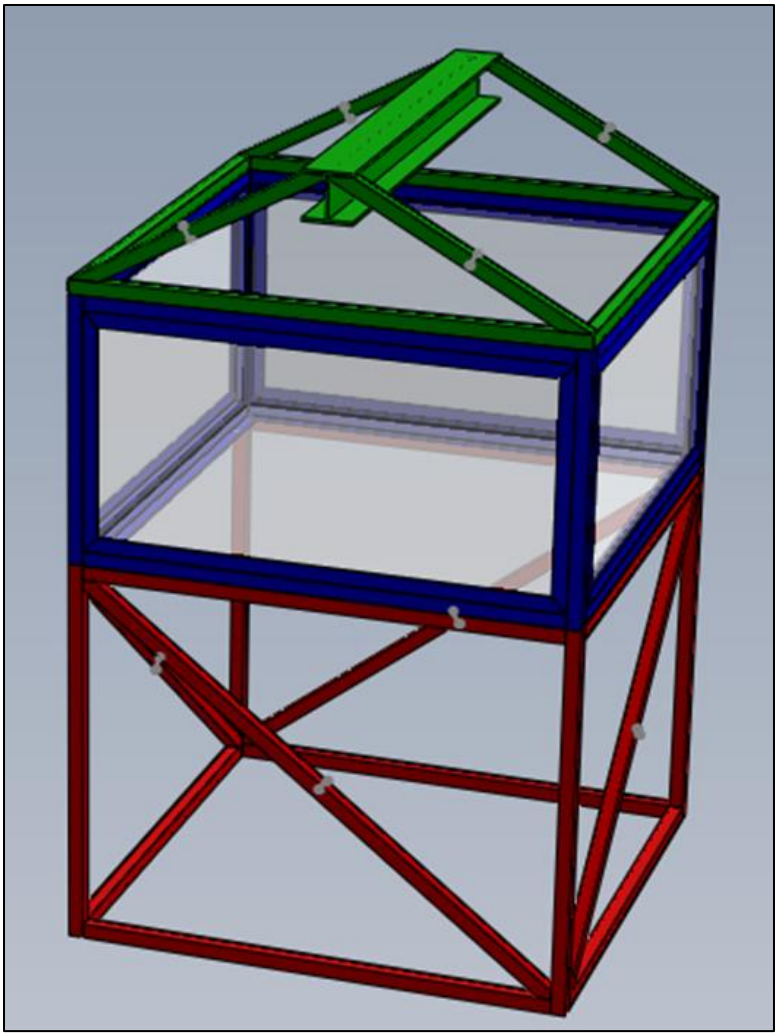

Figure 34. Third iteration of the LSTSA design process

The fourth design iteration, Figure 35, made a number of significant improvements that were incorporated into the final design. First, the height of the reaction frame was increased to accommodate the fully-designed pneumatic loading system. The original W5x16 reaction beam was replaced with a 3” x 4” x 0.5” rectangular section connected to the side frames with angle brackets. As such, a plate was also added on the reaction beam to bolt the pneumatic piston in place. The second main design modification included the decisions regarding the subdivision of structural components to facilitate the assembly of

the apparatus in a confined space. Connection details were also provided consisting of overlapping plates and bolts on the faces, slotted plates and threaded rods on the corners, and triangular gussets on the base frame. This design iteration consisted of three main sections subdivided into 15 individual steel components. The base frame consisted of two square side frames and four crossbeams. The main tank consisted of a bottom frame, four corner posts, and a top frame. The reaction frame consisted of two triangular side frames, two auxiliary crossbeams, and the main reaction beam.

One major change between the final design iteration and the fabrication of the LSTSA was the reconfiguration of the tank section into a single welded component in order to facilitate a water-tight construction and remove the over-complicated slotted plate-threaded rod connections. Other small details were altered to facilitate the fabrication procedure and simplify assembly. The fabricated and assembled LSTSA is depicted in Figure 36. Custom, large-area washers were used to secure the base panel of the LSTSA into the bottom frame in order to reduce the risk of localized stress cracking near bolt holes. The acrylic panels were all sealed in place using an oil-resistant, silicone RTV sealant.

Figure 35. Fourth and final iteration of the LSTSA design process

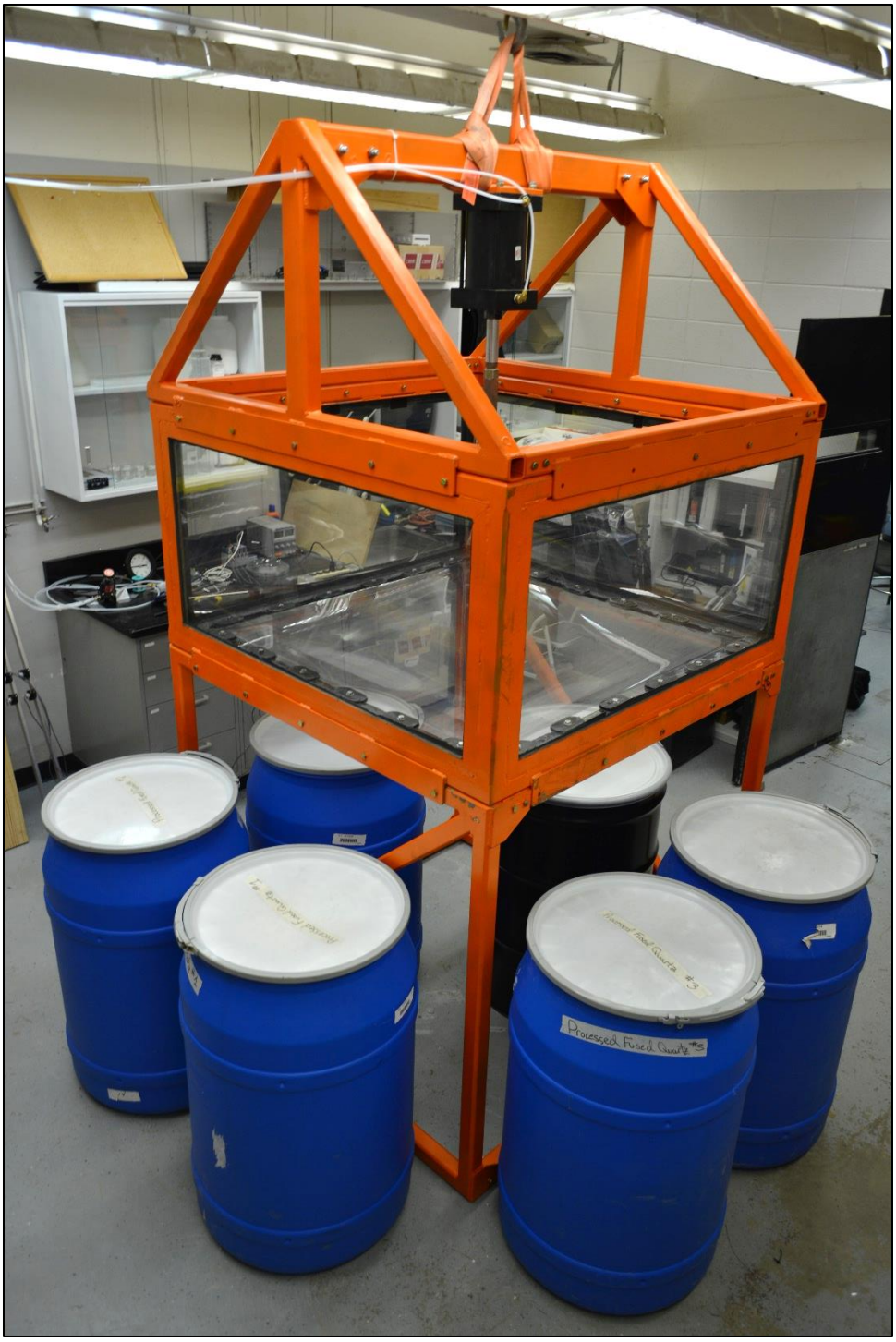

Figure 36. Assembled LSTSA with standard 55-gal drums for scale

3.2.2: Pneumatic Loading System

The purpose of the pneumatic loading system is to apply an incremental, static load to the soil surface via a circular footing. The building air pressure available is approximately 95 ± 5 psi. In order to apply a load of sufficient magnitude, a large diameter piston was required. A Dayton 4MU55 Air Piston was selected. With a 6" bore, 1.375" rod diameter, 26.8 in^2 effective area, and the available air pressure it can provide a theoretical maximum load of 2679 lbs. In addition, the Dayton 4MU55 is a double-acting piston meaning air pressure can be used to extend and retract the piston rod by switching which chamber is pressurized. This may allow for repeated load applications in future test series.

In order to operate the pneumatic piston, the building air pressure is routed through a pressure regulator, a mechanical pressure gauge, and a two-way control valve leading to the two chambers of the double-acting piston.

It should be noted that there are a number of drawbacks associated with this particular pneumatic loading system. First, there is significant friction within the piston, and overcoming that friction to apply load in a consistent sequence can be difficult, especially at lower load levels. In addition, based on experience and perhaps due in some part to the internal friction, the load application is not always linearly proportional to the applied pressure. Finally, there is significant time lag between a pressure increase and the application of load. All of these factors must be accounted for when operating the pneumatic loading system.

3.2.3: Circular Footing

Circular footings are often used for plate load tests (PLT) on pavements, so it was determined to be an appropriate shape for this application. The circular footing is constructed from two ¾"-thick plates of aluminum, one 8" in diameter and the other 6" in

diameter. The two circular plates are bolted together to provide a rigid structure with which to apply the load. The smaller top plate has a centered, chamfered hole in which sits a stainless-steel ball bearing. The load is applied to this ball bearing to ensure that all of the load is applied via vertical compression without any bending moment or eccentricity. For additional testing capabilities, the smaller plate can be removed and used itself for a smaller footing area and higher corresponding bearing pressure at the same load level. However, in this configuration, the footing should be monitored closely for signs of bending or plastic deformation which may permanently damage the footing and bias the test results. An image of the assembled footing is included below, Figure 37.

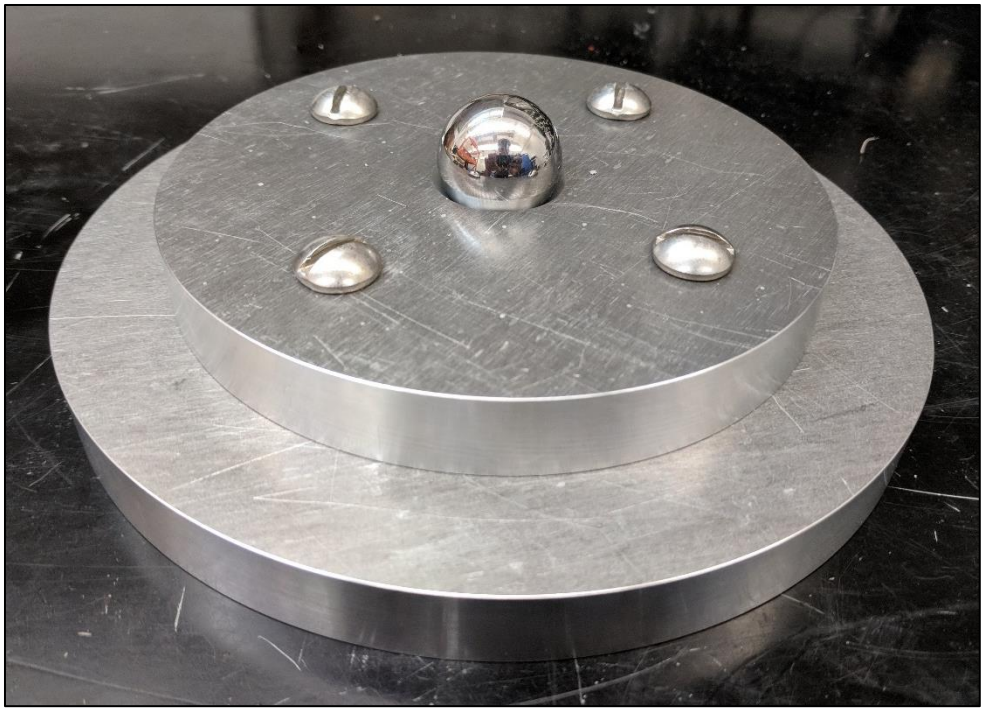

Figure 37. Circular aluminum footing with 8” bottom plate dia. & 6” top plate dia.

The footing also has four hooks in the top plate that are used to attach leads to displacement transducers (not pictured in Figure 37). The average of the displacement

readings from these four positions can be used to determine the overall vertical footing displacement during a test. In addition, differences between the relative displacement of individual positions can be used to determine if, and in what direction, the footing is tilting during load application, an important consideration during testing. In certain situations, it was necessary to add a spacer between the two plates in order to accommodate the limited stroke of the piston and extend the vertical range of the loading system.

3.2.4: Load Cell

A 5000-lb load cell from Geotac, Figure 38, was selected in order to ensure the maximum applied load would not exceed the capacity of the load cell. The load cell has a threaded hole in both ends with standard ¾”-16 threads. Because the piston rod has 1”-14 threads, an adapter was made from 1.5” diameter hexagonal stock steel. A 1”-14 nut, 3”-long, ¾”-16 threaded rod, and ¾”-16 nut were used to complete the loading system assembly. The fully-assembled loading system consisting of the pneumatic piston, hex adapter, load cell, and footing is depicted in Figure 39.

Figure 38. Geotac 5k S-beam load cell

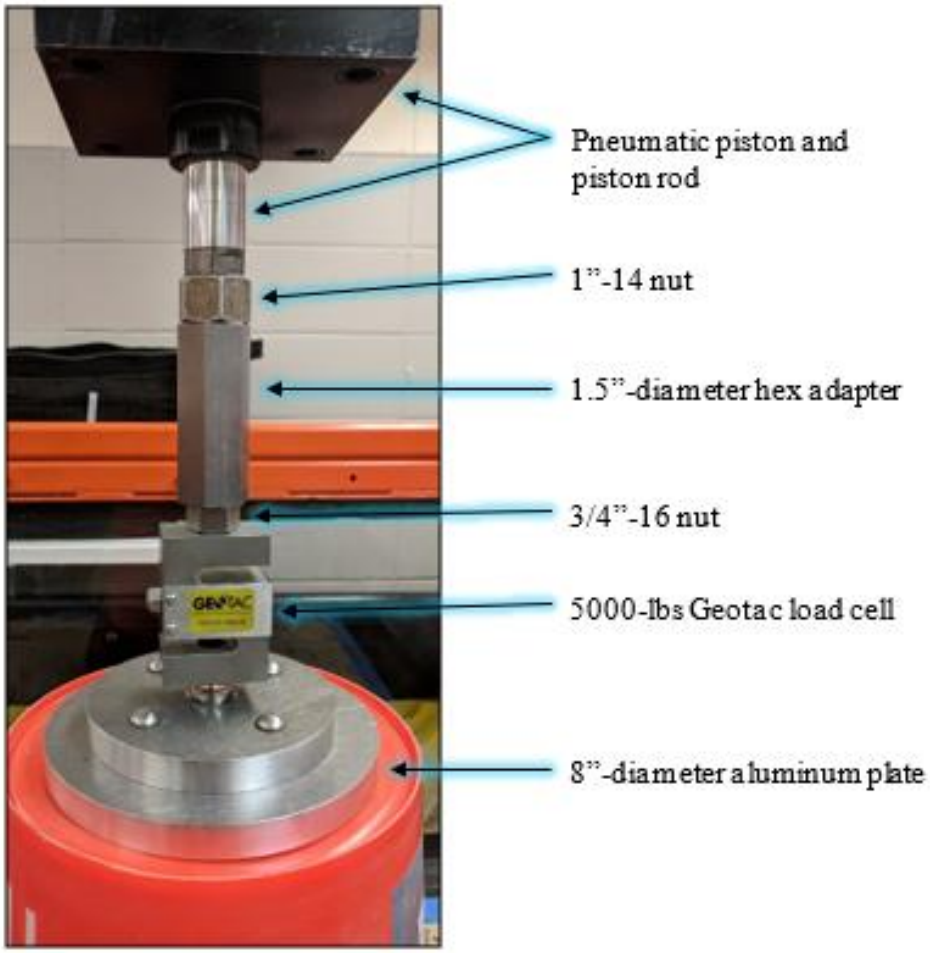

Figure 39. Fully-assembled loading system

3.2.5: Displacement Sensors

In order to 1) validate the results of DIC procedures, 2) have a real-time indication of footing displacement during testing, and 3) directly compare results to previous geocell experiments, it was determined that physical displacement measurements were also required. Based on previous experience, UniMeasure LX-PA linear position transducers were selected for this purpose. These sensors are low cost, compact, and suitable for light- to moderate-duty applications. When supplied with a 10 VDC excitation voltage, the

ratiometric sensors output an analog signal corresponding to the extension of the draw wire. Two different models were used, the LX-PA-2.8 and LX-PA-2, with ranges of 2.8” and 2.0”, respectively.

These sensors were used to measure vertical footing displacement as well as heave and/or settlement of the soil surface adjacent to the footing. Sensor mounting beams fabricated from lengths of ½”-square aluminum were used to secure the sensors in position above the footing and soil surface, Figure 40 and Figure 41. In order to compensate for the nominal tension in the draw wires, steel hanging weights were made to rest on the soil surface with minimal influence on the heave/settlement response during loading, Figure 42. Metal wires were used to attach the draw wires to hooks on the footing and soil surface weights, Figure 43.

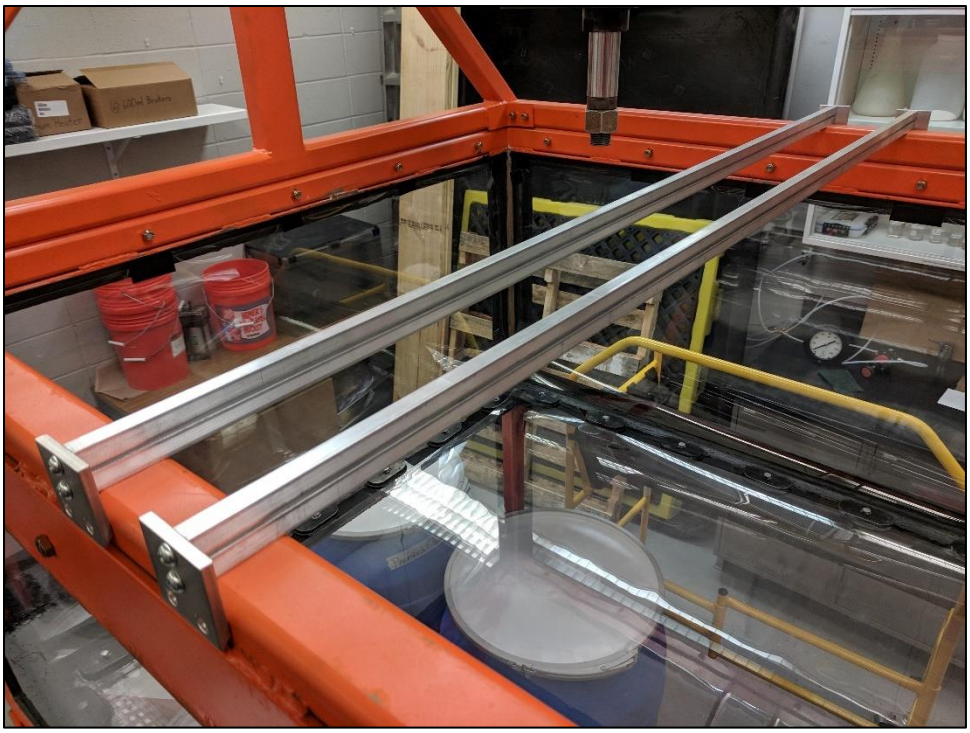

Figure 40. Sensor mounting beams in place across the top of the LSTSA tank

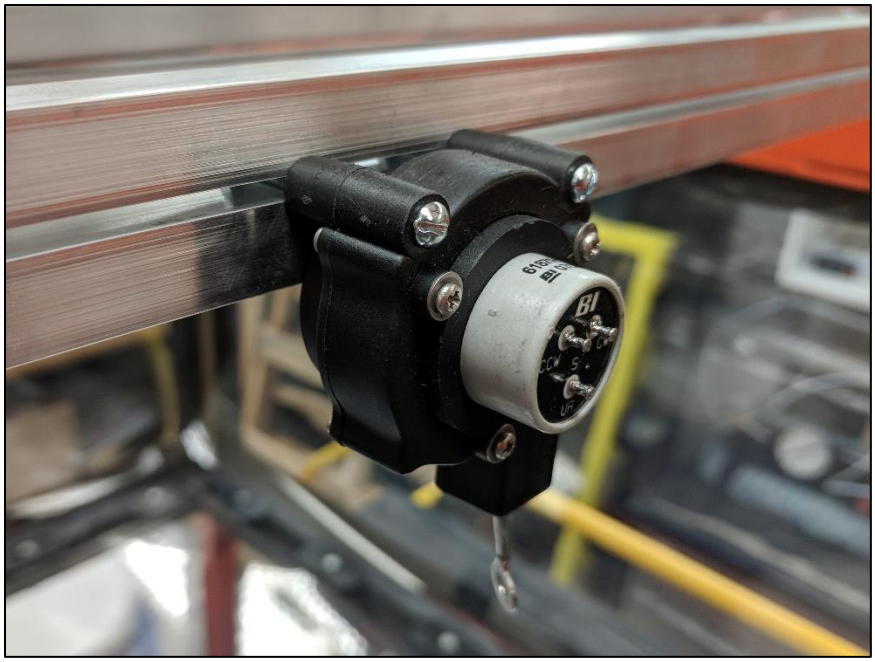

Figure 41. UniMeasure LX-PA displacement sensor secured to mounting beam

Figure 42. Steel hanging weight with hook to compensate for nominal draw wire tension

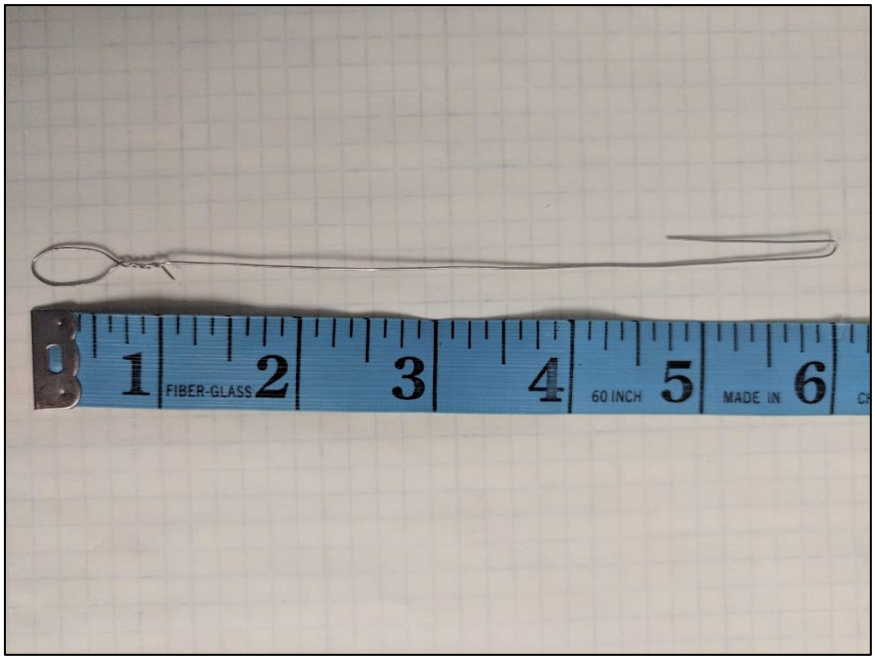

Figure 43. Metal wire used to attach LX-PA draw wires to hanging weights

3.2.6: Data Acquisition System

A National Instruments Compact Data Acquisition System (cDAQ) was configured to measure and record the signals from the load cell and displacement sensors. The DAQ consisted of a cDAQ-9174 chassis with four module slots, a 16-channel NI 9206 analog input module for the displacement sensors, and a 4-channel NI 9237 full-bridge module for the load cell, leaving two slots open for additional modules. A Mastech HY30055D DC power supply was used to provide a constant 10-VDC excitation voltage to all sensors. More details regarding the sensors, DAQ, and wiring configurations can be found in Appendix A.

3.2.7: Camera and Laser System

In anticipation of unique opportunities to observe and quantify soil-reinforcement interactions within the transparent soil, a DSLR camera and planar laser system was

developed based on the system developed by Dr. Xin Peng, (Peng and Zornberg 2016). The system consists of a Nikon D5200 DSLR camera and a World Star Tech Compact Laser Controller. The laser produces a sheet of laser light with maximum output power of 375 mW at a wavelength of 638 nm (red light). The planar laser illuminates a single plane of fused quartz particles within the transparent soil mass as depicted below in Figure 44. The DIC analysis procedure works best with a consistent texture as individual pixel clusters are identified in sequential images to develop a full-field displacement contour map. In this respect, the high contrast between the illuminated particle boundaries and darkened interiors is ideal for DIC analysis.

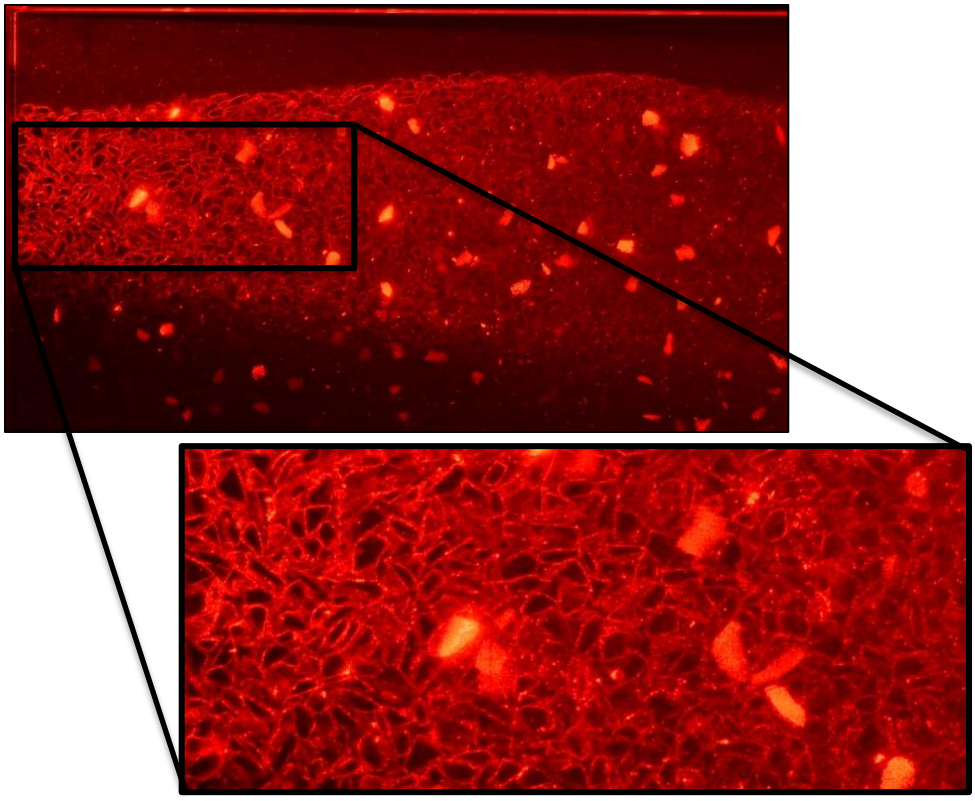

Figure 44. Laser-illuminated plane of fused quartz particles in a transparent soil mass

3.2.8: Oil Circulation and Recycling System

For reasons that will be detailed in a later chapter, it was determined that an oil circulation system would aid the set up and modification of transparent soil within the LSTSA. The required capabilities of the oil circulation system include 1) the filtering of oil to remove floating contaminants, 2) the injection of oil into the transparent soil mass without the introduction of significant entrapped air, and 3) a flow rate sufficient to complete these tasks in a reasonable amount of time. To begin, a pump was required that was self-priming, had a sufficient flow rate, required little maintenance, and did not introduce the oil to air or excessive turbulence. A high-flow peristaltic pump from the Randolph-Austin Company met these requirements with self-priming capabilities, a 3.7 GPM flow rate, and one wearing part, the length of tubing acted on by the rollers.

The peristaltic pump was attached to two manifolds, one upstream and one downstream, each with two ½" NPT inlet ports and four ⅜" NPT outlet ports. The pump was attached to one of the inlet ports of each manifold with the other leading through an on/off control valve to an external reservoir of oil. The four outlet ports on each manifold were connected to two closed loops of tubing, also via individual on/off control valves, for a total of four closed loops. The manifold upstream from the pump lead to the two suction loops that run down the corners and along two parallel edges of the base of the LSTSA. The manifold downstream from the pump lead the two injection loops suspended above the soil surface of the LSTSA tank by a frame of metal conduit tubing on the two sides perpendicular to the injection loops. An oil filter was also included to remove any contaminants suspending in the fluid. This entire system was developed to encourage a generalized, non-preferential flow pattern through the transparent soil mass for uniform oil filtration and oil ratio modification. The pump and manifold assembly, sans external tubing to the reservoir and injection and suction loops, is presented in Figure 45.

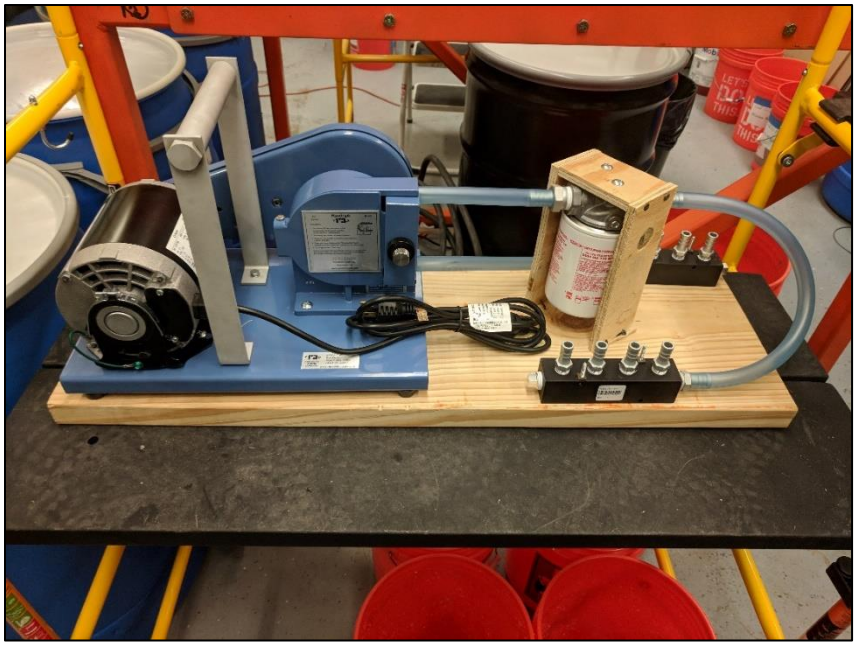

Figure 45. Pump, filter, and manifold assembly as part of the oil circulation system

3.2.9: Placement and Compaction Equipment

Controlled placement and compaction of the fused quartz in the LSTSA is crucial for consistent test set up and unbiased results. For an individual lift, the material is pre-weighed to ensure the correct amount is prepared to reach the desired density. The material is placed in the LSTSA tank with scoops or poured from buckets and then leveled with a flat-bladed, metal scraper. Height indicators on the corners of all four sides are then consulted to determine the amount of compaction required to reach the design height for the lift. An 8”-square hand tamper is used to compact the material to a consistent height. In some areas where the long-handled tamper cannot fit, such as under the pneumatic piston, a flat metal plate and handheld weight are used to ensure even compactive effort is applied to the entire surface. When removing material from the LSTSA tank, some oil may

still remain at the bottom. In order to remove the solid particles without an excessive amount of oil, large slotted scoops are used to lift and drain the fused quartz.

3.2.10: Refractometers

Refractometers are a common tool used to determine the refractive index of various liquids. They vary from large tabletop configurations to small handheld devices. These devices normally direct a standard yellow light (λ = 589.3 nm) through a small sample of fluid, and a detector registers the amount of light that returns. Some refractometers also measure the temperature of the fluid and other relevant parameters.

3.2.10.1: Atago PAL-RI

The Atago PAL-RI was the first refractometer available for this study, obtained for previous transparent soil experimentation, (Peng and Zornberg 2016). It can measure refractive indices in the range of 1.3306 to 1.5284 (precision: ± 0.0003), sufficient to measure the refractive indices of the mineral oil mixtures. The PAL-RI also measures the temperature of the sample in the range of 5 to 40°C (± 0.1°C). It is ergonomic, lightweight, and highly water resistant for easy cleaning. However, based on experience, the device often outputs inconsistent readings of identical samples and is difficult to calibrate accurately, so a second refractometer was obtained.

3.2.10.2: MISCO Palm Abbe

The MISCO Palm Abbe (PA202) is a dual-scale digital refractometer that measures the refractive index (1.3330 – 1.5000 ± 0.0001) and Brix, a measure of sugar concentration not relevant to this study. The Palm Abbe has a sapphire lens, compared to the glass lens of the Atago PAL-RI, and a very high detector resolution (3256 ppi). This refractometer also has a lens cover that removes the possibility of bias from external light sources. The

Palm Abbe also autocorrects the refractive index for temperature; the temperature itself can be obtained as well.

Chapter 4: Transparent Soil Modification and Adjustment

4.1: Small-Scale Testing

Small-scale testing of the fused quartz-based transparent soil was initially conducted to gain an understanding of its properties and workability. A small glass tank (dimensions 20” L x 10” W x 12.5” T) was filled with fused quartz saturated with an oil mixture at a ratio of 52% Puretol 7 Special and 48% Paraflex HT4, Figure 46. At this scale, the transparency of the material was determined to be marginally adequate at 10” for the goals of this study, although there were significant quality issues at 20” associated with the scale increase relative to other small-scale experimentation. It has been noted by some researchers that the maximum depth for adequate visibility in the fused quartz-based transparent soil is just 4”, (Ezzein and Bathurst 2014). If the maximum depth of the LSTSA is reached, the maximum depth of transparent soil will be 24” to the plane of interest and 48” total.

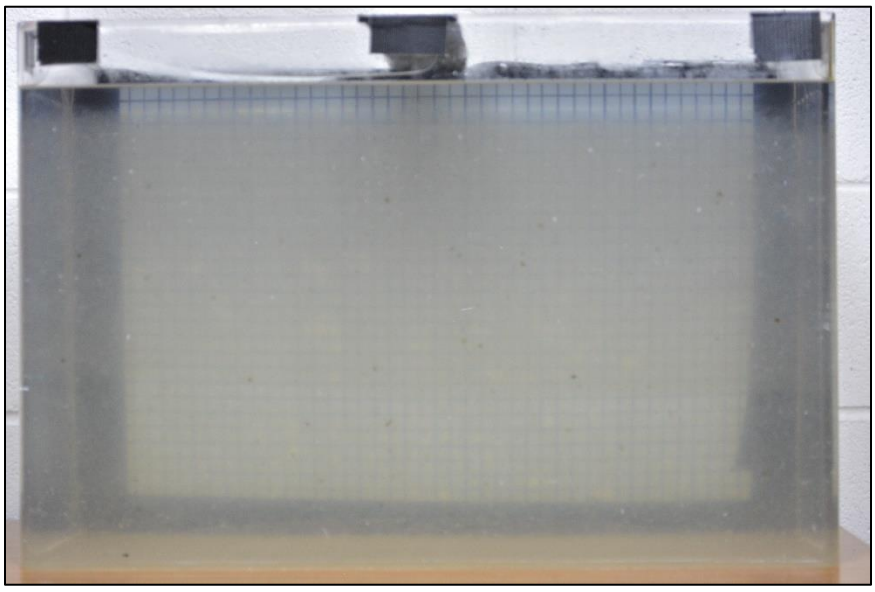

Figure 46. Small-scale transparency evaluation; grid at 10" depth is clearly visible

4.1.1: DIC Proof-of-Concept

The small-scale tank was used to conduct a DIC proof-of-concept test prior to the construction of the LSTSA. The tank was placed on a wheeled table and aligned with displacement indicators. The camera and laser were set up to illuminate a vertically-oriented plane of fused quartz particles within the transparent soil mass, approximately 4" deep horizontally from the viewing plane, Figure 47.

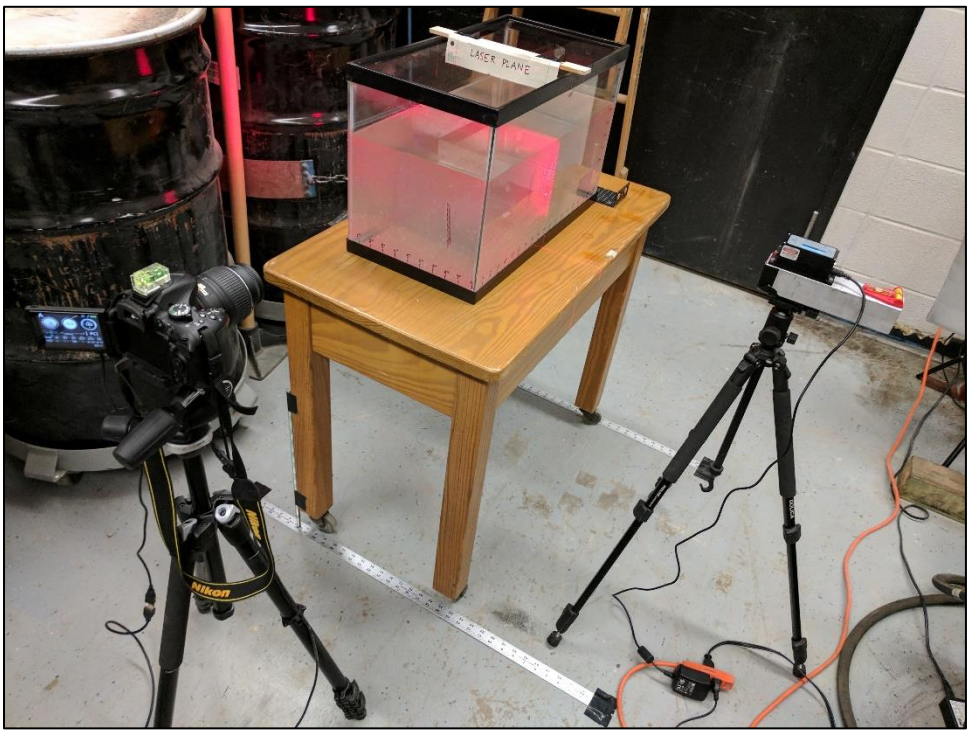

Figure 47. Setup for the DIC proof-of-concept test

The rolling table was moved perpendicularly relative to the viewing plane at ~½" increments, and a picture was taken from a stationary position after each movement. A MATLAB-based DIC code was used to track the displacement of 9 locations within the illuminated plane. The results, summarized in Figure 48, show that all 9 positions within the target area were tracked accurately.

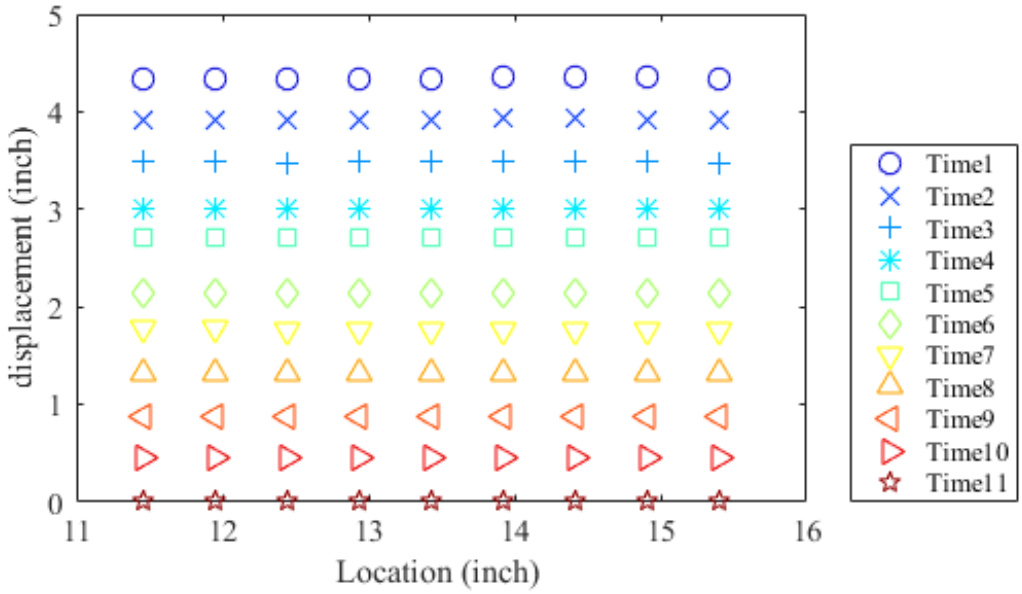

Figure 48. Results of DIC proof-of-concept test

4.1.2: Initial Limitations of Laser Plane Illumination

Additional testing with the small-scale setup revealed that there are limitations with the illumination of transparent soil with a laser plane. First, it should be noted that the mere fact that individual particle boundaries are illuminated by the laser light indicates that there is a slight mismatch in the refractive indices of the solid and liquid components of the transparent soil. If that were not the case, there would be no reflections/refractions occurring to redirect the light from the laser plane to the viewing plane. On very small scales, such as those used for geogrid pullout testing, the minor refractions within the soil do not significant affect the transparency of the material. However, when those minor refractions are summed up over greater and greater depths, a number of adverse effects can be observed.

First, light refracted off particle boundaries on a well-defined laser plane has to pass through more material to reach the viewing plane. With an increase in depth of material that the refracted light has to pass through to reach the viewing plane, the particle boundaries and texture for DIC analysis will become less distinct. Second, the laser plane itself does not remain as a narrow, well-defined plane after passing through a significant depth of material. Instead, light refracting off of individual particle boundaries disperses to a wider area further from the laser's point of entry into the material.

4.1.3: Oil Ratio Modification

Because of some of the initial issues with the transparent soil, another small-scale test was performed to determine the effect of the oil ratio on the transparency. In theory, a greater mismatch between the refractive indices of the solid and liquid components of the transparent soil would yield more refraction and less overall transparency. Because the ideal mixture was initially determined experimentally with a batch of fused quartz from a different source, it was hypothesized that the 52:48 mixture ratio was not ideal for the Heraeus HOQ 310 fused quartz. So, eight samples of transparent soil were made in identical glass beakers and placed in front of a black background. The samples had a range of oil ratios from 70:30 to 40:60 (Puretol 7 Special: Paraflex HT4) with corresponding theoretical refractive indices of 1.4603 to 1.4575, respectively. A qualitative comparison was performed, and the compiled images are presented in Figure 49.

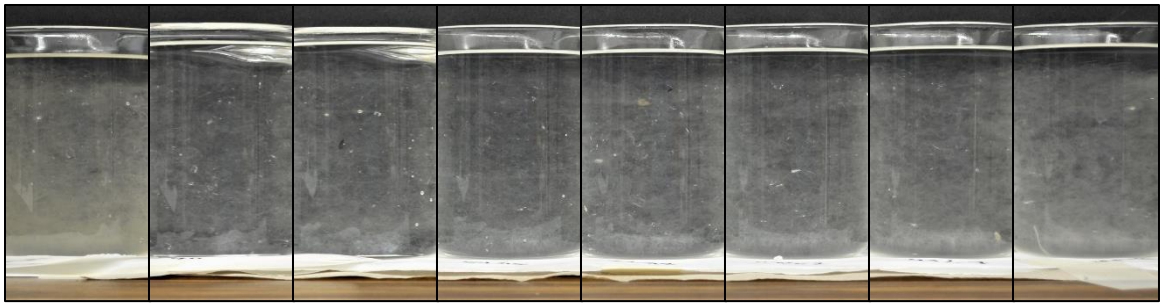

Figure 49. Qualitative comparison of oil ratios from 70:30 to 40:60 (Puretol 7 Special: Paraflex HT4)

It is clear that the extreme oil ratios performed the worst but distinguishing between the mid-range of ratios proved to be difficult. Tentatively, the 54:46 ratio was identified as the "most transparent", but the standard 52:48 ratio was nearly indistinguishable. Also, upon close inspection, particle boundaries are visible in all samples indicating that none of the oil ratios perfectly matches the refractive index of the fused quartz. However, targeting more precise oil mixture ratios and the corresponding refractive indices is impractical at large scales for a number of reasons to be explored in later sections.

4.2: Issues With Transparent Soil

4.2.1: Minor Issues

The initial large-scale testing of the transparent soil led to the identification of a number of minor issues. These minor issues alone would not result in an inadequate overall quality, but they would contribute to poor overall quality if left unaddressed. Luckily, simple solutions were easy to find for these minor issues.

The first minor issue was the presence of macro-contaminants, defined in this context as substantial particles individually visible to the naked eye. Some of these macro-contaminants were identified as colored glass, clear glass, stained fused quartz particles, other opaque particles, rubber shreds, plastic shreds, and silicone sealant fragments. Most

of these macro-contaminants, such as the glass and rubber shreds, were likely introduced into the fused quartz supply during the crushing process, but others were likely introduced during the additional processing and initial testing. Manual removal, although very time-consuming, was the best method to remove these macro-contaminants from the entire supply of crushed fused quartz.

Another minor issue observed during the initial large-scale testing was the presence of bubbles trapped between the acrylic side walls or base and the protective Mylar sheeting. These large bubbles would significantly obstruct or distort any images if they were left unaddressed. It was found that a neoprene rubber squeegee was sufficient to eliminate most trapped bubbles. Additional flushing with oil also helped in this effort.

One final minor issue found during initial testing was the fact that sweat contamination significantly affects the quality of the transparent soil. This is because water-based sweat 1) has a significantly different refractive index than fused quartz, and 2) it does not readily mix with the oil. The result of sweat contamination during the setup procedure is a surprisingly large area where sweat displaces the oil and creates a completely non-transparent medium. Minimizing the time spent leaning over the soil mass and wearing sweat bands during setup proved to be sufficient to avoid significant sweat contamination.

4.2.2: Major Issues

In addition to the aforementioned minor issues, a number of major issues with the transparent soil were identified during the small- and large-scale testing. These major issues included the presence of micro-contaminants, mismatching refractive indices, and the question of light transmittance. As these issues all have the potential to completely ruin the quality of the transparent soil, it was vital to find solutions to each one.

4.2.2.1: Micro-contaminants

In addition to the macro-contaminants from the processing and handling of the fused quartz, there are also micro-contaminants present in the transparent soil. These individual micro-contaminants cannot be seen with the naked eye, but their detrimental effect on the quality of the transparent soil is apparent. These particles of unknown origin are present on the surface of fused quartz particles. When the fused quartz is saturated with oil and agitated, some of the micro-contaminants are dislodged from the fused quartz and become suspended in the oil. It is the job of the oil filter to then remove these floating micro-contaminants from the fluid. Both the clouding effect of suspended micro-contaminants and the effectiveness of the filter at removing them was demonstrated using the small-scale glass tank setup filled with oil alone. Figure 50 depicts the end-on view of the test tank (a 20" depth) filled with just oil before and after filtration.

Figure 50. Comparison of oil clarity before and after oil filtration of micro-contaminants

This test was performed after fused quartz was added to the oil, agitated, and then removed. This effort was an attempt to dislodge all micro-contaminants from the fused quartz. However, when the same fused quartz was replaced in the same oil, re-agitated, and removed again, the oil was nearly as cloudy as the initial test. This indicates that significant

effort must be employed to completely rid the fused quartz of micro-contaminants. It is unclear if constant oil circulation and periodic agitation of a full transparent soil mass will allow for micro-contaminants to dislodge from the fused quartz and flow through the soil mass to the oil filter. Further testing should be conducted in this vein.

4.2.2.2: Mismatching Refractive Indices

As mentioned in previous sections, a mismatch between the refractive indices of the solid and liquid components of a transparent soil will have a significant detrimental effect on the clarity of that material. Most of the transparent soil literature cite refractive indices of the materials in use to the third or fourth decimal place, often the maximum precision of the refractometer used to measure it. However, it is not clear what constitutes a *significant mismatch*, especially in the context of large-scale transparent soil tests. Perhaps with a refractive index "match" to the closest 0.0001 is not sufficient to limit the minor refractions to a point that yields adequate transparency for large-scale experimentation. If more precision is required, it will be extremely difficult to reach and maintain that match for reasons explored in the following sections.

4.2.3: Refractive Index Theories and Complexities

4.2.3.1: Dispersion Curves and Wavelength Dependence

In many studies that deal with transparent soil for geotechnical applications, the refractive index, n, is often defined simply as the ratio between speed of light in a vacuum and the speed of light in the material. A more rigorous definition is the ratio between the phase velocity of light in a vacuum, $c \approx 3x10^8$ m/s, and the phase velocity of light in the material, v, which is equal to the product of the wavelength, λ_0, and the temporal frequency, ν_0.

$$n = \frac{c}{v} = \frac{c}{\lambda_0 \nu_0} \qquad (30)$$

This form of the refractive index equation clearly demonstrates the dependence of refractive index on the wavelength of light passing through the material, a nuance often lost in applications outside of technical optics. This wavelength dependence is known as dispersion. For normally-dispersive materials, n decreases with increasing wavelength, and the effect can often be significant with the refractive index of fused quartz varying from 1.4701 at 400 nm to 1.4542 at 750 nm. Dispersion is even more complicated in narrow bands of wavelength corresponding to the electron resonances in the material. For this application, the dispersion around resonance can largely be ignored because the electron resonant frequencies for fused quartz correspond to wavelengths outside of the visible spectrum, Figure 51.

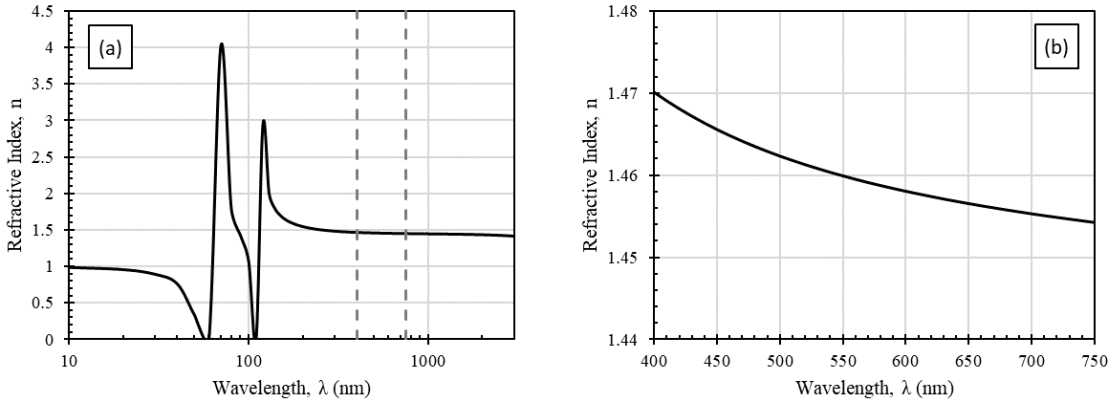

Figure 51. Dispersion curves of fused quartz for (a) a wide range of wavelengths and (b) the visible spectrum

Note, in previous sections of this thesis, the refractive index is often referred to as a standalone value for a particular material. The refractive indices often documented for

materials in non-optical applications correspond to a common reference wavelength of the sodium D line, λ = 589.3 nm. This reference refractive index for fused quartz is around 1.4586 ± 0.0002 depending on the exact formulation.

The full dispersion curve of a material is often described by the empirical Sellmeier equation of the form below with the B_i coefficients representing the strength of the absorption resonance at wavelengths $\sqrt{C_i}$, (Sellmeier 1871),:

$$n^2(\lambda) = 1 + \frac{B_1\lambda^2}{\lambda^2 - C_1} + \frac{B_2\lambda^2}{\lambda^2 - C_2} + \frac{B_3\lambda^2}{\lambda^2 - C_3} \qquad (31)$$

The constants in the Sellmeier equation are determined by the method of least squares on a data set of refractive indices at standard wavelengths performed on several melt samples, (Ohara Corporation 2018). Over ranges of wavelength not subject to electron resonance considerations, the Cauchy equation can also be used to describe the dispersion of typical materials; one form of the Cauchy equation is below, (Jenkins and White 1981):

$$n(\lambda) = B + \frac{C}{\lambda^2} + \frac{D}{\lambda^2} + \cdots \qquad (32)$$

Often, a two-term form of the Cauchy equation is sufficient to describe the dispersion over the range of visible wavelengths. However, there is a clear discrepancy between the Cauchy and Sellmeier dispersion curves for fused quartz in the visible spectrum, as depicted below in Figure 52. The coefficients used for the two curves are listed in Table 5, (Malitson 1965). The Sellmeier curve will be used for all subsequent analyses as it is more technically rigorous and precise.

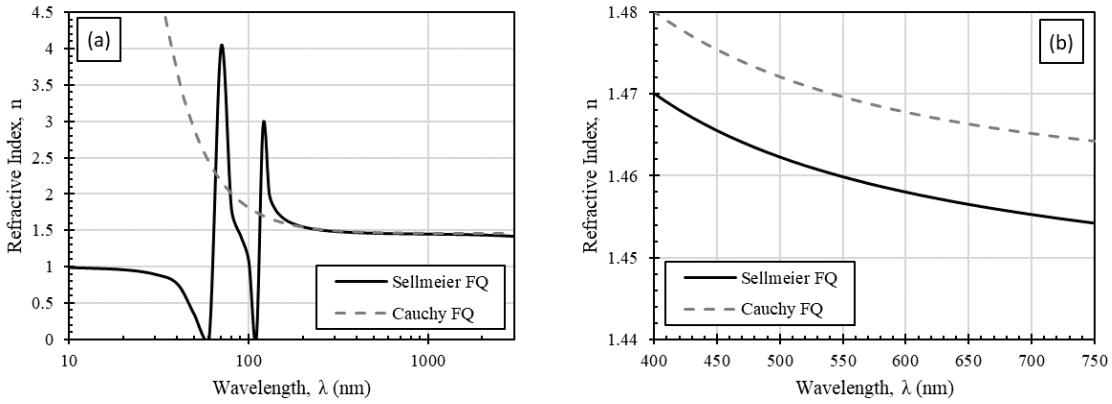

Figure 52. Comparison of Sellmeier and Cauchy dispersion curves of fused quartz

Table 5. Constants for Sellmeier (@ 20°C) and Cauchy dispersion curves of fused quartz

Sellmeier Constants		Cauchy Constants	
B_1	0.6961663	B	1.458
B_2	0.4079426	C	0.00354
B_3	0.8974794		
C_1	0.004679148		
C_2	0.013512063		
C_3	97.9340025		

The dispersion curve of any material may have a slope greater, equal to, or less than the slope of fused quartz. If the dispersion curves for the two mineral oils are the same as fused quartz over the visible spectrum, then a mixture at the correct ratio should align perfectly with fused quartz over a large range of wavelengths and the wavelength dependence of refractive index can be ignored. However, if the dispersion curve slope for one or both oils does not match the slope of the dispersion curve of fused quartz, any mixture of the two oils will only adequately match the refractive index of fused quartz over a small range around a particular wavelength where the curves intersect. As such,

determining the dispersion characteristics of the minerals oils is a crucial step in establishing the best possible transparent soil quality.

4.2.3.2: Temperature Dependence

The refractive index of a material is also dependent on its temperature. This relationship is defined by the temperature coefficient of refractive index, dn/dT. This coefficient itself changes with wavelength and temperature. According to the Ohara Corporation, "temperature coefficients of refractive index show the changes of refractive indices of the material when the temperature of the material raises by 1°C. Usually the coefficient is achieved by averaging the change of the refractive indices of 20°C temperature range," (Ohara Corporation 2018). The relative temperature coefficients (relative to the temperature coefficient of air) of Heraeus HOQ fused quartz are presented in Figure 53.

Relative temperature coefficients of the refractive index in 10^{-6} K^{-1}

Wave-length	Suprasil®-family, Spectrosil®		Infrasil® / HOQ®	
nm	0...20°C	20...40°C	0...20°C	20...40°C
237,8	14,6	14,9	15,2	15,3
365	11	11,2	11,5	11,6
546,1	9,9	10,1	10,6	10,7
587,6	9,8	10,0	10,5	10,6
643,8	9,6	9,8	10,4	10,5

Figure 53. Relative temperature coefficients of Heraeus HOQ fused quartz, (Heraeus 2016)

In absence of published temperature dependence properties for the mineral oils used in this study, a simple experiment was conducted using the Atago PAL-RI refractometer (the Atago refractometer was selected instead of the MISCO because it does not automatically compensate for the temperature of the sample). To begin, samples of both pure mineral oils were heated on a hot plate. The refractive index was tested repeatedly as the samples cooled. Subsequently, the samples were cooled further in a refrigerator and tested as they warmed to room temperature. The data from this experiment are presented in Figure 54a and Figure 54b. The circular markers indicate experimental data, and the black X's represent values obtained from the empirical equation below, after Aguilar-Arevalo (2008). A linear fit was produced to determine a single dn/dT value for the range of temperatures tested.

$$n = A \cdot [1 + B(T - 20)] \qquad (33)$$

where:

n	=	refractive index of the material
A	=	refractive index at T = 20°C
B	=	coefficient related to dn/dT
T	=	temperature, °C

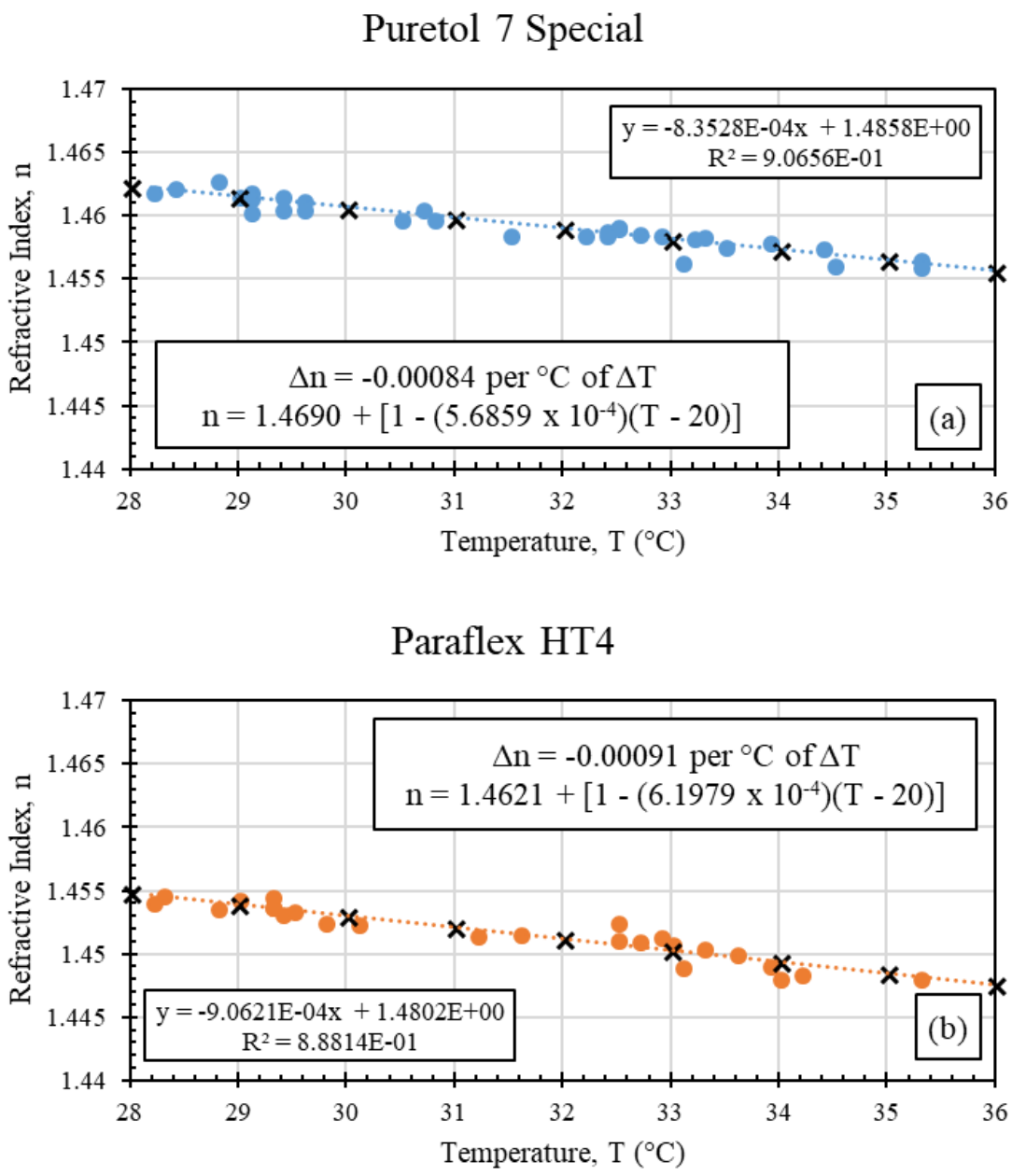

Figure 54. Experimental temperature dependence of (a) Puretol 7 Special and (b) Paraflex HT4

In order to understand the impact of this temperature dependence on the refractive index of the oil used in the laboratory, an ExTech SD700 Climate Datalogger was used to

track daily temperature fluctuations at 3-minute intervals. The maximum, minimum, mean, and standard deviation of the daily temperature in the laboratory are presented in Figure 55a. Based on that data and the empirical temperature dependence, above, the expected fluctuations in refractive index of both pure mineral oils and the 52:48 mixture are presented in Figure 55b. Clearly, there are non-negligible refractive index fluctuations as a function of the laboratory temperature. It should be noted that this conservatively assumes the oil temperature fluctuates with the air temperature; it is expected that the oil temperature fluctuations will be some fraction of the air temperature fluctuations.

To get a better understanding of the effect of hourly fluctuations, the temperature logs from three days with abnormally high fluctuations, typical fluctuations, and low fluctuations are presented in Figure 56a. The corresponding refractive index fluctuations relative to the average n-value are presented in Figure 56b. For a typical day, the hourly temperature fluctuations will not change the refractive index of the oil by more than ±0.0003, a small but non-negligible amount, with the conservative assumption that oil temperature fluctuations match air temperature fluctuations.

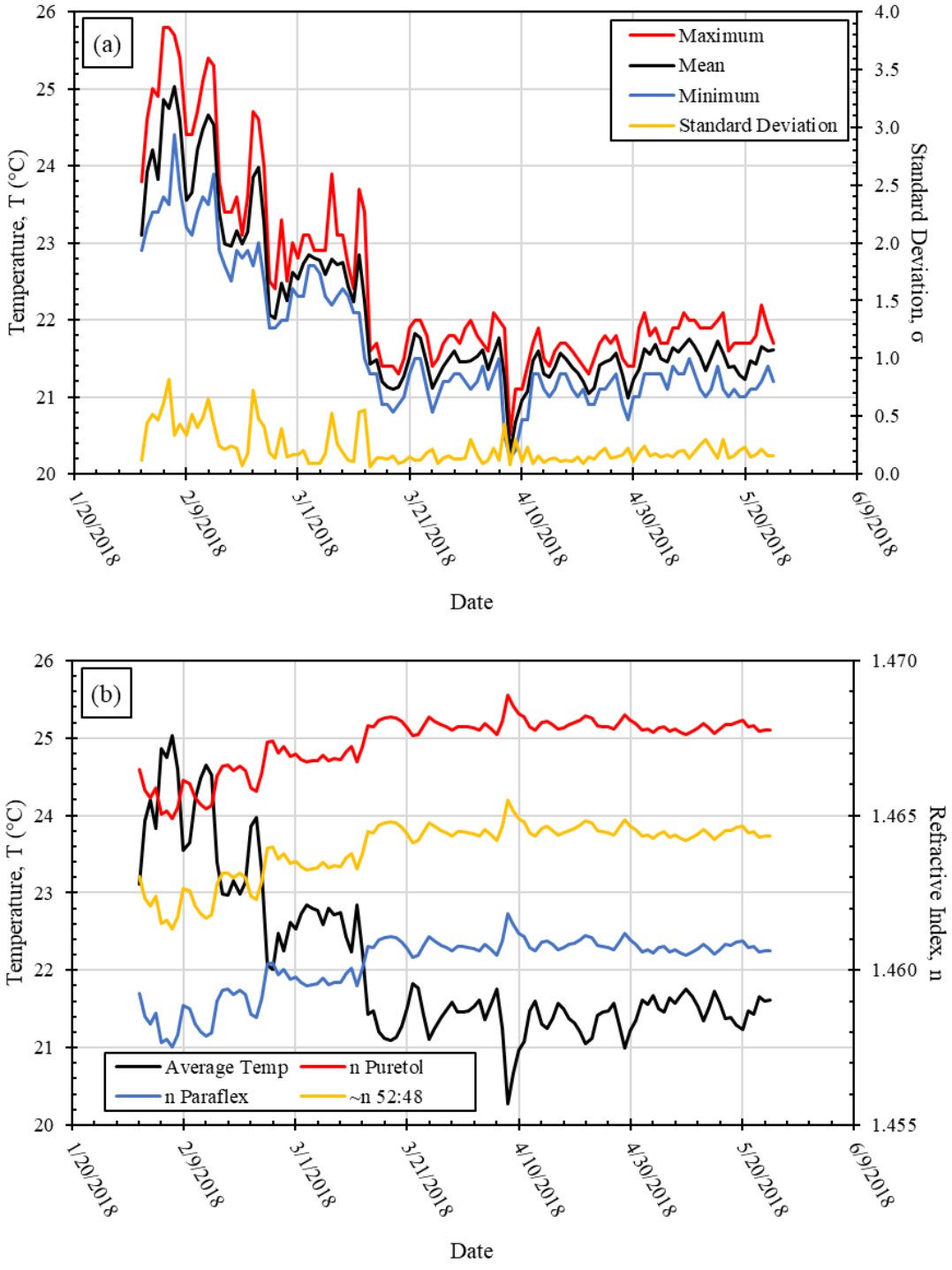

Figure 55. (a) Daily temperature fluctuations in the laboratory and (b) the effect on the refractive index of the mineral oils and mixture

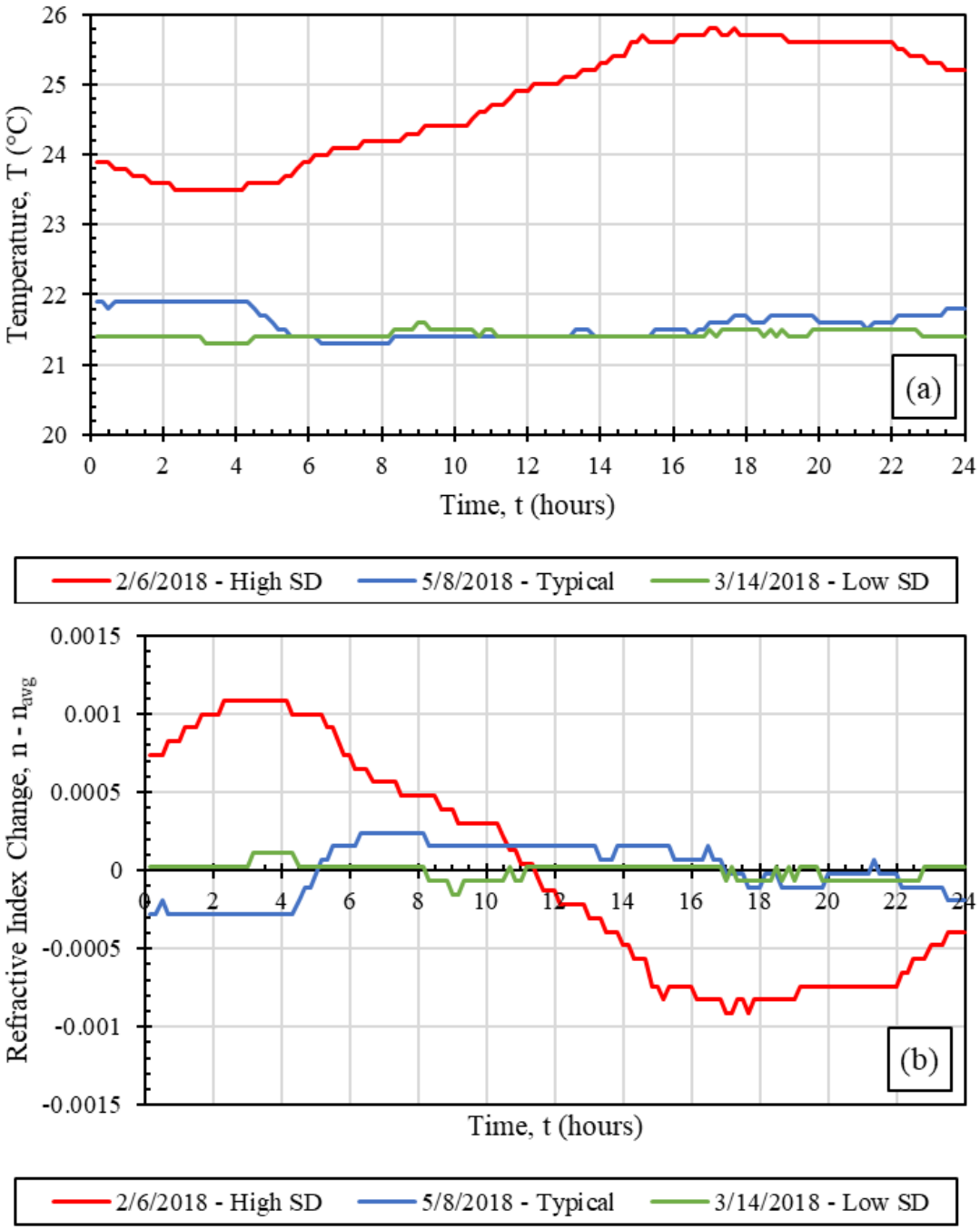

Figure 56. (a) Hourly laboratory temperature fluctuations and (b) corresponding response of oil refractive indices

4.2.3.3: Refractive Index of Mixtures

Thus far, the assumption has been made that the oil mixtures have refractive indices equal to a weighted average by volume. Despite the fact that the two oils should be completely miscible, this may not be the case according to some researchers, (Reis, et al. 2010). Other factors that may cause non-negligible changes to the refractive index of a mixture relative to the theoretical refractive index of an ideal mixture include thermodynamic effects, London dispersion forces, molar and density considerations.

There are many theoretically-derived equations for the determination of the refractive index of a mixture, all based on electromagnetic theory and the assumption that there is no change of volume during mixing, (Wiederseiner et al. 2011). These formulations include the Lorentz-Lorenz equation (Lorentz 1906), Weiner equation (Weiner 1910), Heller equation (Heller 1945), Dale-Gladstone equation (Dale and Gladstone 1858), Arago-Biot equation (Arago and Biot 1806), Lichtenecker equation (Heller 1945), and Newton equation. These equations are based on either the volume fractions, the densities, and/or the weight fractions of the pure fluids. According to one author, "There is no 'best rule,' as different rules work better for different liquid chemistry," (McClymer 2016). It is unclear which rule best applies to mineral oil mixtures.

4.2.4: Light Transmittance

One additional area of concern for the efficacy of transparent soil for large-scale geotechnical applications is the absolute light transmittance through fused quartz. Light transmittance is defined as the amount of light that passes through a material, often measured as a percent transmittance for a 10-mm thick sample. According to published data sheets, the transmittance of Heraeus HOQ 310 fused quartz is ~93% over the visible spectrum as depicted in Figure 57.

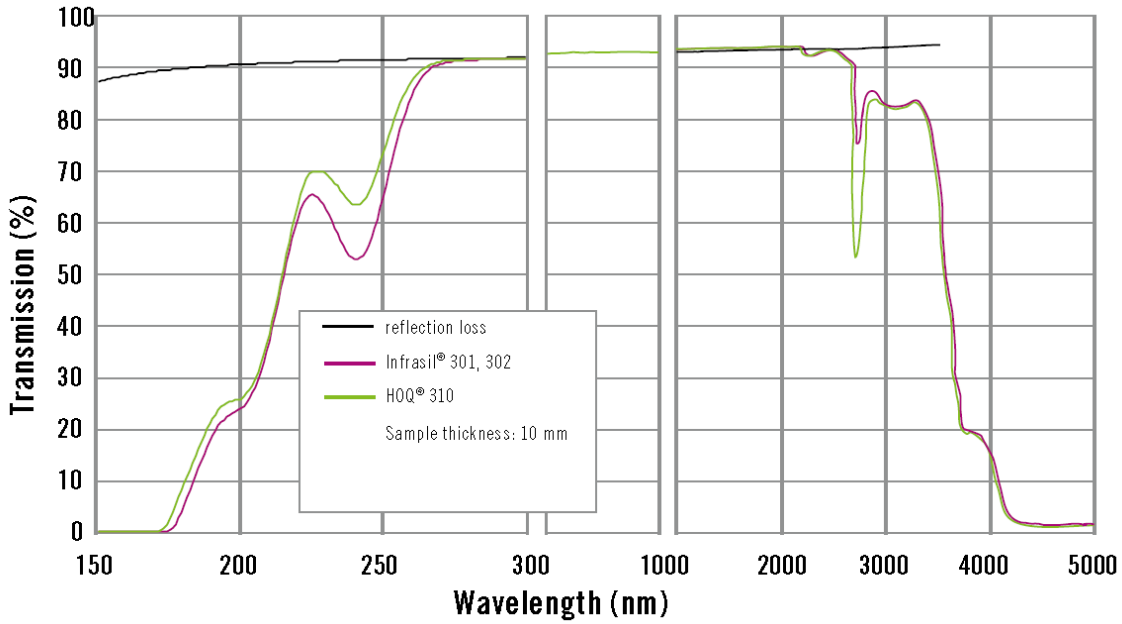

Figure 57. Typical transmittance through various fused quartz products, (Heraeus 2016)

With this information, it is possible to calculate the theoretical transmission through a solid block of HOQ 310 fused quartz of any depth. A solid block the size of the LSTSA tank (~1300 mm) would theoretically transmit less than 0.1% of the light from a light source perpendicular to its face. How this property translates to a mass of fused quartz particles is unknown and there is little research in this area. However, based on testing that will be discussed in later sections, it seems that significantly more than 0.1% of light is transmitted through the medium, although the means to measure the exact transmittance are not currently available in the laboratory.

4.3: LARGE-DEPTH TRANSPARENCY TESTING

4.3.1: Large-Depth Transparent Soil Apparatus

4.3.1.1: Purpose and Conception

The need for a large-depth transparent soil apparatus was identified after issues with the quality of the transparent soil, both major and minor, were noted and deemed to be detrimental to the required testing capabilities. As mentioned in the previous chapter, the minor issues included macro-contaminants (e.g. sand, dirt, dust, rubber shreds, and colored glass), bubbles between the acrylic sidewalls and protective Mylar sheeting, entrapped air bubbles in the soil mass, and sweat contamination. Major issues included micro-contaminants, mismatching refractive indices of the transparent soil components, and transmittance limitations.

The goals in mind during the development of the full-depth transparent soil apparatus were fourfold: 1) to rapidly test transparent soil variations at multiple viewing depths, 2) to quantify the quality/transparency of the transparent soil formulations, 3) to isolate factors that contribute to poor quality, and 4) to test solutions that address those factors. In order to accomplish these goals, the full-depth apparatus had to mimic the full-scale apparatus in the crucial dimension, the depth of the transparent soil mass perpendicular to the orientation of the plane of interest. In addition, the apparatus needed to be fabricated from the same material (clear, cast acrylic) and with the same overall thickness (maximum 2") as the full-scale apparatus to ensure the same transmission of light. A final factor under consideration was to use a relatively small volume to facilitate rapid testing of the various issues and solutions for the transparent soil material.

4.3.1.2: Design and Fabrication

The final design of the full-depth testing apparatus consisted of a long, narrow tank (OD: 48” x 5” x 4”; ID: 46” x 4” x 3.5”) built from ½”-thick clear, cast acrylic, Figure 58. Acrylic cement, a solvent used to “weld” acrylic joints, was used at the joints to eliminate the need for metal fasteners. Permanent inserts were added at the 12” and 24” locations relative to the camera-side to allow for testing at incrementally larger depths of transparent soil. These inserts added to the total depth of acrylic along the full depth of the tank to match the maximum 2” thickness of acrylic that is present if the plane of interest in the large-scale apparatus is horizontal (i.e. a view point beneath the large-scale apparatus). A target image can be attached to the outside of the side opposite from the camera’s position as a target for a Similarity Index Analysis. A simple mount was built to hold the acrylic tank and digital camera in place relative to one another; the tank is secured by wooden brackets, while the camera is secured by a bolt compatible with the camera’s tripod-mounting threads. This eliminates any bias in the Similarity Index Analysis introduced by misalignment of the camera during testing.

Figure 58. Full-depth transparent soil apparatus

4.3.2: Similarity Index Evaluation

A recent study by Beemer et al. (2016) presented a technique to quantitatively evaluate the transparency of transparent soil samples, in their case LNM silicate used as a clay surrogate. The technique, known as Similarity Index Evaluation, is a simple algorithmic process that assesses differences between a sample image and a reference image, Figure 59, and then outputs a Similarity Index value as a percentage difference between those images. The algorithm follows the process summarized below, (Beemer, et al. 2016):

1. All images converted to grayscale
2. Sample image inverted and added to reference image resulting in Image A, I_A
    a. If summed images are identical I_A will be white (1 in grayscale)
3. All entries in Image A summed, ΣI_A
4. Similarity Index calculated as percent difference between ΣI_A and the sum of a white image of the same size

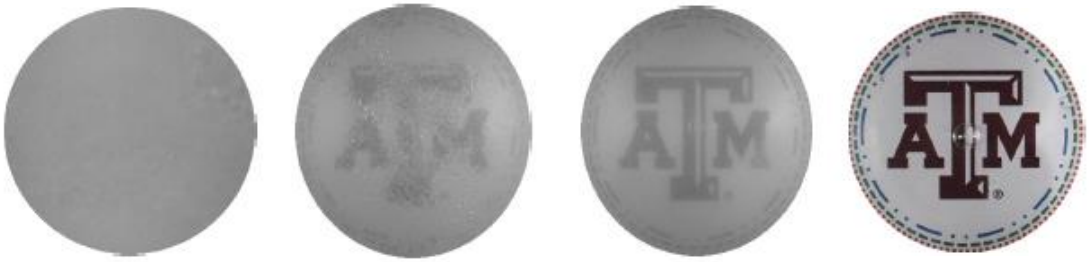

(a) (b) (c) (d)

Figure 59. (a – c) Sample images of clay simulate with increasing concentrations of an emulsifier and (d) the reference image used in the Similarity Index Evaluation

The technique, while simple and effective, is difficult to reproduce in the context of large-scale testing. First and foremost, the sample and reference images must be perfectly aligned with one another. Any misalignment will be interpreted by the algorithm

as a difference in transparency and will influence the results significantly. This problem is coupled with the refraction that occurs between the liquid within the full-depth transparent soil apparatus and the outside air, which has a magnifying effect on the image on the far side of the apparatus. If different depths of material are to be compared, a reference image must be taken at each depth to avoid this problem. Additionally, as different liquids have different refractive indices, water cannot be used as the reference for the oil-saturated transparent soil. The lighting conditions and camera settings must also be kept constant for all images to avoid other introduced errors.

Problems caused by slight misalignments were solved using one feature of the code PatchMatch, written by Dr. Gaston Quaglia and Calvin Blake at The University of Texas at Austin. Using pixel clusters, the relative shift between the reference and sample images in the vertical and horizontal dimensions was determined. This information was used to adjust the area of interest used in the Similarity Index Evaluation to the nearest pixel. This methodology was determined to be effective using images with a deliberate misalignment. The Similarity Index of the misaligned images in Figure 60 was determined to be 98.5%, and the Similarity Index of the realigned images was determined to be 99.9% as supported by the nearly pure white “combination” image in the lower right of the figure.

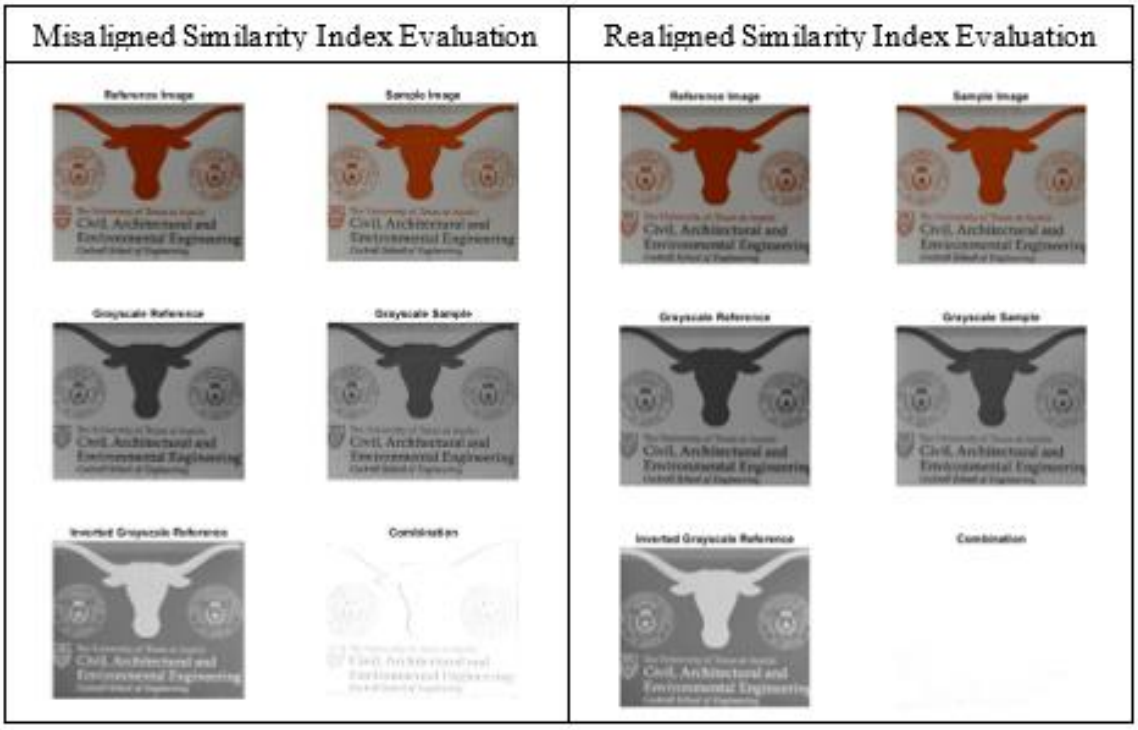

Figure 60. Results of a Similarity Index Evaluation illustrating the importance of exact image alignment

Despite the promising capabilities of Similarity Index Evaluations, the technique was not used in extensive evaluations of transparent soil quality for a number of reasons. First, the transparency of the fused quartz was so poor at the shortest depth in the full-depth transparent soil apparatus that meaningful results could not be obtained. Furthermore, soon after the development of this evaluation technique, it was established that the best possible, fused quartz-based transparent soil would still not be adequately transparent at the depths required for large-scale testing.

4.3.3: Cargille Fused Silica Refractive Index Matching Fluid

In the search for information about the refractive index material property, a specific product was found that may provide the best case for the large-scale implementation of

fused quartz as a transparent soil. Cargille Labs, based in New Jersey, USA, specializes in the development and manufacturing of optical liquids, immersion oils, and other optically-sensitive products. One of their products, Cargille Fused Silica Matching Liquid, is manufactured for the specific purpose of matching the refractive index of fused silica (fused quartz) for a broad range of light wavelengths. Figure 61 is a graph showing the dispersion curve of fused quartz in blue, of Cargille liquid in black, and of a reference mineral oil, Marcol 7 from (Aguilar-Arevalo 2008), in orange. The discrepancies between the curves of the two liquids and fused quartz are plotted as dashed lines of corresponding color on the secondary vertical axis. Note that the difference between the dispersion curves for the Cargille liquid and fused quartz is almost zero for most of the visible spectrum, approximately 390 nm to 700 nm. The minimum difference between the mineral oil and fused quartz is ~0.0028, a significant difference.

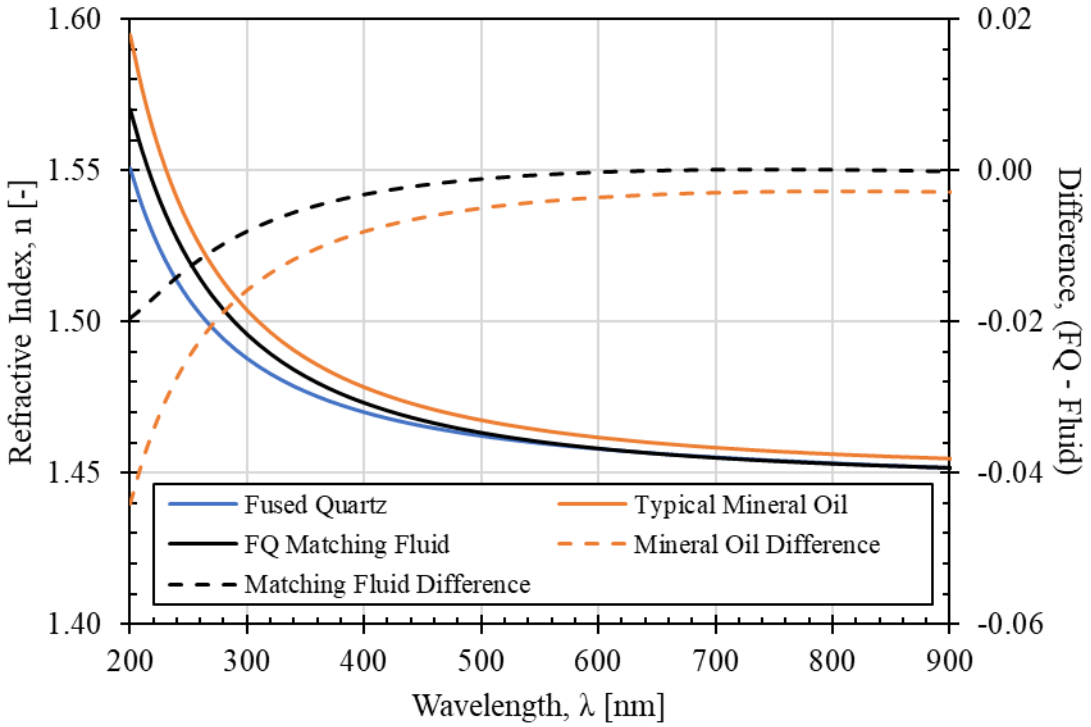

Figure 61. Dispersion curves of typical mineral oil, fused quartz, and Cargille matching liquid

It should be noted that the dispersion curve for the "typical mineral oil" is not specific to either mineral oil used in this research, but it is considered to be representative based on its refractive index at a reference value of wavelength, 1.4584 at 589 nm. Unfortunately, the dispersion curves for both mineral oils could be obtained from neither the oil manufacturer nor a third-party laboratory during the extent of this study.

As mentioned in previous sections, the dispersion curves of two materials may or may not align for any range of wavelengths. If the dispersion curves for both mineral oils align with the curve of fused quartz, then the perfect ratio of the two oils in a mixture should yield the optimum transparency, as should the Cargille Fused Silica Matching Liquid. However, in testing the Cargille liquid, it was determined that it does not perform

significantly better than any oil ratio tested. This may be the case because, despite rendering individual fused quartz particles nearly invisible when submerged, both the oil mixtures and matching liquid still allow for very minor refractions to occur, especially along sharp edges and facets. These minor refractions are not of great concern in small-scale testing, but they compound and render large depths of transparent soil virtually opaque. Further testing and modifications must be performed to provide the proper transparency with fused quartz for large-scale testing. There is potential for sophisticated lighting techniques to illuminate, or at least backlight, opaque seeding particles suspended in a planar grid at a particular depth of interest.

4.4: FULL-SCALE TESTING

Despite the number of technical challenges that still need to be overcome to create a fully transparent soil mass in the LSTSA, a full-scale optical trial was conducted to establish a baseline for the optical quality of the transparent soil.

4.4.1: Layout and Setup of Full-Scale Optical Trial

The layout of the full-scale optical trial was optimized to include a variety of embedded objects at different positions in the transparent soil mass to ascertain the degradation of visibility with depth for different materials. Three individual HDPE geocells, three individual transparent PVC geocells, and four sections of biaxial geogrid were embedded in the configuration depicted in the side and plan view below, Figure 62a and Figure 62b, respectively. The plan view is oriented such that the side view presented in Figure 62a is from the bottom. The solid grey boxes indicate the approximate position of the transparent PVC geocells and their respective cell depths. The dashed black boxes indicate the approximate positions of the HDPE geocells and their respective cell depths.

The solid black lines indicate the position of the geogrid sections. The full amount of processed fused quartz available, ~2200 lb, resulted in a maximum depth of ~16” above the bottom of the side window, ~17.5” above the base of the tank.

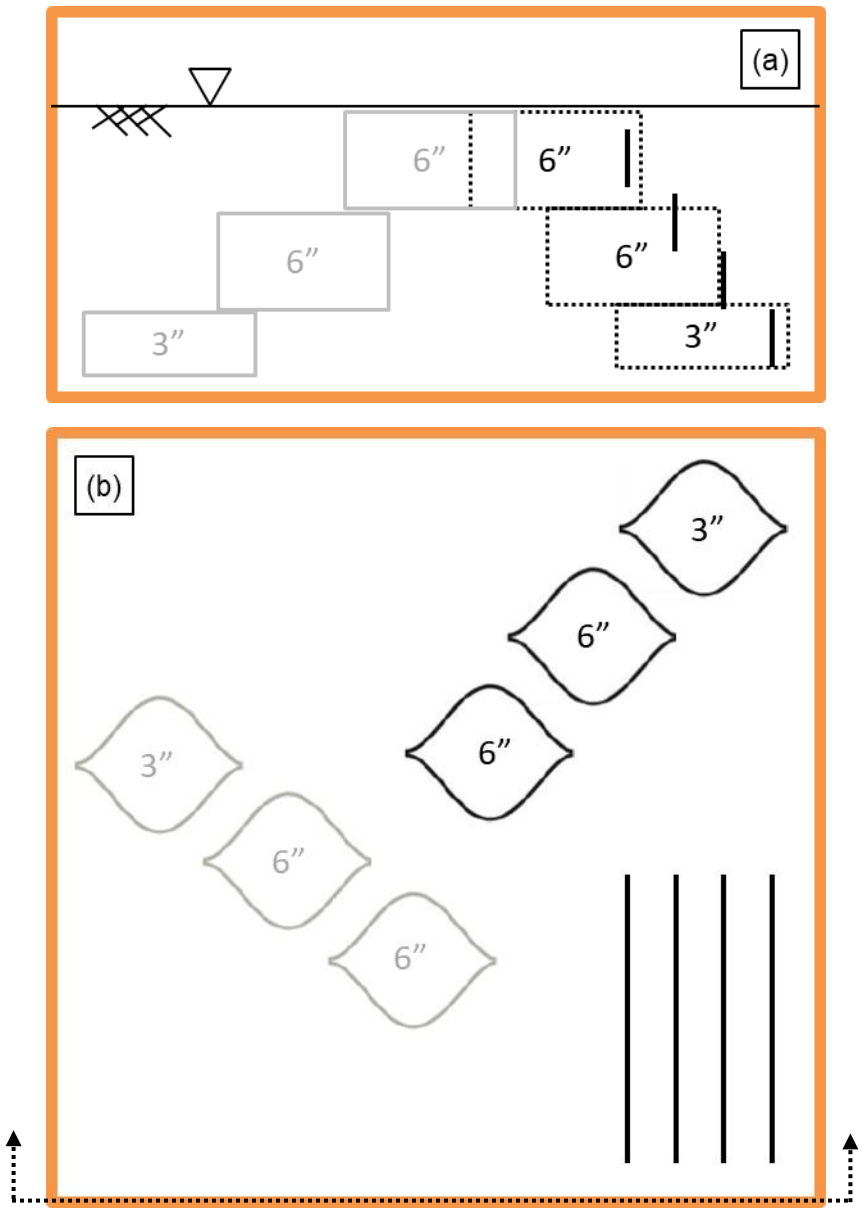

Figure 62. Layout of the full-scale optical trial in from (a) the side view and (b) the plan view

In order to ensure that no bubbles were present in the transparent soil mass, three placement/saturation techniques were attempted during the trial. First, the "wet placement" method was employed in which excess oil is pumped into the tank to reach a ponded level at least 2" above the surface above the granular particles. Then, the next lift of fused quartz was gently placed in the ponded oil. This method still required some manual agitation to remove a few bubbles in the fused quartz.

The second placement/saturation technique was the "within lift" saturation method in which a dry layer of fused quartz was placed over the top of the oil injection lines. After the lift placement, oil was pumped using the oil circulation system to saturate the lift. Significant bubbles remained trapped within the lift, especially along the interface between the two lifts and around the injection line ports.

The third placement/saturation technique, "top-down, bottom-up" saturation, involved the placement of a dry layer of fused quartz on top if which the injection lines were rested before pumping in oil. Oil flowed quickly down the sides of the tank below the injection lines, uniformly across the base of the tank, and then saturated the majority of the soil mass from the bottom-up. This method performed similarly to the "within lift" saturation method and required manual agitate to remove entrapped air bubbles. Perhaps with a much slower flow rate, the oil would be able to flow steadily through the pore spaces without entrapping bubbles within the soil mass.

In addition to the ability to test placement/saturation procedures, the set-up of this full-scale trial was the first opportunity to remove a significant amount of the macro-contaminants still remaining in the crushed fused quartz. As such, significant time was spent manually removing all possible macro-contaminants after the placement of each 1"-thick lift. All of the macro-contaminants removed from the material were kept in a large container, Figure 63.

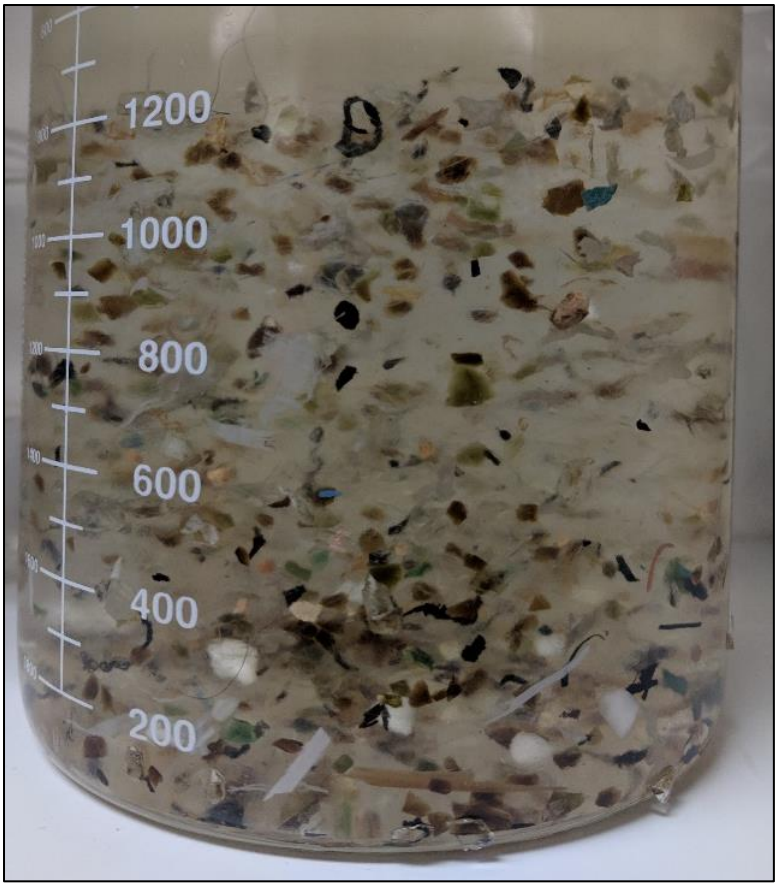

Figure 63. Macro-contaminants removed from the processed fused quartz during the set-up of the full-scale optical trial

4.4.2: Results of Full-Scale Optical Trial

Figure 64 through Figure 67 are the best quality images obtained from each side of the LSTSA during the full-scale optical trial. These images were obtained using fluorescent photography studio-style lighting fixtures to provide sufficient backlighting. With this lighting condition, it is possible to clearly see the biaxial geogrid approximately 12” away from the viewing plane in Figure 65. This is the best indication that a grid of opaque soil

particles could be used to track full-field soil particle displacements at depths of at least 12” within the transparent soil mass.

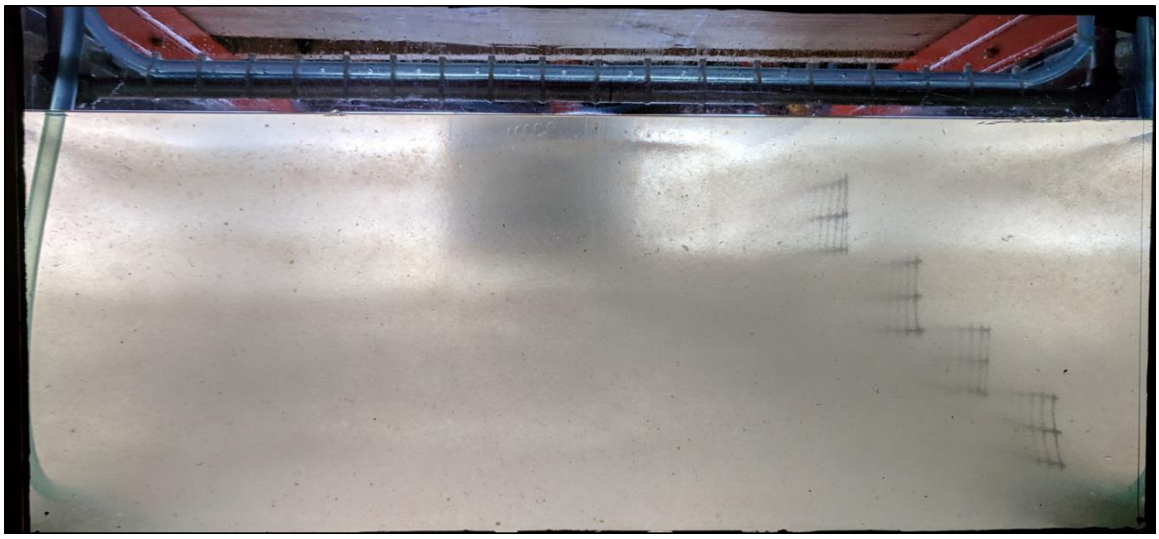

Figure 64. Full-scale optical trial, Side 1

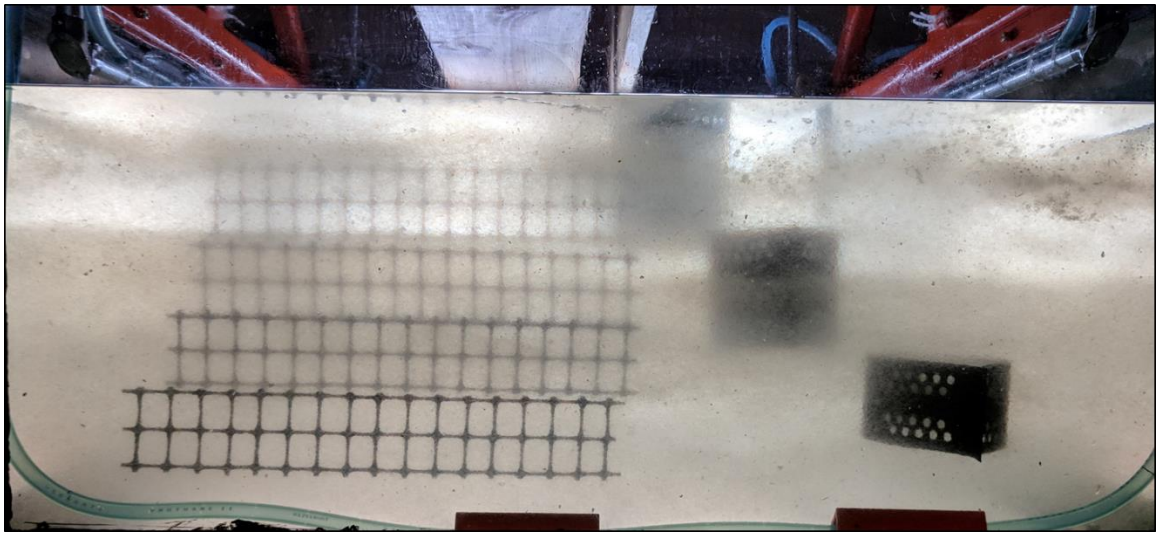

Figure 65. Full-scale optical trial, Side 2

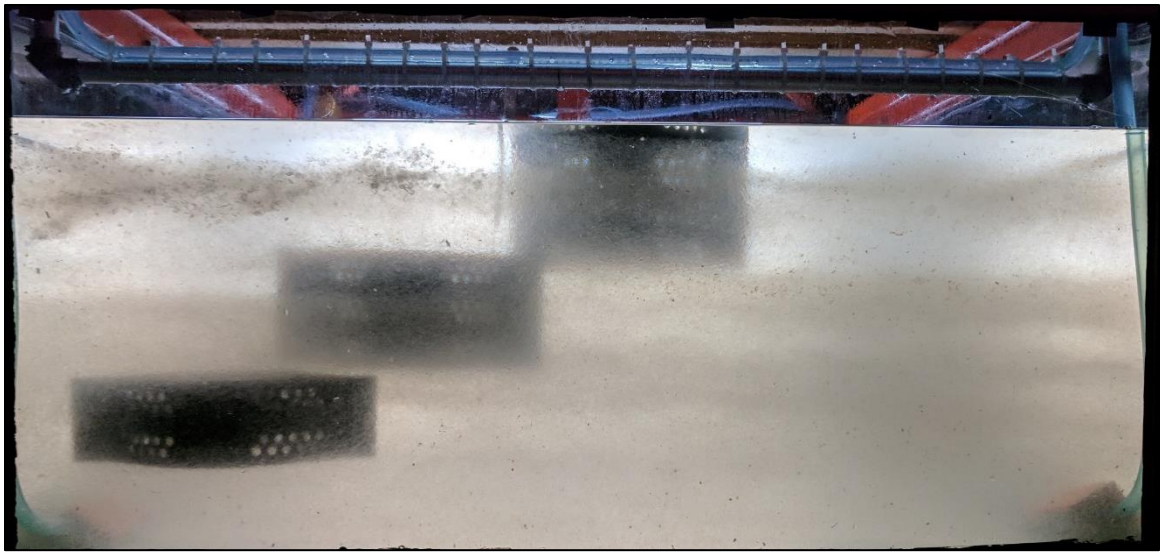

Figure 66. Full-scale optical trial, Side 3

Figure 67. Full-scale optical trial, Side 4

Note that the maximum resolution and precision possible with opaque soil particles is less than that with a laser-illuminated plane, (Ferreira 2013), but the laser plane is not adequate for full-field illumination in the full-scale setup. The divergence of the laser plane across the full 50.5” width of the LSTSA is depicted in Figure 68. The vertical line indicates

the approximate position and width of the initial laser plane on the far side of the LSTSA. The dashed oval represents the extent to which the light spread over a 48” travel path, although the overall red glow in the transparent soil mass is indicative of even more extensive internal refraction.

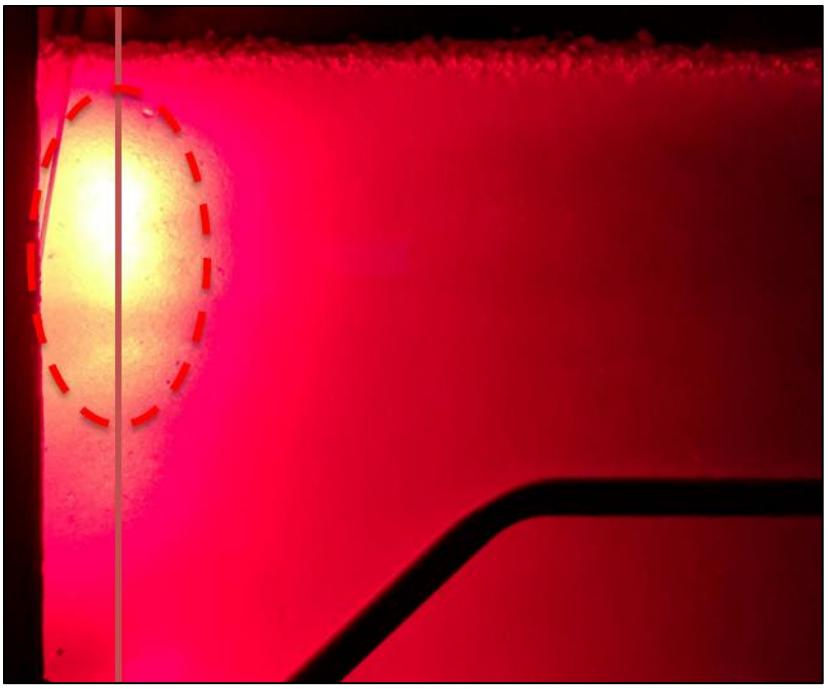

Figure 68. Divergence of light from the laser plane after passing through 48" of transparent soil in line with the output direction

When viewed from the side parallel to the plane of the laser, the result is as depicted in Figure 69. Note, the laser plane is being shone from left to right in Figure 69. Close inspection and careful adjustment of camera settings would reveal good illumination of particle boundaries within the left-most 12” similar to that depicted in Figure 44, but with a steady degradation until the soil mass appears as an untextured red glare on the far right. Additionally, this test was conducted with the laser plane 4” from the side wall of the

LSTSA. The entire soil mass appears as a red glare when the centerline of the tank, a full 24” from the viewing plane, is illuminated with the laser plane instead.

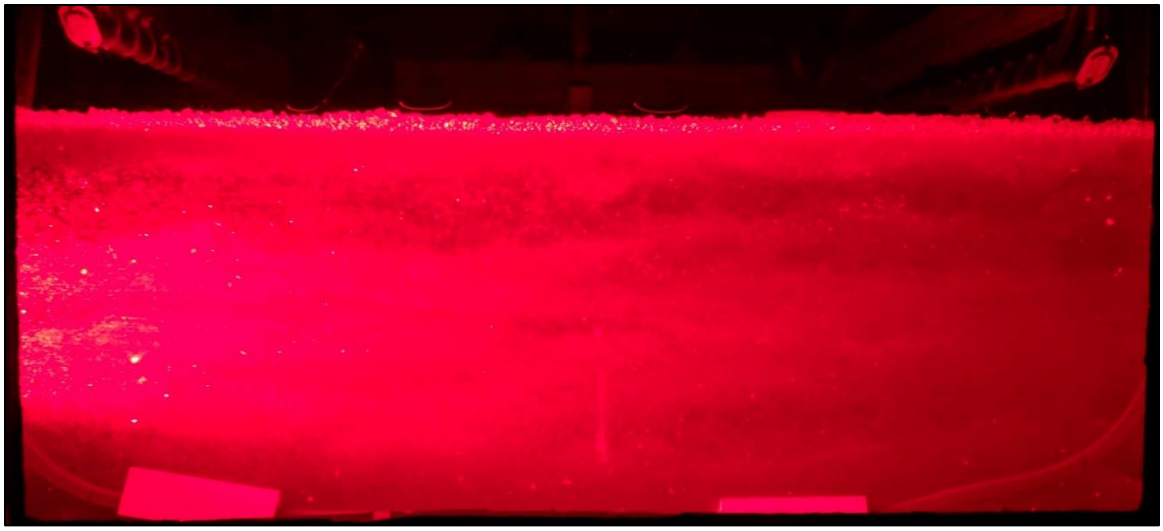

Figure 69. Divergence and diffusion of light from a laser plane through the large-scale transparent soil mass

4.5: LESSONS LEARNED

Overall, the full-scale optical trial resulted in a number of important lessons that influenced the procedures and goals for the subsequent tests. First, it is clear that, despite best efforts to the contrary, the transparent soil developed during this study is not yet adequate for the observation and quantification of full-field soil particle displacements on the main plane of interest, the center line directly beneath the footing. However, near-surface displacements and planes within 12” of the LSTSA side walls may be visible with the current quality of the transparent soil.

The three placement/saturation procedures, “wet placement”, “within lift” saturation, and “top-down, bottom-up” saturation, all resulted in the need for manual agitation to remove entrapped air bubbles. However, manual agitation is not necessarily

conducive to consistent and uniform density of soil placement, so, for the next suite of tests involving the operation of the loading system and physical measurement devices, the bubbles and most optical considerations were ignored in favor of rapid, consistent, and uniform placement and compaction. Measures should be taken during later test series to accommodate both consistent soil densification and optical quality (i.e. bubble removal).

Chapter 5: Typical Large-Scale Transparent Soil Apparatus Results

A total of four full-scale tests were completed to verify the operation and preliminary capabilities of the LSTSA. Initially, one unreinforced test and one geocell-reinforced test were planned, but complications required repeats of both tests. In general, all tests were constructed of 8 lifts placed and compacted in a dry condition. Displacement sensors were placed in identical layouts between unreinforced and reinforced trials; a minor change was implemented between the first and second pair of tests to allow for transparent soil observation from a different angle. Top-down saturation was performed after sensor setup was completed. The prescribed loading sequence for all tests consisted of 50-lb load increments applied at approximately 1.5-min intervals. This loading sequence was maintained until the piston reached its full stroke. These tests will be referred to as U1 and R1, the first pair of unreinforced and reinforced tests, and U2 and R2, the second pair, for the remainder of this chapter.

5.1: TEST SETUP

5.1.1: Placement, Compaction, and Density

The main objective of these tests was verification of the operation of the loading system and physical measurement devices, so the bubbles and most optical considerations were ignored in favor of rapid, consistent, and uniform placement and compaction. As such, the dry placement and "top-down, bottom-up" saturation method was selected. A target density of 80 pcf was selected. Based on the available supply of processed fused quartz, it was determined that, at this density, the maximum depth of soil in the LSTSA would be approximately 17.5 inches. Thus, this full height was subdivided into 8 lifts. The fused quartz for each lift was weighted and poured gently into the tank. Then it was leveled with a flat-bladed metal scraper and compacted to the desired height with the an 8"-square

cast iron hand tamper. The compaction procedures were not as consistent from lift to lift as one might hope, but the average density of each test was nearly 85 pcf, slightly above the target density, see Figure 70. A full compaction record for each test is included in Appendix B.

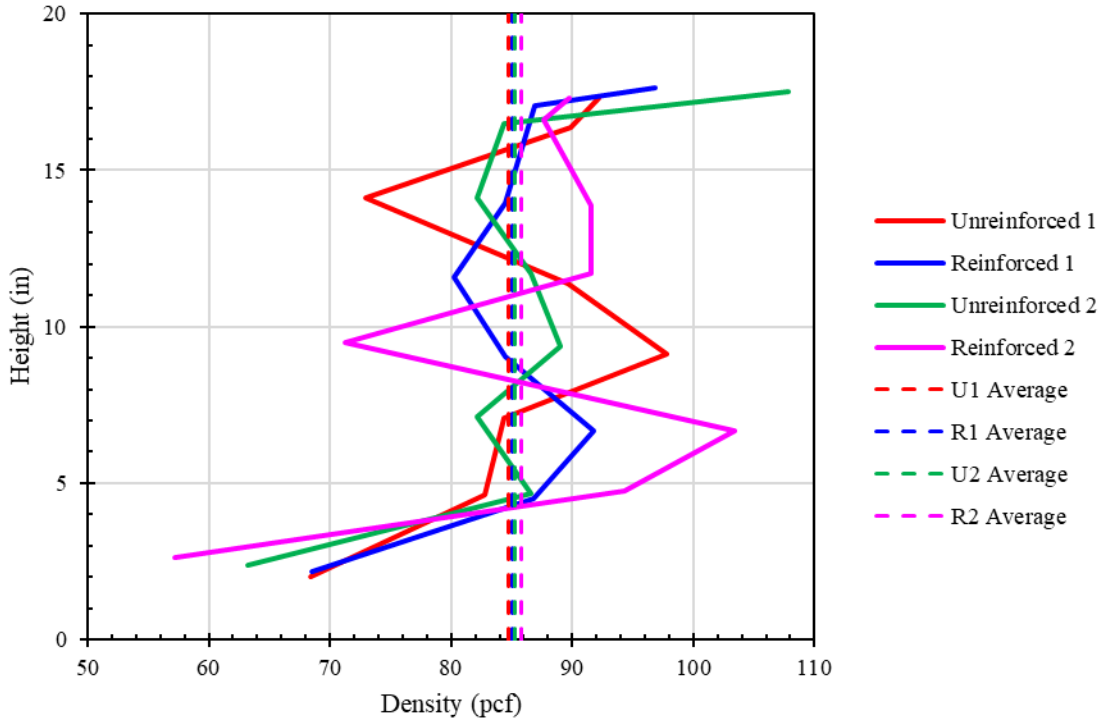

Figure 70. Compaction record from the four full-scale tests

A possible explanation for the increasing trend of measured density with increasing height in each test is that, before the material was weighted, it was stored in 55-gal drums. Because the material is reused after each test, there is still some oil coating the fused quartz particles when they are removed from the LSTSA. After some time at rest, the oil drips to the bottom of the drum. The first lifts were constructed of material from the top of the 55-gal drums, while subsequent lifts consisted of material from the bottom of the drums.

Because the material at the bottom of the drums is slightly saturated, it has a greater density. Procedures for more consistent placement and compaction should be employed for future testing.

In the case of the reinforced test, the geocell was placed in the 7th lift with its base approximately 14" above the base of the LSTSA tank. HDPE$_t$ GC 1-150 test sections were used for both tests, so the top of the geocell layer reached approximately 17" leaving another 0.5" for a cover layer. It should be noted that the geocell test sections were filled and leveled, but not immediately compacted. The final compaction was performed after the placement of the cover layer to prevent damage to the geocell itself. This is in accordance with standard geocell installation practices in the field, (Strata Systems, Inc. 2016).

5.1.2: Sensor Layout

The displacement sensors were laid out in such a way as to capture a full profile of soil surface displacement in line with the center of the footing and observe whether or not the geocell reinforcement behaves differently on its perpendicular axes. Because of the number of displacement sensors available (12) and four are committed to measuring footing displacement, only eight sensors were available to measure soil surface heave and/or settlement. Six of these sensors, referred to hereinafter as the main beam sensors, M1 – M6, were laid out along the centerline of the footing with three on each side. The closest sensors to the footing, M3 & M4, were 4" from the edge of the footing to the center of their hanging weight. The middle and furthest sensors, M1, M2, M5, & M6, were spaced 4" on-center. The remaining two sensors, the offset sensors O1 & O2, were placed in the same position relative to the footing as M3 & M4, but on the perpendicular axis. This layout is illustrated in Figure 71 and depicted on an unreinforced test bed in Figure 72. In U2 and

R2, sensor O1 was not used to allow for unobstructed image capture of a laser plane illuminated region near the edge of the footing.

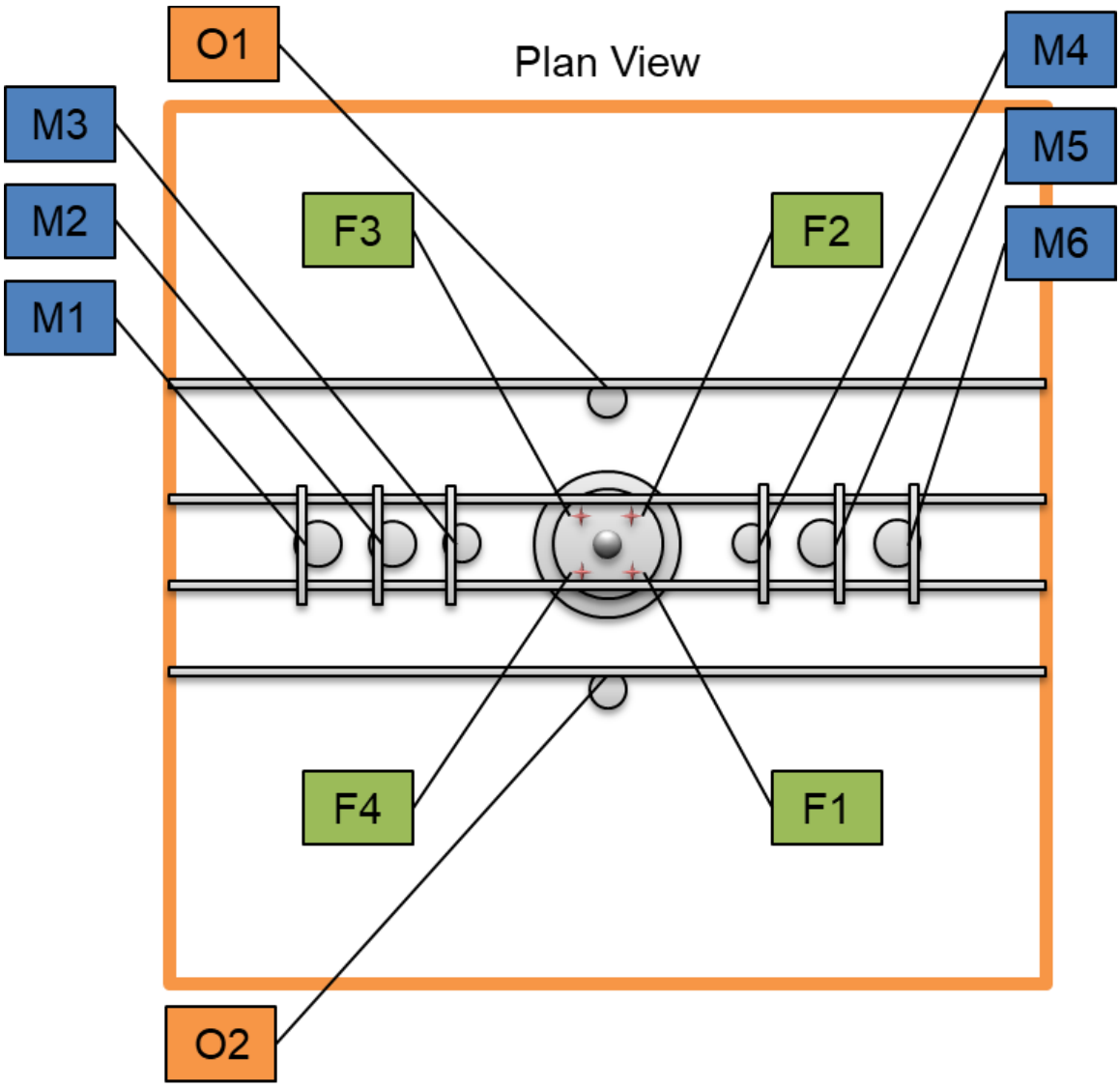

Figure 71. Illustration of the sensor layout pattern used in all four tests

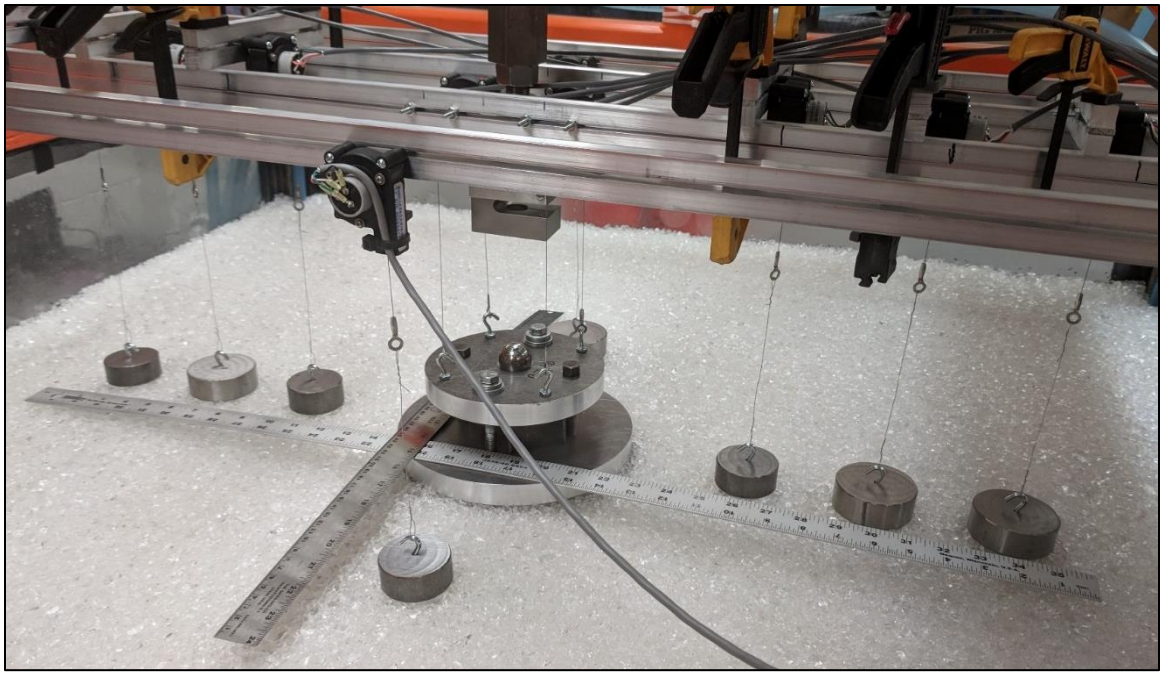

Figure 72. Complete sensor layout on an unreinforced test bed

5.2: UNREINFORCED SOIL BEHAVIOR

Tests U1 and U2 were conducted to determine the performance of the unreinforced transparent soil as a baseline with which to evaluation the geocell-reinforced performance. The results of U1 are subject to scrutiny as the test was disrupted by an accidental pre-test load application and footing embedment. The internal friction and lag between pressure increases and load application during test setup caused the loading system to contact the footing prior to the start of the data acquisition system. It is estimated that the magnitude of this pre-loading was approximately 700 lbs and resulted in approximately 0.5” of embedment. U1 and U2 were stopped when the piston reached the full extent of its stroke length; modifications were made to the footing for R1 and R2 to extend the embedment range.

5.2.1: Load Versus Footing Displacement

The load-displacement response of the footing in both unreinforced tests is presented in Figure 73a. The same results are presented in Figure 73b as bearing pressure (applied load / footing area) in psi versus footing settlement ratio (footing diameter / displacement) as a percentage. It is clear that the pre-load in U1 had a significant impact on the recorded results. The bearing capacity for these tests can be defined as the pressure at which the first major change in displacement occurred. The bearing capacity of U1 was approximately 16 psi, and the bearing capacity of U2 was approximately 2 psi. Because of the load-controlled condition and resultant failure mechanisms, these results are difficult to compare with classical bearing capacity theories. An alternative failure criterion could be the load at which the footing reached a specific footing settlement ratio, say 10%. Using this definition, U1 failed at ~32 psi U2 failed at ~19 psi.

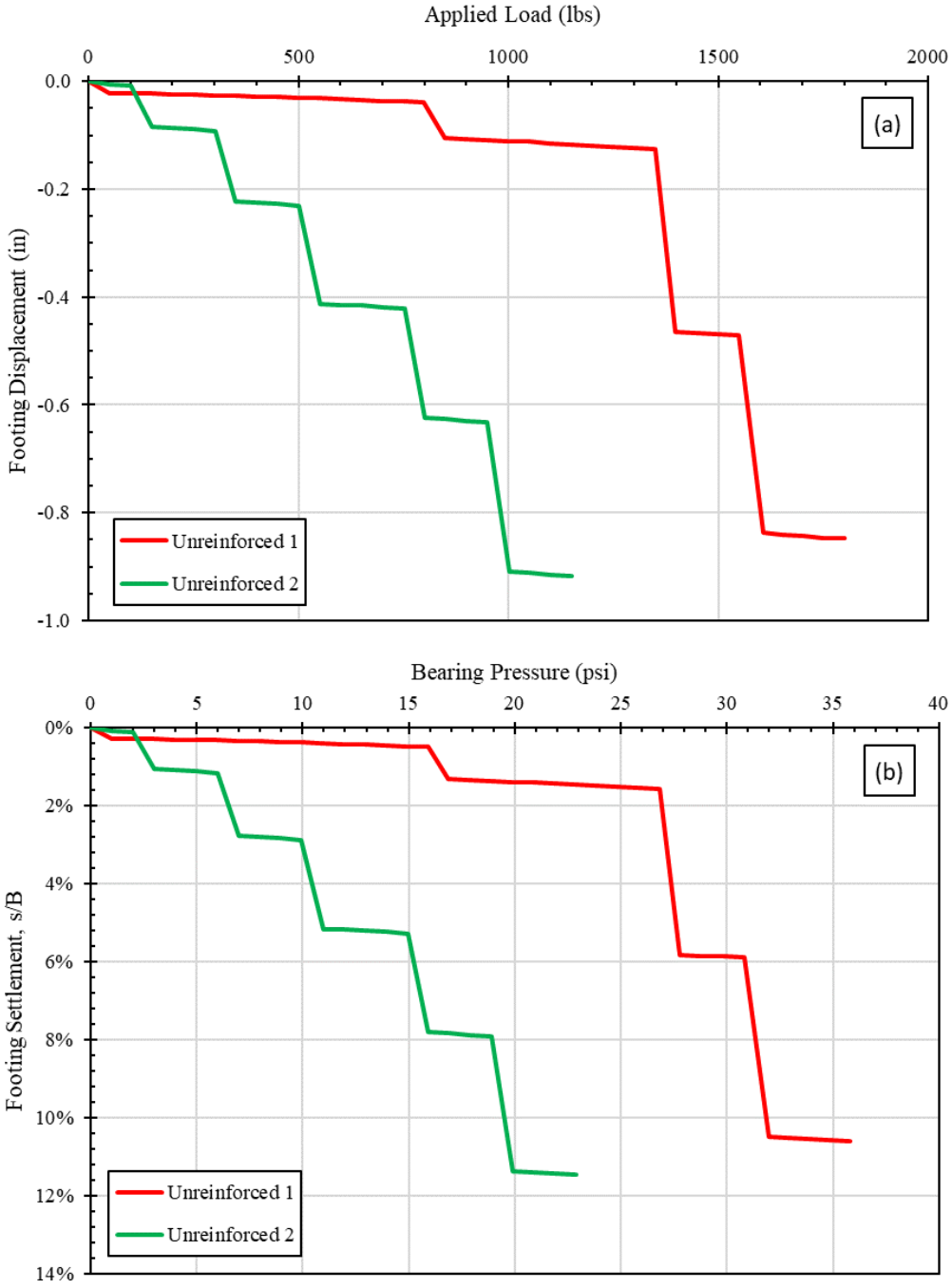

Figure 73. (a) Load vs displacement and (b) bearing pressure vs settlement response of U1 and U2

Because this is a load-controlled test, the failure mode is characterized by sudden, successive punching failures. During each punching failure, there is an immediate decrease in applied load which is regained as the pneumatic system reestablishes the air pressure in the piston. This response is more evident when the applied load and footing displacement are presented individually as a function of time, Figure 74. These data are provided for each test in Appendix B.

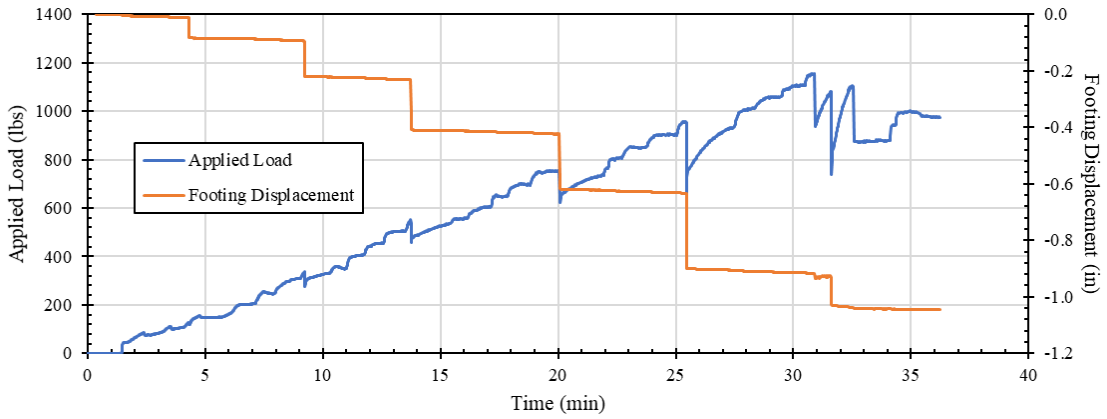

Figure 74. Applied load and footing displacement as a function of time during U2

5.2.2: Soil Surface Profiles

The displacement of the footing and soil surface, as measured by the average footing displacement and the six sensors on the main beam, can be used to create soil surface profiles at each increment of load, Figure 75. The behavior of the soil surface is indicative of the behavior of the unreinforced and the geocell-reinforced soil masses.

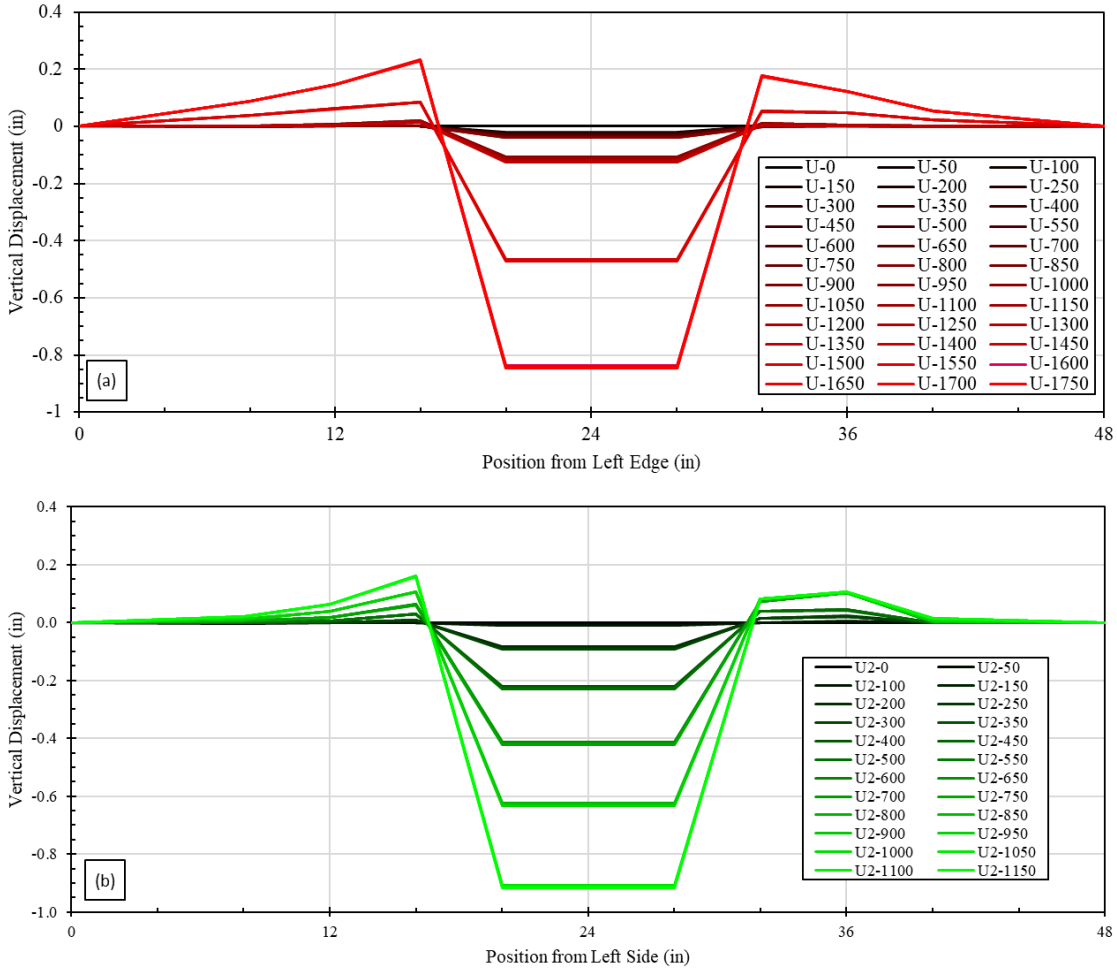

Figure 75. Soil surface profiles from (a) U1 and (b) U2

The soil surface profiles of U1 and U2 indicate that the soil adjacent to the footing heaves up significantly as the footing is pushed downward. In both unreinforced tests, the adjacent soil heaves ~0.2" by the end of the test when the footing displacement is ~0.9".

5.2.3: Visual Observations

Direct observation of the footing and soil surface monitors were not particularly useful during the unreinforced tests. It was clear that the soil adjacent to the footing was

heaving significantly. Also, a slight tilt of the footing was noted, but this can be quantified after analysis of the four footing displacement sensors.

5.3: GEOCELL-REINFORCED SOIL BEHAVIOR

5.3.1: Load Versus Footing Displacement

The load-displacement response of the footing in both reinforced tests is presented in Figure 76a. The same results are presented in Figure 76b as bearing pressure (load / footing area) in psi versus footing settlement ratio (footing diameter / displacement) as a percentage. In an attempt to mimic the accident pre-load applied during U1, an intentional pre-load was applied to R1. This intentional pre-load was recorded, and the full results are presented in Appendix B. The maximum load applied during the pre-load was approximately 750 lb, which resulted in a footing displacement of 0.25".

Comparing the two reinforced tests, the effect of the pre-load is noticeable but not as evident as in the unreinforced tests. The pre-loaded R1 test had a bearing capacity of approximately 11 psi, while the virgin R2 has a bearing capacity of approximately 5 psi. Both tests follow the same trend of bearing pressure versus footing settlement ratio during the loading sequence except for a lag by R2. Using the 10% settlement ratio failure criterion, R1 failed at ~30 psi, while R2 failed at ~22 psi.

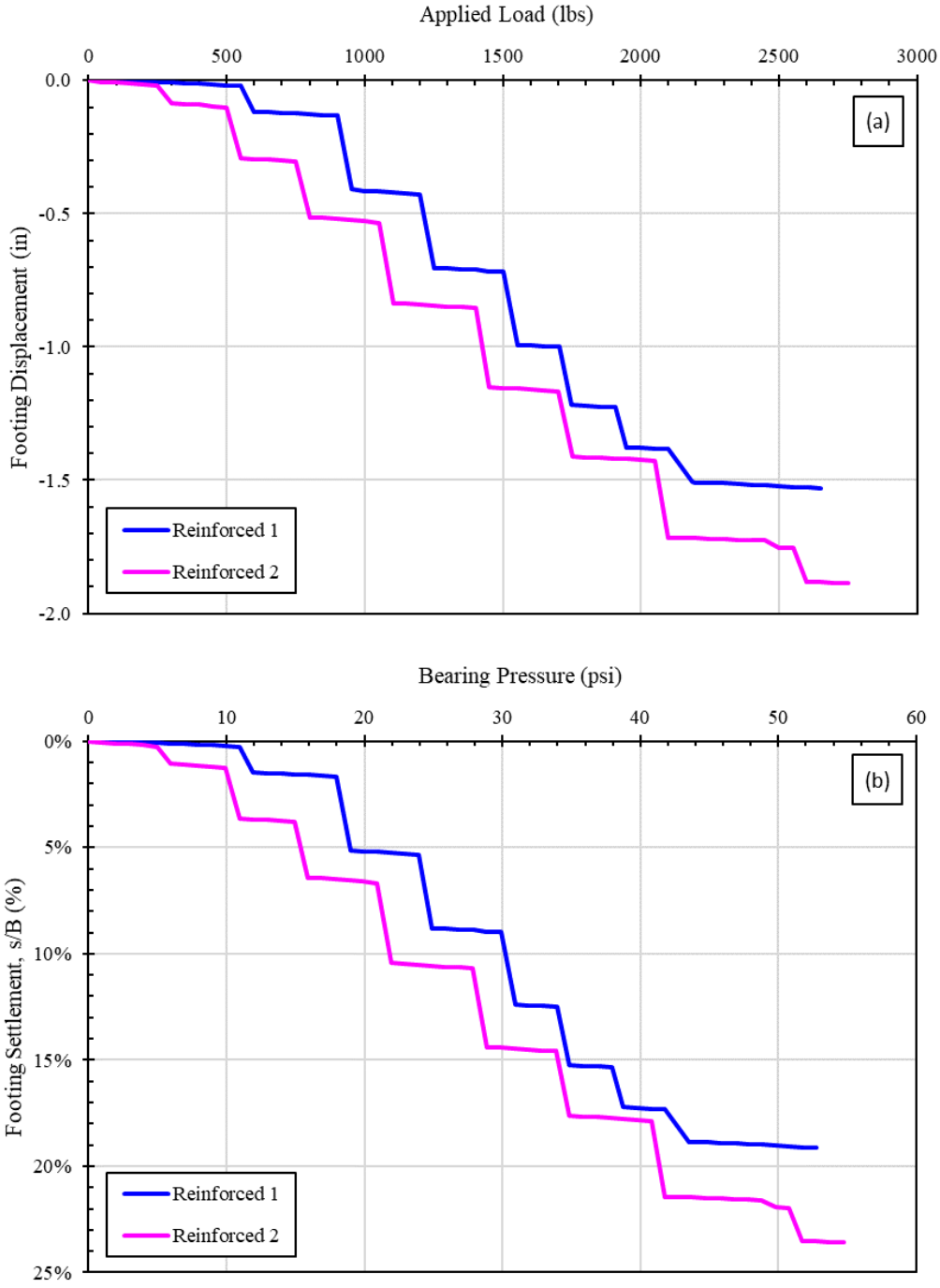

Figure 76. (a) Load vs displacement and (b) bearing pressure vs settlement response of R1 and R2

5.3.2: Soil Surface Profiles

The soil surface profile from R1, Figure 77a, demonstrates significant heave, although unlike the unreinforced tests, the maximum heave (~0.3") occurred at the middle set of displacement sensors, not those closest to the footing. This is indicative of a deeper and wider failure plane relative to the unreinforced cases. A comparison of R1 and R2 is somewhat contradictory. The maximum heave experienced by the soil surface during R2 was only 0.1", significantly less than all other tests, although both tests suggest a wider generalized failure pattern and localized settlement within 4" of the footing perimeter.

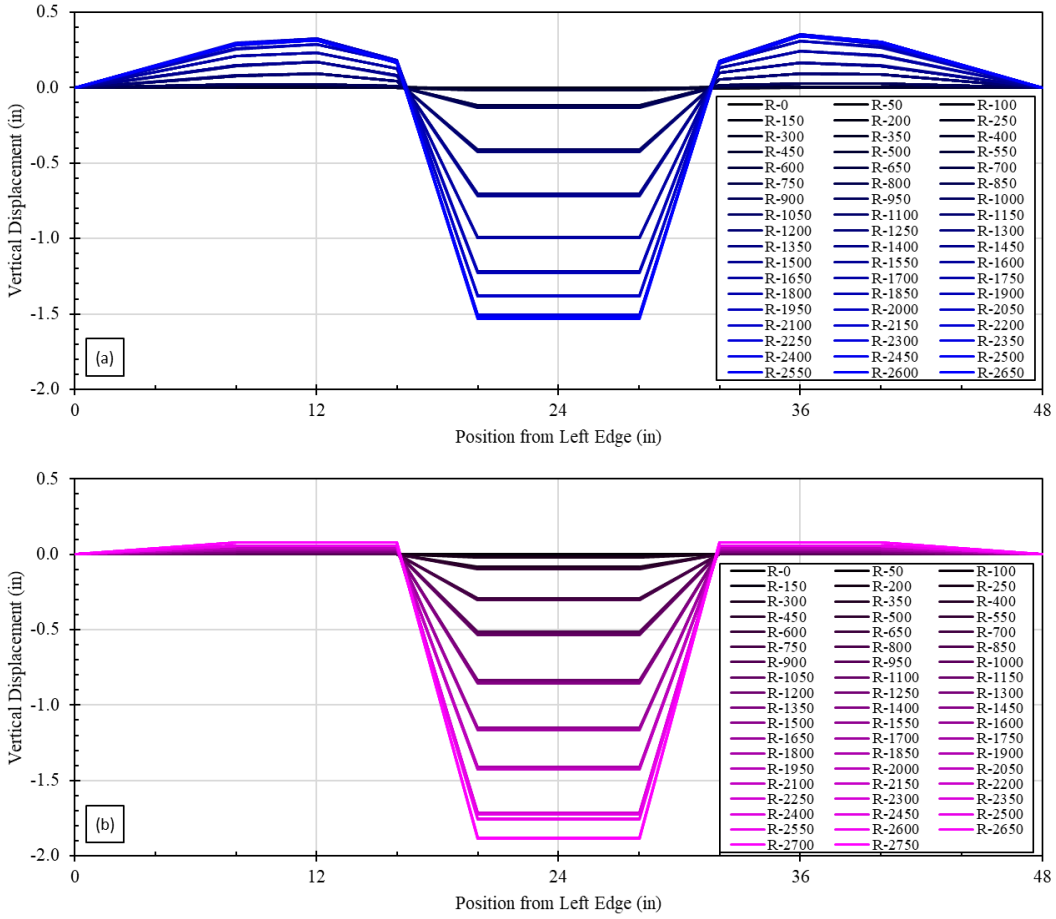

Figure 77. Soil surface profiles from (a) R1 and (b) R2

5.3.3: Visual Observations

Like the unreinforced tests, direct observation during the reinforced tests was also not the main source of information in the current setup. However, after completion of the loading sequence and removal of the soil surface displacement sensors, it was possible to see significant deformations of the geocell directly beneath the footing. The geocell side walls had partially collapsed at points where it was directly under the footing. At points where the geocell side wall was outside the extent of the footing, the geocell bulged slightly outwards.

The reinforced tests showed less overall heave on the soil surface adjacent to the footing and even some settlement very close to the footing. The settlement was observed, not measured, as it occurred closer to the footing than the closest soil surface displacement sensor (i.e. within 4" of the edge of the footing). The hanging weights closest to the surface were clearly tilting in towards the footing at the end of the test despite indicating an overall heave at the 4"-mark.

5.4: Comparison of Unreinforced and Geocell-Reinforced Performance

Figure 78 presents a comparison of the bearing pressure-footing settlement responses from all four tests. These results are not completely conclusive, but when the accidental and intentional pre-loads in U1 and R1, respectively, are accounted for, the geocell-reinforced soil has a higher bearing capacity. A summary of the important results of the physical measurements from all four tests is provided in Table 6.

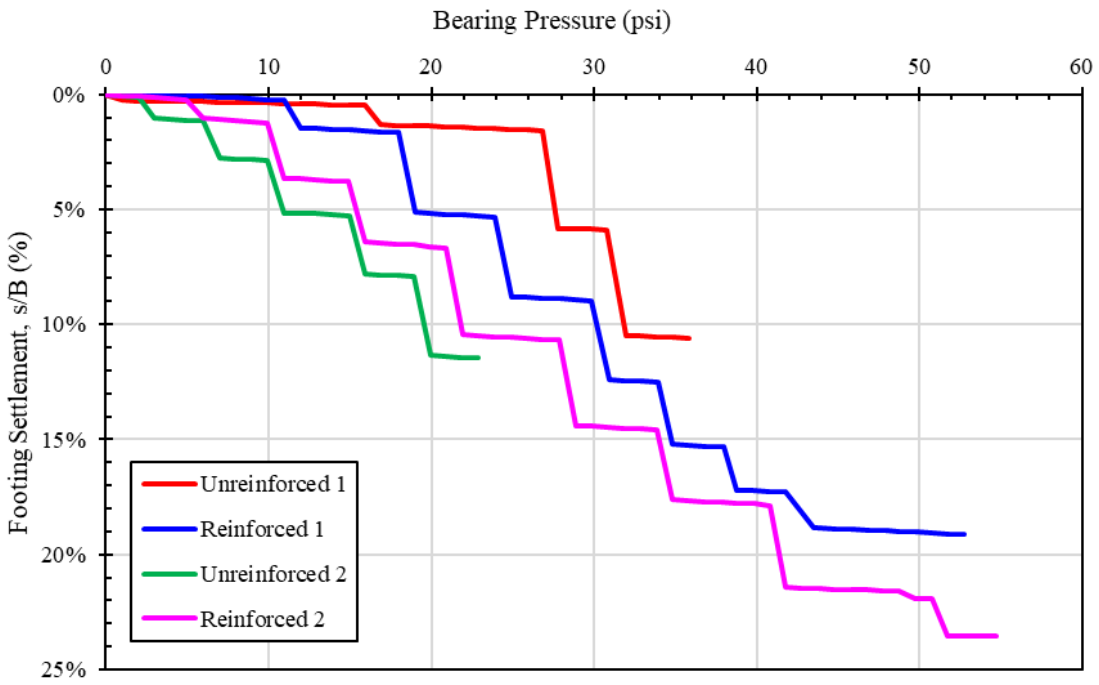

Figure 78. Bearing pressure vs footing settlement response of all four tests

Table 6. Summary of physical measurement results of all four tests

Test	U1	U2	R1	R2
Condition	Pre-loaded	Virgin	Pre-loaded	Virgin
Bearing Capacity @ First Major Disp.	16 psi	2 psi	11 psi	5 psi
Bearing Pressure @ s/B = 10%	32 psi	19 psi	30 psi	22 psi
Maximum Applied Pressure	36 psi	23 psi	53 psi	55 psi
Maximum Footing Settlement	11%	12%	19%	23%
Maximum Soil Surface Heave	0.25"	0.3"	0.15"	0.1"

The most relevant comparison of the four tests to quantify the benefit of geocell reinforcement is between U2 and R2, the two tests with a virgin soil mass (without any pre-load condition). Looking at the results depicted in Table 6, the reinforced soil mass performed substantially better. The first major displacement occurred at 5 psi during R2, while the same displacement occurred at only 2 psi during U2. Additionally, the bearing pressure at a 10% settlement ratio was 3 psi greater for the reinforced case. Finally, the soil

surface heave adjacent to the footing was only 0.1” at the end of R2, while it exceeded 0.3” by the end of U2.

5.5: Laser Plane Capabilities

As noted in previous sections, additional effort is required to reach a transparent soil quality adequate to observe full-field soil particle displacements on the centerline beneath the footing. However, it was found that with the current capabilities a laser plane illuminating a localized region of soil directly adjacent to the footing from an angled position above the soil surface could be captured with a camera positioned similarly but perpendicular to the laser plane. An image depicting this set up is provided in Figure 79.

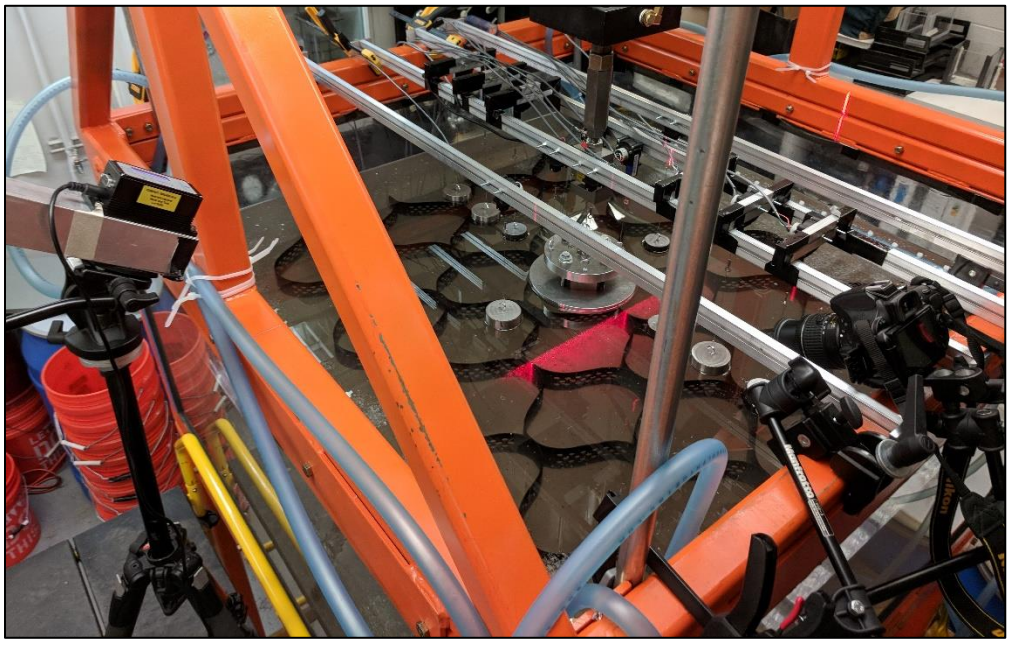

Figure 79. Camera and laser positioned to capture soil particle displacement adjacent to the footing during R1

Images were taken from this camera position after every load increment and after any significant footing displacement event. Example images taken at various load

increments during U2, Figure 80a-d, demonstrate the potential to visualize and quantify soil particle displacements in this region. However, no DIC analysis was conducted on the images from any test at the time of writing. DIC analysis would be complicated by a number of factors including:

- Distorted perspective due to the refraction through the oil surface
- Soil particle movement perpendicular to the laser plane
- Soil particles breaking the oil surface due to significant heave during later test stages that blurs particle boundaries

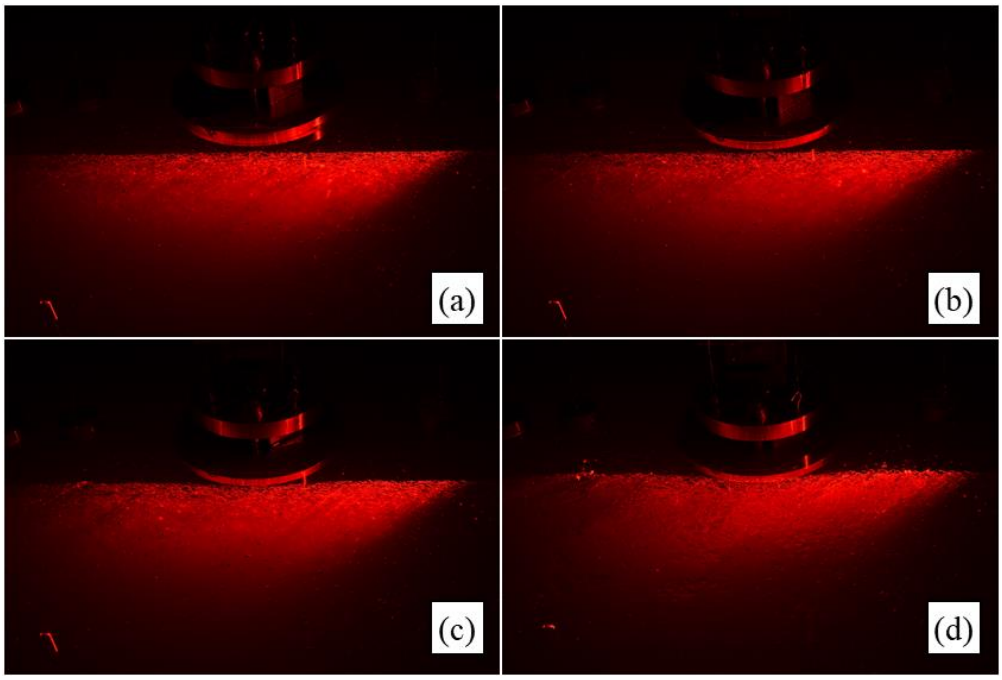

Figure 80. Selected images of soil illuminated by a laser plane during U2

Chapter 6: Potential Transparent Soil Capabilities

6.1: Summary of Current Testing Capabilities

To summarize, the current testing capabilities of the LSTSA and associated equipment include:

- Physical measurement of footing displacement, soil surface displacement, and the applied load,
- Direct observation of post-test condition, including the condition of the geocell in-situ and undisturbed, and
- Localized laser plane illumination of limited near-surface regions, although the possibility of using these results for accurate DIC analysis is complex due to the necessary viewing angle and other distortions.

These capabilities are sufficient, at least, to recreate and validate the results of nearly any full-scale geocell experiment performed to date. In fact, the direct observation and localized laser plane illumination are significant improvements on typical experiments. However, these limited capabilities fall far short of the initial capabilities that were desired for these experiments. The list of fully-functional testing capabilities includes:

- Full-field displacement and strain mapping of soil particles on vertical planes located, at the extreme, on the centerline beneath the footing,
- Full-field displacement and strain mapping of soil particles on horizontal planes at various elevations relative to the soil surface and geocell mattress,
- Side-on observation of HDPE geocell behaviors and the quantification of tensile strains due to bending under load,

- Bottom-up observation of HDPE geocell behavior and the quantification of radial expansion of the loaded cell and corresponding collapse of adjacent cells, and
- Side-on and bottom-up observation of soil particles within transparent PVC geocells and the quantification of soil-reinforcement interactions such as shear between cell walls and infill soil.

Currently, these capabilities are limited by the diminished transparency of the fused quartz at significant depths. At minimum, visual clarity must be achieved at the center of the 50.5”-wide LSTSA tank. These capabilities are necessary in order to fully understand and quantify the behaviors and mechanisms of geocell-reinforced soil for the development of a design method compatible with the Mechanistic-Empirical Pavement Design Guide.

6.2: PROPOSED TESTING MATRIX

Despite the current limitations of the LSTSA and transparent soil, a parametric evaluation schedule has been developed that will yield the necessary understanding of geocell behavior provided the proper testing capabilities. The proposed testing matrix is based on the available geocell test sections and is summarized in Table 7. The range of aspect ratios, cell depth-to-footing width ratio, cell size-to-footing witch ratios, material stiffnesses, and material textures will allow for comprehensive data collection on the influence of each of these parameters on geocell reinforcement mechanisms in-situ.

Table 7. Available geocell test sections

Section	Material	Weld Spacing (mm)	Expanded Cell Dimensions Width (mm)	Length (mm)	Depth (mm)	h/d_e Ratio	Cells	Quantity # of T.S.
GC 1-75	Transparent PVC	**356**	259	224	**75**	**0.4**	4x4	4
GC 1-150	Transparent PVC	**356**	259	224	**150**	**0.8**	4x4	4
GC 1-300	Transparent PVC	**356**	259	224	**300**	**1.6**	4x4	4
GC 2-38	Transparent PVC	**178**	129.5	112	**38**	**0.4**	8x8	4
GC 2-75	Transparent PVC	**178**	129.5	112	**75**	**0.8**	8x8	4
GC 2-150	Transparent PVC	**178**	129.5	112	**150**	**1.6**	8x8	4
GC 3-19	Transparent PVC	**89**	64.75	56	**19**	**0.4**	16x16	4
GC 3-38	Transparent PVC	**89**	64.75	56	**38**	**0.8**	16x16	4
GC 3-75	Transparent PVC	**89**	64.75	56	**75**	**1.6**	16x16	4
GC 1-75	Textured HDPE	**356**	259	224	**75**	**0.4**	4x4	4
GC 1-150	Textured HDPE	**356**	259	224	**150**	**0.8**	4x4	4
GC 1-300	Textured HDPE	**356**	259	224	**300**	**1.6**	4x4	4
GC 2-38	Textured HDPE	**178**	129.5	112	**38**	**0.4**	8x8	4
GC 2-75	Textured HDPE	**178**	129.5	112	**75**	**0.8**	8x8	4
GC 2-150	Textured HDPE	**178**	129.5	112	**150**	**1.6**	8x8	4
GC 3-19	Textured HDPE	**89**	64.75	56	**19**	**0.4**	16x16	4
GC 3-38	Textured HDPE	**89**	64.75	56	**38**	**0.8**	16x16	4
GC 3-75	Textured HDPE	**89**	64.75	56	**75**	**1.6**	16x16	4
GC 1-75	Smooth HDPE	**356**	259	224	**75**	**0.4**	4x4	4
GC 1-150	Smooth HDPE	**356**	259	224	**150**	**0.8**	4x4	4
GC 1-300	Smooth HDPE	**356**	259	224	**300**	**1.6**	4x4	4
GC 2-38	Smooth HDPE	**178**	129.5	112	**38**	**0.4**	8x8	4
GC 2-75	Smooth HDPE	**178**	129.5	112	**75**	**0.8**	8x8	4
GC 2-150	Smooth HDPE	**178**	129.5	112	**150**	**1.6**	8x8	4
GC 3-19	Smooth HDPE	**89**	64.75	56	**19**	**0.4**	16x16	4
GC 3-38	Smooth HDPE	**89**	64.75	56	**38**	**0.8**	16x16	4
GC 3-75	Smooth HDPE	**89**	64.75	56	**75**	**1.6**	16x16	4

6.3: EXPECTED RESULTS

In combination with the fully-functional testing capabilities, the proposed parametric evaluation will yield a sophisticated understanding of geocell-reinforced soil behavior as a function of certain important parameters while the transparent soil techniques will allow for novel observation and quantification of the individual reinforcement mechanisms. Together, these results will be used to create a new mechanistic design methodology fully compatible with the MEPDG in order to facilitate the growth of geocells in the geosynthetic soil reinforcement market.

Chapter 7: Conclusions

The goals of this research are threefold: 1) to observe, characterize, and quantify the separate reinforcement mechanisms that occur within geocell-reinforced soil, 2) to provide a framework to develop a mechanistic design methodology that accounts for the soil-reinforcement interaction mechanisms, and 3) to establish the protocols, equipment, and techniques for subsequent testing involving geocells and transparent soil.

In this thesis, the materials and equipment necessary to conduct a novel and comprehensive parametric evaluation of geocell-reinforced soil were developed and tested. The list of materials includes the following: three sets of geocell test sections of various dimensions fabricated from textured HDPE, smooth HDPE, and transparent PVC; ~2200 lb of crushed fused quartz; ~330 gallons of mineral oil; and opaque seeding particles for displacement tracking. The equipment includes the following: a large-scale transparent soil apparatus (LSTSA) with a 32-ft^3, acrylic-sided tank; a pneumatic loading system, a data acquisition system with associated displacement sensors and load cell; and a DSLR camera and a 100-mW, 638-nm planar laser. During the development and initial testing performed with this equipment, the follow conclusions were made:

- Transparent soil is a useful technique to visualize and quantify soil-reinforcement interaction on a small scale with very high resolution and precision. However, scaling up the transparent soil concept to properly test geocell-reinforced soil masses exaggerates some existing challenges (material processing and handling, visualization and lighting procedures) and presents new difficulties (cloudy/non-transparent appearance at large depths, refractive index matching).
- The LSTSA is capable of testing geocell test sections to failure and making a number of typical physical measurements such as applied load, vertical footing displacement,

and displacement of the geocell test section and adjacent soil mass. These measurements can be used for direct comparison to previous experimental campaigns as well as validate the results of transparent soil techniques in later testing.

- The pneumatic loading system, as a load-controlled system, was found to present a number of drawbacks including abrupt failures followed by load rebound, internal friction within the piston restricting free movement of the footing, time-lag between air pressure increases and the application of vertical load, and non-linearity between the applied air pressure and the footing load.
- The results of the initial four tests indicate that geocell reinforcement does improve the bearing capacity and, to a lesser extent, overall stiffness of unbound granular materials. However, the limitations of the loading system make comparisons to theoretical bearing capacity theories and the identification of true "failure" difficult.
- The reinforced tests showed less overall heave on the soil surface adjacent to the footing and even some settlement very close to the footing. The settlement was observed, not measured, as it occurred closer to the footing than the closest soil surface displacement sensor (within 4" of the edge of the footing). The hanging weights closest to the surface were clearly tilting in towards the footing at the end of the test despite the recording that indicated an overall heave at the 4"-mark. Laser plane illuminated and DIC would be able to provide much higher resolution soil surface profiles throughout the test.
- The filtering of micro-contaminants from the oil significantly improved the clarity of a 20" tank of oil. These micro-contaminants were transferred to the oil after a batch of fused quartz was saturated and agitated to dislodge some micro-contaminants. It was not determined how many cycles of saturation and agitation would completely rid the

fused quartz and oil of micro-contaminants, but considering the entire supply of fused quartz, it would be a time- and energy-intensive effort.

- The wavelength dependence of refractive index, also known as dispersion, means that the light conditions used to observe transparent soil have a significant impact on the transparency of the material. In order to best match the refractive index of the oil mixture with the fused quartz at the wavelength of light output by the planar laser, dispersion parameters for the two oils must be obtained, perhaps via ASTM D 1218 – the Standard Test Method for Refractive Index and Refractive Dispersion of Hydrocarbon Liquids.
- The temperature dependence of refractive index also complicates the refractive index matching. Typical daily temperature fluctuations in the laboratory correspond to oil mixture refractive index fluctuations of ±0.0003, a non-negligible amount, although this is based on the conservative assumption that the oil temperature fluctuations match air temperature fluctuations; the oil temperature fluctuations are likely far less than air temperature fluctuations.
    - The planar laser currently available cannot fully penetrate the full width of the LSTSA tank (50.5”) without dispersing into a broad, illuminated area, nor can light refracted off particle boundaries on a centered laser plane makes its way to the viewing plane without dispersing into a homogenous red light. However, the laser plane can be used to illuminate localized regions near the surface of the transparent soil. A camera can then take images during testing to measure soil particle displacements using DIC. Note, the camera angle necessary to capture these images creates significant image distortion, which considerably complicates DIC analysis.
    - A direct comparison of U2 and R2, the two tests conducted on virgin soil masses, reveals that GC 1-150 test section improves the performance of the soil mass in terms

of bearing pressure at which the first major displacement occurred, the bearing pressure at a settlement ratio of 10%, and the ultimate heave of the soil surface adjacent to the footing.

Over the course of this research, a number of challenges were encountered leading to important revelations regarding the practical aspects of large-scale transparent soil experimentation. These "lessons learned" will be helpful for future research along the same trajectory. Recommendations for future work include:

- Minimizing the contamination of the crushed fused quartz particles during processing, handling, test set-up, take-down, and storage in order to improve the quality of the transparent medium and reduce time-intensive efforts during later stages of testing.
- Small-scale and full-depth testing of transparent soil quality prior to any large-scale assembly to ensuring adequate transparency for the desired testing. Adjustments can be made much more rapidly in a small-scale set up than in a large-scale set up. However, it is important to test the transparent soil quality over the maximum depth of interest (i.e. the perpendicular distance between the parallel plane of interest and viewing plane) that will be used in large-scale testing.
- Minimizing the formation of bubbles during the placement and saturation of fused quartz-based transparent soil is crucial for efficient set-up and adequate transparency. Manual agitation and bottom-up saturation procedures were identified as the best techniques to minimize bubbles formation, although it should be noted that manual agitation will increase the relative density of the granular medium above the relative density achieved with standard placement or pluviation techniques.
- Using a grid or plane of opaque seeding particles instead of laser plane illumination for full-field soil particle displacement tracking using DIC. A grid or plane of opaque seeding particles should be used and backlit with strong, uniform lighting in order to

visualize and quantify displacements and strains within the soil mass. This technique may not yield a resolution as high as laser plane illumination, but it was identified as the most accurate methodology for large-scale transparent soil testing for planes of interest at significant depth.

- Removing all of the entrapped air bubbles while maintaining as-compacted soil structure and density. This could be achieved with a number of proposed methods: 1) vibratory motion imparted with electromagnetic drivers (such as those found in subwoofers) over a range of frequencies and amplitudes with a signal generator, 2) a board with regularly-spaced nails could be used to manually agitate thin lifts of transparent soil, or 3) the creation of a vacuum-tight lid for the LSTSA tank in order to remove all air from the tank and oil within.
- Verifying the generalized flow path induced by the oil circulation system by utilizing flow path modeling with the help of area expects in Petroleum Engineering. This analysis would be important if the oil circulation system is used for the purpose of oil ratio modification; it is necessary to know that preferential flow paths are not developing and that all of the oil contained within the pore spaces is circulating through the soil mass and circulation system.
- Embedding a GoPro or other watertight camera within the transparent soil mass in order to observe a fully-illuminated laser plane before internal refractions cause the distinct particle boundary texture to disperse into a red glare. Such a camera may be triggered remotely or via a wired connection, although care must be taken that the camera and associated wires do not have significant influence on the failure mechanisms at work.
- Replacing or modifying the loading system to include 1) a manually-operated hydraulic jack for greater control and overall capacity, 2) a computer-controlled screw jack, which would be capable of running plate load tests as either a) load-controlled tests, or

b) displacement-controlled tests. These modifications, especially the use of a screw jack, would require significant physical and software alteration.

- One additional recommendation for future work is the measurement of the tensile strength, stiffness, seam peal strength, and material-specific interface friction for all three geocell materials, textured HDPE, transparent PVC, and smooth HDPE. These parameters will be crucial for the analysis of test results and the development of a design methodology.

Appendices

APPENDIX A – DATA ACQUISITION SYSTEM DETAILS

National Instruments Hardware:
Chassis: cDAQ-9174
Available Modules:

- NI 9264 AO ±10 V Module
  - 16 channels
- NI 9263 ±10 V Module
  - 4 channels
- NI 9206 AI Fuel Cell Module
  - 16 differential or 32 RSE channels
- NI 9237 AI Bridge Module
  - 4 RJ-45/RJ-50 channels (w/ optional external excitation)
- NI 9219 AI Universal Module
  - 4 6-conductor channels

Modules Currently in Use:

- NI 9206 AI Fuel Cell Module
  - 16 differential or 32 RSE channels
- NI 9237 AI Bridge Module
  - 4 RJ-45/RJ-50 channels (w/ optional external excitation)

Sensors:

- Uni-Measure LX-PA-2.8-N1N-NNN linear position transducers
  - Up to 16 if differential AI required; up to 20 if RSE AI noise levels are acceptable
  - 4 on footing/load applicator
  - 8 on soil surface
- Geotac 5000-lb Load Cell (ID 82577)
  - 5K load cell will be used to measure a maximum load of 2,500 lb; 1-lb precision desirable
  - Relevant characteristics:
    - Capacity: 5000. lb
    - Input Resistance: 376 ohms
    - Excitation: 10.000 VDC
    - Output Resistance: 355 ohms
    - Calibration Factor: -2835692.41 lbs/V/V (may not still be valid)
    - Correlation Coefficient: 0.99999992

The wiring/connection of the load cell is complicated by mismatched cable connections and excitation. The sensor itself has a 4-pin connector which was wired by the manufacturer to a 6-pin mini DIN male connector. A member of our research group created an adapter to go from the 6-pin mini DIN male connector to a 4-conductor cable with red, black, white and green conductors. This is wired as a socket according to the manuals for the load frames with which the load cells were purchased (many years ago). Note that this is a 10 VDC sensor, so pin 6 is the excitation voltage (red).

Figure 81. Front, side, and rear view of Geotac 5k load cell and 4-pin male & 6-pin mini DIN male cable ends provided by the manufacturer

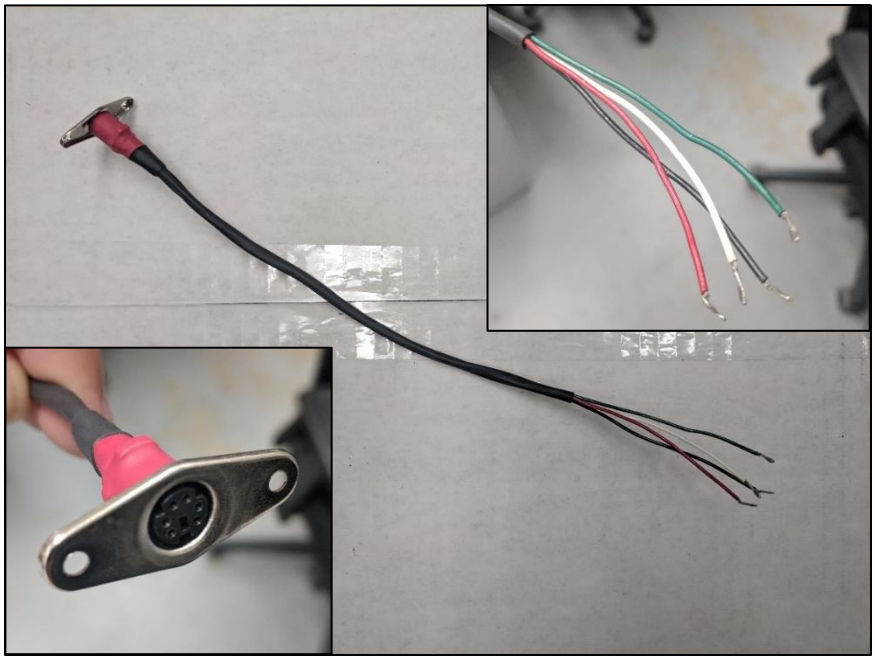

Figure 82. Custom 6-pin mini DIN female -to- 4-conductor cable adapter

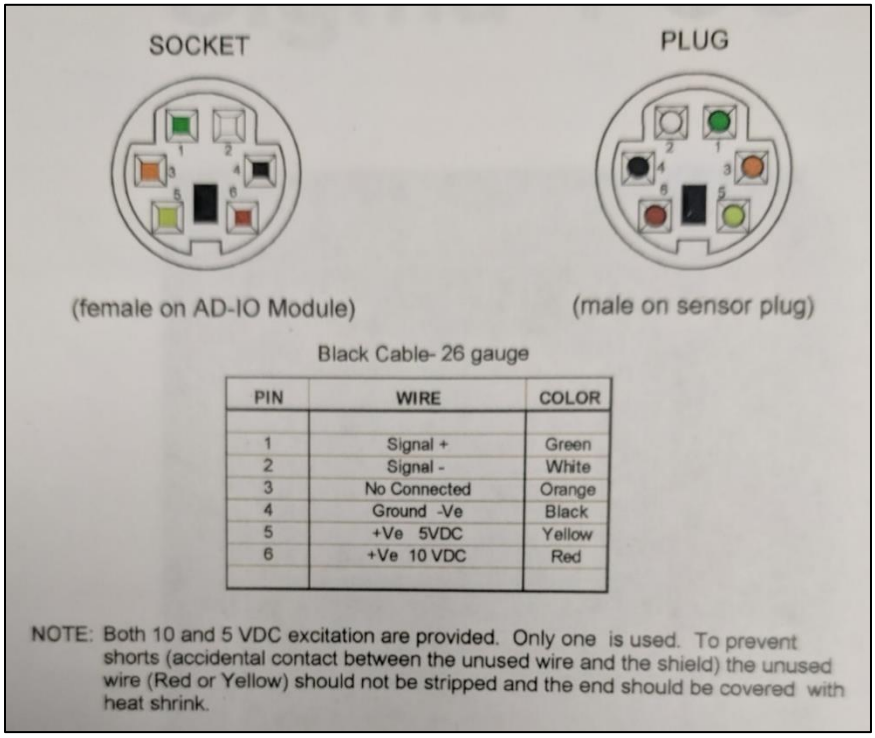

PIN	WIRE	COLOR
1	Signal +	Green
2	Signal -	White
3	No Connected	Orange
4	Ground -Ve	Black
5	+Ve 5VDC	Yellow
6	+Ve 10 VDC	Red

Figure 83. 6-pin mini DIN female connector to 4-conductor cable pinout diagram

The four conductors on the adapter are connected via butt connectors to the four appropriate conductors in the RJ-45 cable. As depicted in the pinout of NI 9237, a full bridge connection should be wired with CH+ in (2), CH- in (3), EX+ in (6), and EX- in (7). Based on the conductor colors in the RJ-45 plug, those pin positions correspond to the following conductor colors: (2) – Orange/White; (3) – Orange; (6) – Green/White; (7) – Green. Table 2 summarizes the required connections.

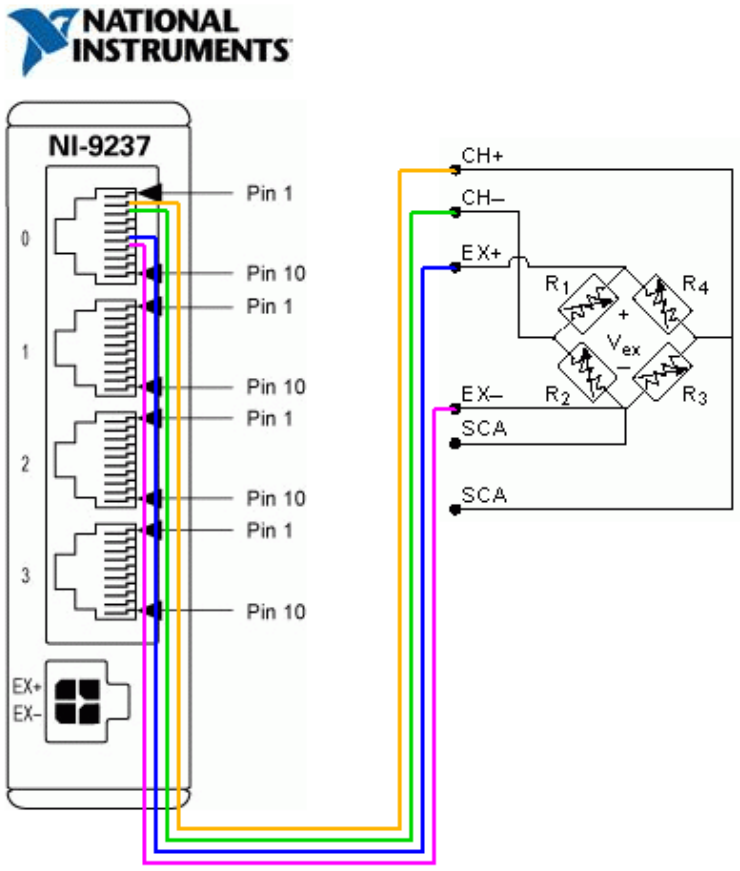

Figure 84. NI 9237 full bridge pinout diagram

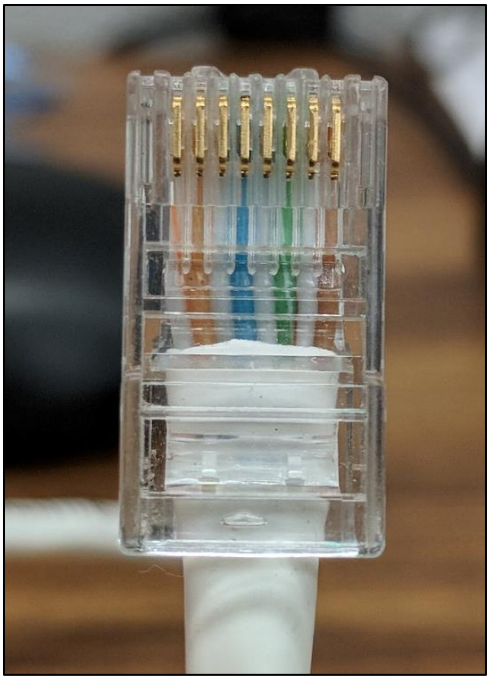

Figure 85. RJ-45 Conductor Colors (1-10, Left-Right)

Table 8. Required wire connections from load cell to NI 9237

Purpose	CH+ / Signal+	CH- / Signal-	EX+ / +Ve 10 VDC	EX- / Ground - Ve
6-pin DIN Position/Color	1 / Green	2 / White	6 / Red	4 / Black
RJ-45 Pin Position (Fig 9)	2	3	6	7
RJ-45 Color (Fig 10)	Orange/White	Orange	Green/White	Green

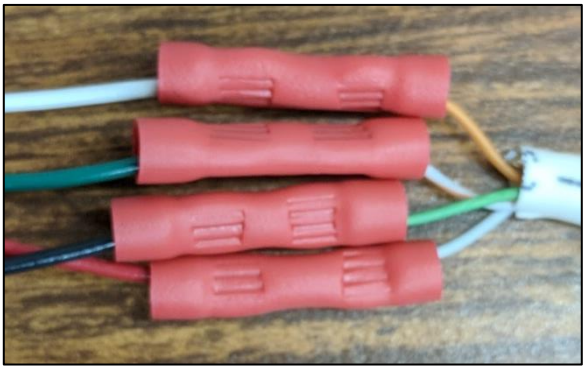

Figure 86. Butt connections made according to Table 8

The excitation voltage for the load cell and all displacement sensors is 10 VDC. This constant voltage is provided by an external power source, a Mastech HY30055D DC power supply. Power is supplied to the displacement sensors wired in parallel using two terminal blocks according to the schematic in Figure 87. Excitation is provided to the load cell via a splice in its cable also in parallel with the displacement sensor, but not attached to the terminal blocks. The NI 9237 bridge module is not capable of supplying enough voltage to power to load cell. There has been some indications of signal interference between sensors; steps should be taken to mitigate that interference.

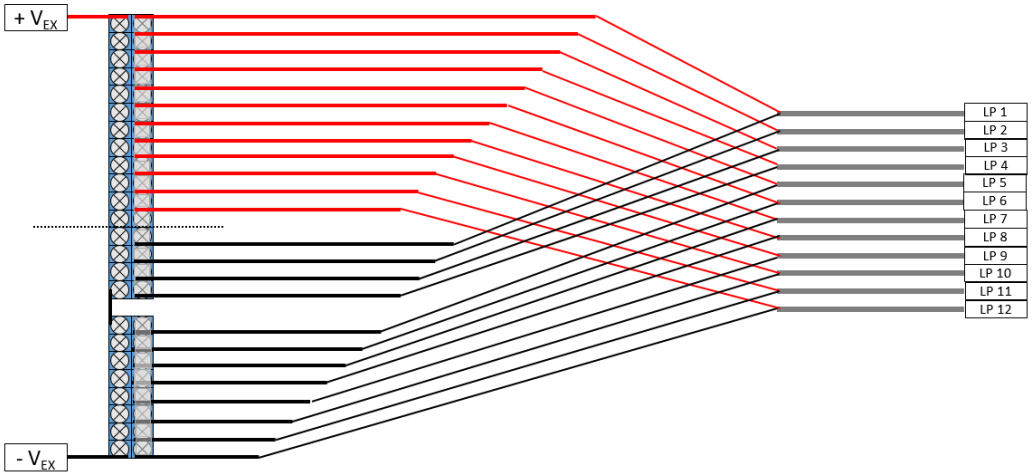

Figure 87. Excitation voltage wiring schematic for displacement sensors

APPENDIX B – ADDITIONAL RESULTS FROM TEST U1, R1, U2, AND R2

Unreinforced 1

Lift	Mark	h (in)	h_{tot} (in)	Bucket 1	Bucket 2	Bucket 3	Bucket 4	Bucket 5	Bucket 6	Bucket 7	Bucket 8	W_{cfq} (lb)	γ (pcf)
1	0.5	2.2	2.0	55.5	55.5	55.5	55.5	0.0	0.0	0.0	0.0	222.0	68.4
2	3.1	2.4	4.6	49.4	49.6	49.4	49.7	49.1	49.1	0.0	0.0	296.3	82.8
3	5.6	2.4	7.1	47.9	50.2	49.6	53.2	50.5	51.9	0.0	0.0	303.3	84.3
4	7.6	2.1	9.1	48.6	48.6	50.2	48.6	48.7	52.7	0.0	0.0	297.6	97.8
5	9.9	2.3	11.4	49.6	49.0	49.0	50.9	50.0	49.4	0.0	0.0	297.8	89.7
6	12.6	2.8	14.1	48.7	50.0	48.1	51.0	48.7	49.4	0.0	0.0	295.9	72.9
7	14.9	2.3	16.4	50.5	49.9	48.6	51.2	48.4	49.9	0.0	0.0	298.4	89.9
8	15.8	0.9	17.3	31.6	34.0	32.7	29.3	0.0	0.0	0.0	0.0	127.5	92.2
												2138.9	84.7

Reinforced 1

Lift	Mark	h (in)	h_{tot} (in)	Bucket 1	Bucket 2	Bucket 3	Bucket 4	Bucket 5	Bucket 6	Bucket 7	Bucket 8	W_{cfq} (lb)	γ (pcf)
1	0.7	2.2	2.2	39.6	38.8	37.6	37.6	37.6	30.1	0.0	0.0	221.3	68.5
2	3.0	2.3	4.5	49.4	49.4	49.4	49.4	49.4	49.4	0.0	0.0	296.2	86.8
3	5.2	2.2	6.7	49.4	49.4	49.4	49.4	49.4	49.4	0.0	0.0	296.2	91.7
4	7.6	2.4	9.1	49.4	49.4	49.4	49.4	49.4	49.4	0.0	0.0	296.2	84.5
5	10.1	2.5	11.6	49.4	49.4	49.4	49.4	49.4	49.4	0.0	0.0	296.2	80.3
6	12.4	2.4	13.9	49.4	49.4	49.4	49.4	49.4	49.4	0.0	0.0	296.2	84.5
7	15.6	3.1	17.1	49.4	49.4	49.4	49.4	98.7	104.7	0.0	0.0	400.9	86.9
8	16.1	0.6	17.6	31.3	31.3	17.8	0.0	0.0	0.0	0.0	0.0	80.4	96.9
												2183.5	85.0

Unreinforced 2

Lift	Mark	h (in)	h_{tot} (in)	Bucket 1	Bucket 2	Bucket 3	Bucket 4	Bucket 5	Bucket 6	Bucket 7	Bucket 8	W_{cfq} (lb)	γ (pcf)
1	0.9	2.4	2.4	37.0	37.0	37.0	37.0	37.6	25.1	11.3	0.0	221.8	63.3
2	3.2	2.3	4.7	37.0	37.0	37.0	37.0	37.0	37.0	37.0	37.0	295.7	86.6
3	5.6	2.4	7.1	37.0	37.0	37.0	37.0	37.0	37.0	37.0	37.0	295.7	82.2
4	7.9	2.3	9.4	37.0	37.0	37.0	37.0	37.0	37.0	37.0	37.0	295.7	89.0
5	10.2	2.3	11.7	37.0	37.0	37.0	37.0	37.0	37.0	37.0	37.0	295.7	86.6
6	12.6	2.4	14.1	37.0	37.0	37.0	37.0	37.0	37.0	37.0	37.0	295.7	82.2
7	15.0	2.4	16.5	37.0	37.0	37.0	37.0	37.0	37.0	37.0	37.0	295.7	84.4
8	16.0	1.0	17.5	37.6	37.6	37.6	37.6	8.8	0.0	0.0	0.0	159.1	107.8
												2154.9	85.3

Reinforced 2

Lift	Mark	h (in)	h_{tot} (in)	Bucket 1	Bucket 2	Bucket 3	Bucket 4	Bucket 5	Bucket 6	Bucket 7	Bucket 8	W_{cfq} (lb)	γ (pcf)
1	1.1	2.6	2.6	27.7	27.7	27.7	27.7	27.7	27.7	27.7	27.7	221.5	57.2
2	3.3	2.1	4.8	37.0	37.0	37.0	37.0	37.0	37.0	37.0	37.0	295.7	94.3
3	5.2	1.9	6.7	37.0	37.0	37.0	37.0	37.0	37.0	37.0	37.0	295.7	103.4
4	8.0	2.8	9.5	37.0	37.0	37.0	37.0	37.0	37.0	37.0	37.0	295.7	71.2
5	10.2	2.2	11.7	37.0	37.0	37.0	37.0	37.0	37.0	37.0	37.0	295.7	91.6
6	12.4	2.2	13.9	37.0	37.0	37.0	37.0	37.0	37.0	37.0	37.0	295.7	91.6
7	15.1	2.8	16.6	37.0	37.0	37.0	37.0	37.0	37.0	74.5	59.5	355.8	87.7
8	15.8	0.7	17.3	35.6	38.1	19.0	0.0	0.0	0.0	0.0	0.0	92.7	89.7
												2148.4	85.8

Figure 88. Placement and compaction record from initial test series

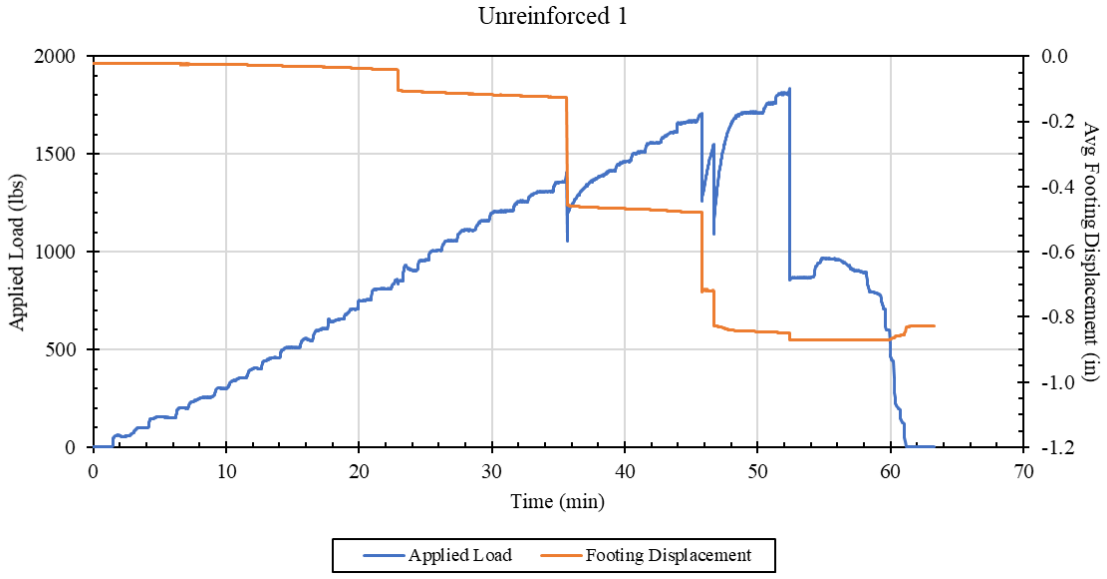

Figure 89. Applied load and footing displacement as a function of time during U1

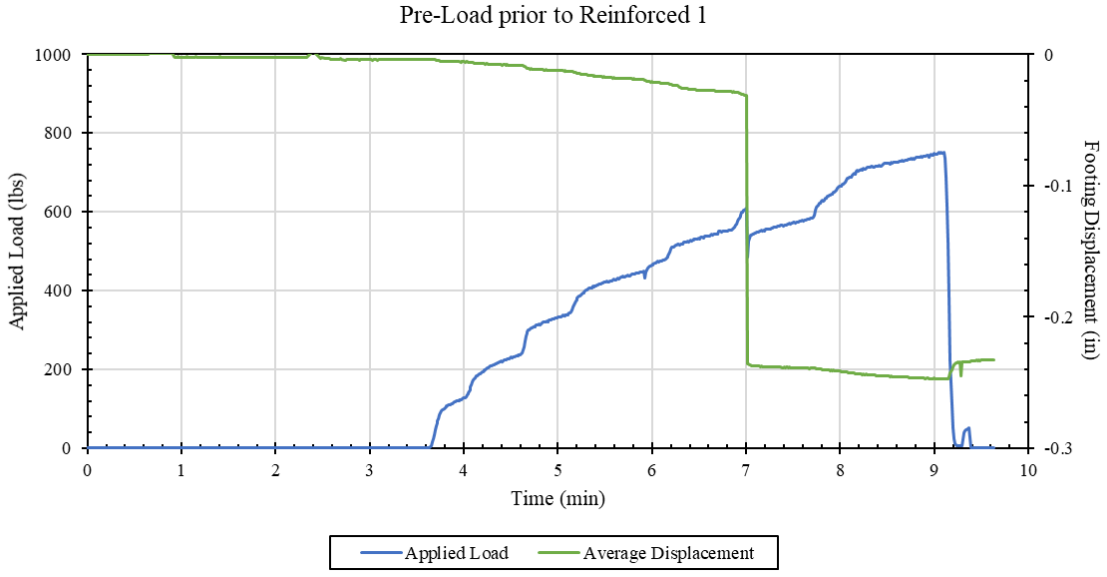

Figure 90. Applied load and footing displacement during R1 pre-loading

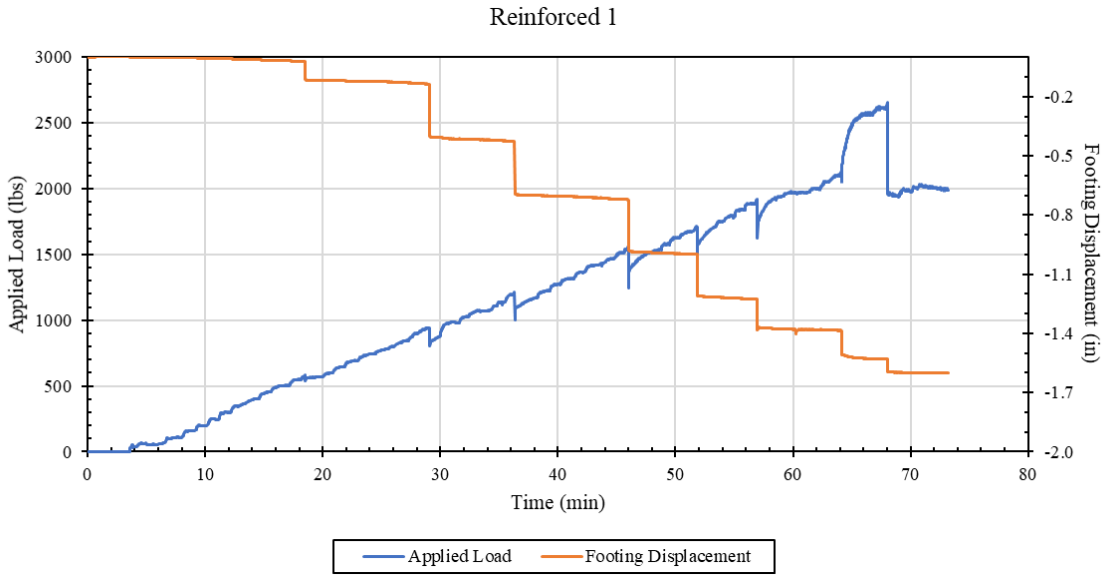

Figure 91. Applied load and footing displacement as a function of time during R1

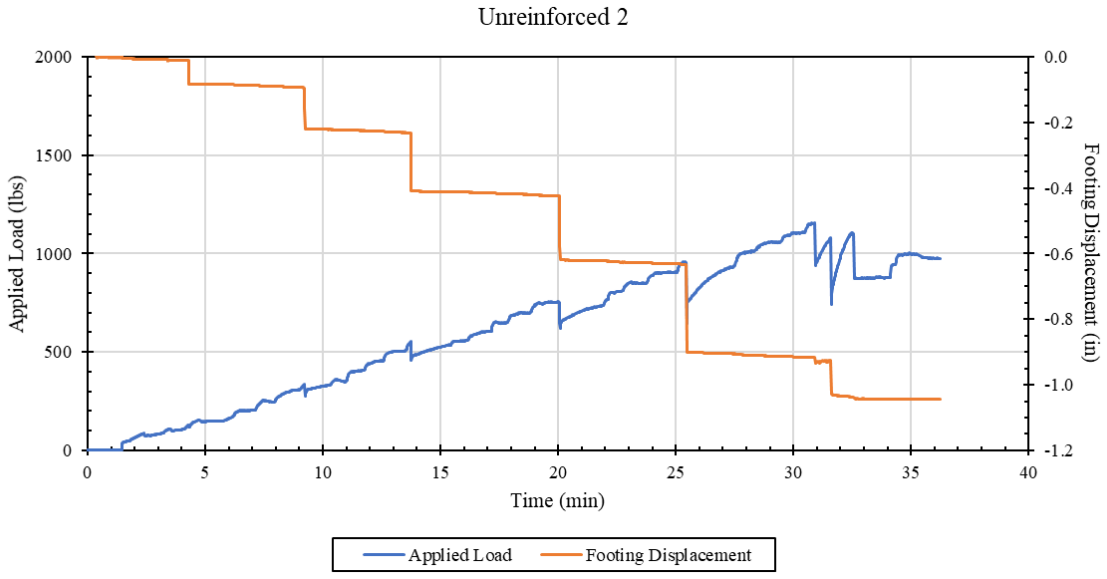

Figure 92. Applied load and footing displacement as a function of time during U2

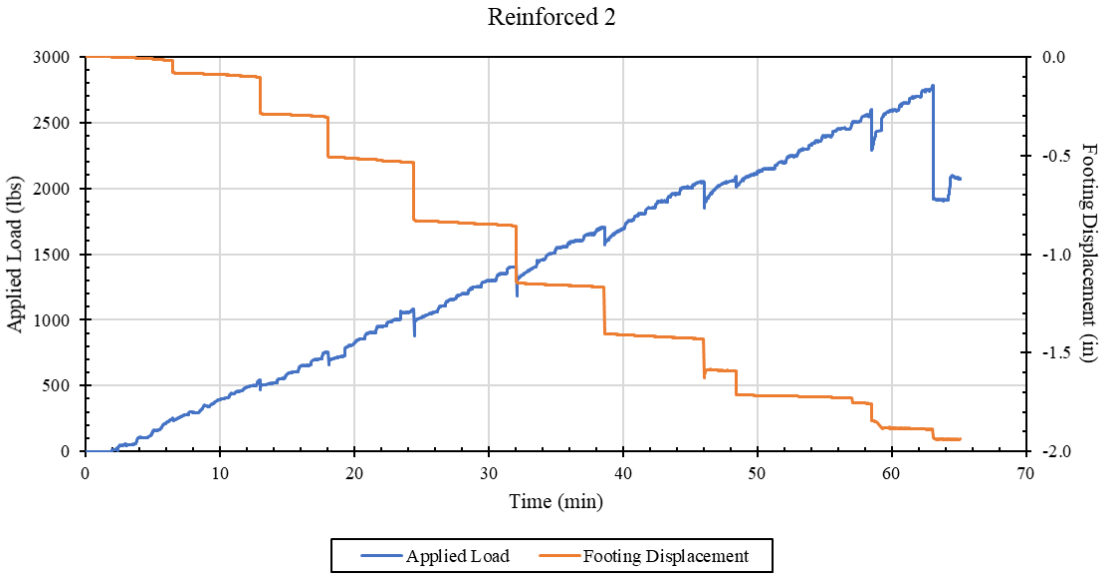

Figure 93. Applied load and footing displacement as a function of time during R2

Bibliography

AASHTO. 2007. *AASHTO T 307-99: Determining the Resilient Modulus of Soils and Aggregate Materials.* Testing Standard, American Association of State Highwy and Transportation Officials.

Aguilar-Arevalo, A. A., et al. 2008. "The MiniBooNE Detector." *Nuclear Instruments and Methods in Physics Research* (Elsevier) 28-46.

Al-Qadi, I. L., and J. J. Hughes. 2000. "Field evaluation of geocell use in flexible pavements." *Transportation Research Record: Journal of the Transportation Research Board* 26-35.

Andela Products Ltd. 2017. "Sieve Analysis." Richfield Springs, NY.

ARA, Inc., ERES Consultants Division. 2004. *Guide for Mechanistic-Empirical Design of New and Rehabilitated Pavement Structures.* Final Report, National Cooperative Highway Research Program, Transportation Research Board, National Research Council.

Arago, D. F., and J. B. Biot. 1806. *Mem. Acad. France* 7-9.

Avesani Neto, J. O., B. S. Bueno, and M. M. Futai. 2013. "A bearing capacity calculation method for soil reinforced with a geocell." *Geosynthetics International, 20, No. 3* 129-140.

—. 2016. "Design of a calculation method for geocell-reinforced soils and verification through bearing capacity laboratory experiements." *GeoAmericas 2016, 3rd Pan-American Conference on Geosynthetics.* Miami Beach: International Geosynthetics Society. 1817-1829.

Avesani Neto, J. O., B. S. Bueno, and M. M. Futai. 2015. "Evaluation of a calculation method for embankments reinforced with geocells over soft soils using finite-element analysis." *Geosynthetics International* 439-451.

Bathurst, R. J., and F. M. Ezzein. 2015. "Geogrid and soil displacement observations during pullout using a transparent granular soil." *Geotechnical Testing Journal* 673-685.

Bathurst, R. J., and K. Rajagopal. 1993. "Large-scale triaxial compression testing of geocell-reinforced granular soils." *Geotechnical Testing Journal, Vol. 16, No. 3* 296-303.

Bathurst, R. J., and R. E. Crowe. 1992. "Recent cases histories of flexible geocell retaining walls in north america." *Recent Case Histories of Permanent Geosynthetic-reinforced Soil Retaining Walls.* Tokyo: A.A. Balkema, Rotterdam. 3-20.

Beemer, R. D., E. Shaughnessy, K. R. Ewert, N. Boardman, G. Biscontin, C. P. Aubeny, and F. J. Grajales. 2016. "The use of sodium pyrophosphate to improve a translucent clay simulate." *Geo-Chicago 2016: Sustainable Materials and Resource Conservation.* Chicago: ASCE. 83-93.

Bhasin, A. 2017. "CE 391 P.2 - Design and Performance of Pavements." Course Notes, Austin, Texas.

Black, J. A. 2015. "Centrifuge modelling with transparent soil and laser aided imaging." *Geotechnical Testing Journal* 631-644.

Chen, R., Y. Huang, and F. Huang. 2013. "Confinement effect of geocells on sand samples under triaxial compression." *Geotextiles and Geomembranes* 35-44.

Coduto, D. P., M. R. Yeung, and W. A. Kitch. 2011. *Geotechnical Engineering: Principles and Practices Second Edition.* Upper Saddle River, NJ: Pearson Higher Education, Inc.

Cole, R. T., and K. M. Rollins. 2006. "Passive earth pressure mobilization during cyclic loading." *Journal of Geotechnical and Geoenvironmental Engineering* 1154-1164.

Dale, T. P., and J. H. Gladstone. 1858. "On the influence of temperature on the refraction of light." *Philosphical Transactions of the Royal Society of London* 887-894.

Dash, S. K. 2012. "Effect of geocell type on load-carrying mechanisms of geocell-reinforced sand foundations." *International Journal of Geomechanics* 537-548.

Dash, S. K., K. Rajagopal, and N. R. Krishnaswamy. 2007. "Behavior of geocell-reinforced sand beds under strip loading." *Canadian Geotechnical Journal* 905-916.

Dash, S. K., N. R. Krishnaswamy, and K. Rajagopal. 2001. "Bearing capacity of strip footings supported on geocell-reinforced sand." *Geotextiles and Geomembranes* 235-256.

Dash, S. K., P. D. T. Reddy, and S. T. G. Raghukanth. 2008. "Subgrade modulus of geocell-reinforced sand foundations." *Proceedings of the Institution of Civil Engineers - Ground Improvement* 79-87.

Dash, S. K., S. Sireesh, and T. G. Sitharam. 2003. "Model studies on circular footing supported on geocell reinforced sand underlain by soft clay." *Geotextiles and Geomembranes* 197-219.

Emersleben, A., and N. Meyer. 2009. "Interaction between hoop stresses and passive earth resistances in single and multiple geocell structures." *GIGSA GeoAfrica 2009 Conference Proceedings.* Cape Town: GIGSA. 1-10.

Ezzein, F. M., and R. J. Bathurst. 2014. "A new approach to evaluate soil-geosynthetic interaction using a novel pullout test apparatus and transparent granular soil." *Geotextiles and Geomembranes* 246-255.

Ezzein, F. M., and R. J. Bathurst. 2011. "A transparent sand for geotechnical laboratory modeling." *Geotechnical Testing Journal* 590-601.

Ferreira, J. A. Z. 2013. *Evaluation of soil-geogrid interaction at different load levels using pullout tests and transparent soil.* PhD Thesis, Austin, TX: The University of Texas at Austin.

Ferreira, J. A. Z., and J. G. Zornberg. 2015. "A transparent pullout testing device for 3D evaluation of soil-geogrid interaction." *Geotechnical Testing Journal* 686-706.

Foster, C. R., and R. G. Ahlvin. 1954. "Stresses and deflections induced by a uniform circular load." *Thirty-Third Annual Meeting of the Highway Research Board.* Washington, D.D.: Highway Research Board. 467-470.

Ganiyu, A. A., A. S. A. Rashid, and M. H. Osman. 2016. "Utilisation of transparent synthetic soil surrogates in geotechincal physical models: a review." *Journal of Rock Mechanics and Geotechnical Engineering* 568-576.

Hedge, A., and T. G. Sitharam. 2015. "3-Dimensional numerical modelling of geocell reinforced sand beds." *Geotextiles and Geomembranes* 171-181.

Heller, W. 1945. "The determination of refractive indices of colloidal particles by means of a new mixture rule or from measurements of light scattering." *Physical Review Journals* 5-10.

Henkel, D. J., and G. D. Gilbert. 1952. "The effect of the rubber membrane on the measured triaxial compression strength of clay samples." *Geotechnique* 20-29.

Heraeus. 2016. "Quartz Glass for Optics - Data and Properties." Technical Data Sheet.

Iskander, M., R. J. Bathurst, and M. Omidvar. 2015. "Past, present, and future of transparent soils." *Geotechnical Testing Journal* 557-573.

Iskander, M., S. Sadek, J. Liu, K. Tabe, M. Ahmed, I. Guzman, S. Kashuk, et al. 2016. *Transparent Soils Wiki.* Accessed July 29, 2018. https://wp.nyu.edu/ts/.

Jenkins, F. A., and H. E. White. 1981. *Fundamentals of Optics, 4th ed.* New York, NY: McGraw-Hill, Inc.

Kief, O., and K. Rajagopal. 2008. "Three dimensional cellular confinement system contribution to structural pavement reinforcement." *Geosynthetics India '08 International Seminar.* Hyerabad (Andhra Pradesh): Indian Chapter of International Geosynthetics Society and the Central Board of Irrigation & Power (CBIP).

Koerner, R. M. 2005. *Designing with Geosynthetics - 5th ed.* Upper Saddle River, NJ: Pearson Education, Inc.

Latha, M. 2011. "Design of geocell reinforcement for supporting embankments on soft ground." *Geomechanics and Engineering, Vol 3, No. 2* 117-130.

Leshchinsky, B., and H. I. Ling. 2013. "Numerical modeling of behavior of railway ballasted structure with geocell confinement." *Geotextiles and Geomembranes* 33-43.

Lorentz, H. A. 1906. *The Theory of Electrons and Its Applications to the Phenomena of Light and Radiant Heat.* New York, NY.

Malitson, I. H. 1965. "Interspecimen comparison of the refractive index of fused silica." *Journal of the Optical Society of America* 1205-1209.

marketsandmarkets.com. 2018. *Geocells Market by Raw Material, Design Type, Application, and Region - Global Forecast to 2022.* April. Accessed July 2, 2018. https://www.marketsandmarkets.com/Market-Reports/geocells-market-30761024.html.

—. 2014. *Geosynthetics Market by Type & Applications, and by Region - Trends and Forecasts to 2019.* November. Accessed July 2, 2018. https://www.marketsandmarkets.com/Market-Reports/geosynthetic-market-1174.html.

McClymer, J. P. 2016. "Precise determination of the refractive index of suspended particles: light transmission as a function of refractive index mismatch." *American Journal of Physics* 602-605.

Mengelt, M., T. B. Edil, and C. H. Benson. 2000. *Reinforcement of flexible pavements using geocells.* Geo Engineering Report No. 00-04, Dept. of Civil and Environmental Engineering, University of Wisconsin-Madison.

Mengelt, M., T. B. Edil, and C. H. Benson. 2006. "Resilient modulus and plastic deformation of soil confined in a geocell." *Geosynthetics International* 195-205.

Ohara Corporation. 2018. *Introduction to Glass Properties - Optical Properties.* Accessed July 30, 2018. http://oharacorp.com/o2.html.

Peng, X., and J. G. Zornberg. 2017. "Evaluation of load transfer in geogrids for base stabilization using transparent soil." *Transportation Geotechnics and Geoecology.* Saint Petersburg, Russie: Elsevier. 307-314.

—. 2016. "Evaluation of load transfer in triaxial geogrids using transparent soil." *GeoAmericas 2016, 3rd Pan-American Conference on Geosynthetics.* Miami Beach, Florida: International Geosynthetics Society. 1520-1531.

Petro-Canada Lubricants Inc. 2013. "Paraflex (TM) HT Fluids." Technical Data Sheet, Mississauga, Ontario.

Petro-Canada Lubricants Inc. 2017. "Puretol (TM) White Mineral Oils." Technical Data Sheet, Mississauga, Ontario.

Pokharel, S. K. 2010. *Experimental study on geocell-reinforced bases under static and dynamic loading.* Dissertation, Lawrence: The University of Kansas.

Pokharel, S. K., Han. J., D. Leshchinsky, and R. L. Parsons. 2017. "Experimental evaluation of geocell-reinforced bases under repeated loading." *International Journal of Pavement Research and Technology* 114-127.

Pokharel, S. K., J. Han, D. Leshchinsky, R. Parsons, and I. Halahmi. 2010. "Investigation of factors influencing behavior of single geocell-reinforced bases under static loading." *Geotextiles and Geomembranes* 570-578.

Presto Geosystems. 2009. "Geocells: The early days with the Army Corps." *Geosynthetics Magazine* 45.

Presto Geosystems. 2008. "Geoweb Load Support System: Technical Overview." Appleton, Wisconsin.

Rajagopal, K., G. M. Latha, and N. R. Krishnaswamy. 2001. "Finite element analysis of embankments supported on geocell layer." *Computer Methods and Advances in Geomechanics: Proceedings of the 10th International Conference on Computer Methods and Advances in Geomechanics.* Tucson, Arizona: CRC Press.

Rajagopal, K., N. R. Krishnaswamy, and G. M. Latha. 1999. "Behaviour of sand confined with single and multiple geocells." *Geotextiles and Geomembranes, 17* 171-184.

Reis, J. C. R., I. M. S. Lampreia, A. F. S. Santos, M. L. C. J. Moita, and G. Douheret. 2010. "Refractive index of liquid mixtures: theory and experiment." *ChemPhysChem* 3722-3733.

Richardson, Gregory N. 2004. "Geocells, a 25-year perspective part 1: roadway applications." *Geotechnical Fabrics Report, GFR* 14-19.

Richardson, Gregory N. 2004. "Geocells, a 25-year perspective part 2: channel erosion control and retaining walls." *Geotechnical Fabrics Report, GFR* 22-27.
Sellmeier, W. 1871. "Zur Erklärung der abnormen Farbenfolge im Spectrum einiger Substanzen." *Annalen der Physik und Chemie* 272-282.
Strata Systems, Inc. 2015. "StrataWeb 356 Product Data." Cumming, GA, January 1.
Strata Systems, Inc. 2016. "StrataWeb: Design Guidelines for Soil Stabilization." Design Guidelines.
Tseng, K., and R. L. Lytton. 1989. "Prediction of permanent deformation in flexible pavement materials." *ASTM STP 1016* 154-172.
Weiner, O. 1910. *Zur Theorie der Refraktionskonstanten.* Leipzig.
Wiederseiner, S., N. Andreini, G. Epley-Chauvin, and C. Ancey. 2011. "Refractive-index and density matching in concentrated particle suspensions: a review." *Experiments in Fluids* 1183-1206.
Witczak, M. W. 2003. *Harmonized Test Methods for Laboratory Determination of Resilient Modulus for Flexible Pavement Design.* Tempe: National Cooperative Highway Research Program, Transportation Research Board, National Research Council.
Yang, X., J. Han, S. K. Pokharel, C. Manandhar, R. L. Parsons, D. Leshchinsky, and I. Halahmi. 2012. "Accelerated pavement testings of unpaved roads with geocell-reinforced sand bases." *Geotextiles and Geomembranes* 95-103.
Yoder, E. J., and M. W. Witczak. 1975. *Principles of Pavement Design.* New York: Wiley.
Zhang, L., M. Zhou, C. Shi, and H. Zhou. 2010. "Bearing capacity of geocell reinforcement in embankment engineering." *Geotextiles and Geomembranes* 475-482.